TIME-DEPENDENT BEHAVIOR OF PRETENSIONED STAINLESS STEEL BARS USED FOR STRUCTURAL REHABILITATION AND RETROFITTING

A Dissertation
Presented to
The Academic Faculty

By

Falak Dipak Shah

In Partial Fulfillment
of the Requirements for the Degree of
Doctor of Philosophy

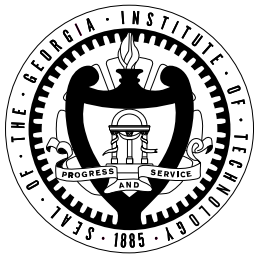

Structural Engineering, Mechanics, and Materials
School of Civil and Environmental Engineering
Georgia Institute of Technology

December 2014

TIME-DEPENDENT BEHAVIOR OF PRETENSIONED STAINLESS STEEL BARS USED FOR STRUCTURAL REHABILITATION AND RETROFITTING

Approved by:

Prof. Abdul-Hamid Zureick, Co-Advisor
School of Civil and Environmental Engineering
Georgia Institute of Technology

Prof. Bruce R. Ellingwood, Co-Advisor
School of Civil and Environmental Engineering
Georgia Institute of Technology

Prof. Richard W. Neu
School of Mechanical Engineering
Georgia Institute of Technology

Prof. Preet M. Singh
School of Materials Science and Engineering
Georgia Institute of Technology

Prof. Phanish Suryanarayana
School of Civil and Environmental Engineering
Georgia Institute of Technology

Date Approved: October 31, 2014

Acknowledgements

Doctoral dissertations are collections of ideas and knowledge, nurtured in an environment involving many mentors, colleagues, and friends. The work here is no exception.

My advisors, Professors Abdul-Hamid Zureick and Bruce Ellingwood, deserve distinct gratitude. Without their guidance, patience, and experience, I could not have become the researcher, engineer, and person I am today.

Professors Preet Singh, Rick Neu, and Phanish Suryanarayana are thanked for generously giving me their time as well as access to their labs and other resources.

I am also appreciative of Institute staff members Jeremy Mitchell, Andy Udell, J. D. Huggins (ME), Jamshad Mahmood (MSE), Donny Otwell, and Mike Sorenson.

Tim Wright, Nick Reynolds, Sung-Hu Kim, and Andrew Bechtel were great friends, helpers, and partners-in-crime. Amal Jayapalan, Chris Shearer, Nathan Mayercsik, Bradley Dolphyn, Elizabeth Nadelman, Laura Redmond, Brett Holland, Passarin Jongvisuttisun, the HPEPL people, Daniela Estrada, Daniel Schuetz, Mitchell McKay, Eric Anger, Giovanni Loreto, Lisa Burris, Sujith Mangalathu, Eun Cha, Ruth Jensen, and Badal Juneja made the past four years a blast.

Finally, surviving this process would not have been possible without the unconditional love and support of my family. Thank you for always being there for me, Pappa and Mummy, Ropa, Achal, Molly, Minolee, and all my other family members.

Table of contents

List of tables

List of figures

List of symbols

b_v	thickness of pier cap
c	material-specific parameter in Bažant-Yu viscoplastic constitutive model
d_s	depth of tension reinforcement
d_s'	depth of compression reinforcement
f_c'	compressive strength of concrete
f_{cu}	allowable stress in strut
f_s	nominal stress in strut
h_a	height of node in strut-and-tie model
k	material-specific parameter in Bažant-Yu viscoplastic constitutive model
k_B	Boltzmann constant
l_b	width of bearings
l_c	width of pier column
p_{sr}	percent stress relaxation, defined as $p_{sr} = \frac{\sigma(t) - \sigma_0}{\sigma_0} \times 100$
t	time
v_r	vibration constant in logarithmic creep model
w_s	width of strut
A	parameter in continuum damage mechanics (CDM) creep model
A_T	Arrhenius factor

D	damage variable
D_p^{cr}	creep damage
D_p^{ti}	time-independent plastic damage
E	modulus of elasticity
$\tilde{E}$	effective modulus of elasticity
E_n	analogous spring constant in rheological models, where n is the number of springs
Fe	percent ferrite
FN	ferrite number
K	parameter in CDM creep model
P_{clamp}	pretension clamp force
P_u	force in a pier column
Q_c	activation energy associated with creep
Q_{sr}	activation energy associated with stress relaxation
R	universal gas constant
T	temperature
T_0	reference temperature [294.2 K in this study]
T_H	homologous temperature, defined as the ratio of service temperature and the material's melting temperature in absolute units
T_m	melting temperature [2525–2630 °F for the UNS S32101 stainless steel]
α_{ct}	stress relaxation amplification factor for isothermal temperature increase
α_r	constant in logarithmic creep model
α_{vt}	stress relaxation amplification factor for a variable temperature increase

β_1	compressive strength factor for concrete
ε	strain
ε^{cr}	creep strain
ε^{e}	elastic strain
ε^{tot}	total strain
γ	parameter in the Bažant-Yu viscoplastic constitutive model
η_n	analogous coefficient of viscosity in rheological models, where n is the number of dashpots
θ_s	angle of diagonal strut
λ_c	hydrostatic factor used with the strut-and-tie model
λ_{ss}	parameter in Bažant-Yu viscoplastic constitutive model
ρ	material-specific parameter in Bažant-Yu viscoplastic constitutive model for stainless steel [defined in this study as 1,000 hours]
σ	stress
σ_0	initial stress [i.e., $\sigma(t=0)$]
$\sigma_{0.01}$	0.01% proof stress
$\sigma_{0.2}$	0.2% strain offset yield stress
σ_y, f'_y	yield stress [taken as the 0.5% extension under load (EUL)]
θ_s	angle of diagonal strut

Summary

The objective of this study is to characterize the long-term behavior of an austenitic-ferritic stainless steel-based pretensioned system for strengthening reinforced concrete bridge pier caps in shear. Stress relaxation experiments were conducted on UNS S32101 stainless steel bars subjected to various initial stresses and temperatures within the low homologous temperature (LHT) regime. Data from these experiments were used to develop a viscoplastic constitutive model to describe the long-term time- and temperature-dependent behavior of the stainless steel bars. This mechanics-based approach is integrated with an analytical method based on strut-and-tie analysis to compute the shear strength of reinforced concrete pier caps strengthened with this external pretensioned system.

Chapter 1
Introduction

1.1 Background and motivation

Condition assessment of existing reinforced concrete bridge pier caps using the current AASHTO *LRFD Bridge Design Specifications* (2010) has led to the view that many bridges in the state of Georgia are structurally deficient (Wang et al. 2011). Bridges deemed structurally deficient are posted (i.e., vehicles over specified weight limits are prohibited from using that bridge); such postings may have an adverse economic impact on local communities when truck route lengths and travel times are increased. This research aims to characterize the long-term behavior of a stainless steel-based strengthening system used to improve the shear strength of existing reinforced concrete (RC) pier caps.

Pier caps behave structurally as deep beams that transfer loads from a bridge's superstructure (decks, girders) to its piers and, ultimately, to its foundation (Fig. 1.1). Such RC deep beams may be analyzed as an equivalent truss system consisting of compression struts, tension ties, and nodal zones (AASHTO 2007). One particular system for strengthening bridge pier caps with apparent shear deficiencies involves the use of external pretensioned bars to cause the pier cap structural resistance to transform from a single-strut mechanism to a multiple-strut mechanism, leading to an increase in the member's shear capacity (Fig. 1.2). Zureick et al. (2014) studied the fundamental mechanical behavior of these RC deep beams with external reinforcement systems that

use carbon steel bars. While hot-dipped galvanized steel bars are currently used in the state of Georgia, the use of austenitic-ferritic (duplex) stainless steel bars has been proposed as an alternative. However, the influence of stress relaxation of stainless steel on the long-term performance of such systems has yet to be fully investigated. This research addresses this deficiency by studying the time-dependent behavior of an external post-tensioned system that uses duplex stainless steel bars.

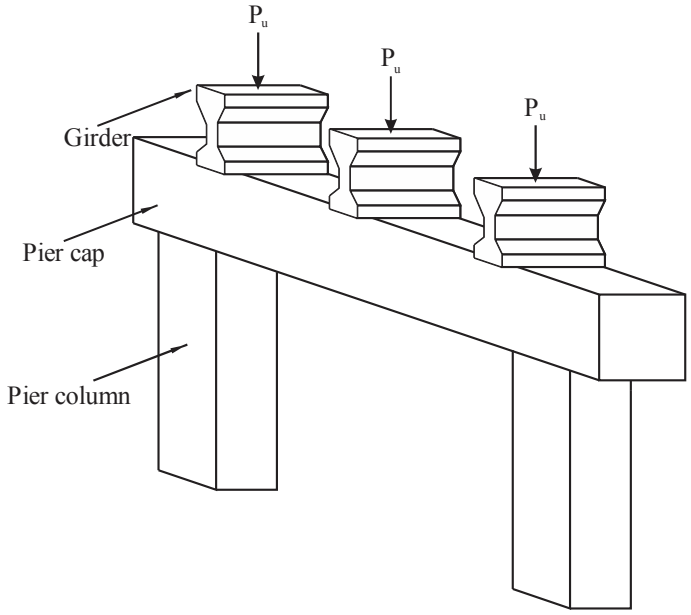

Figure 1.1. Schematic of a typical bridge substructure

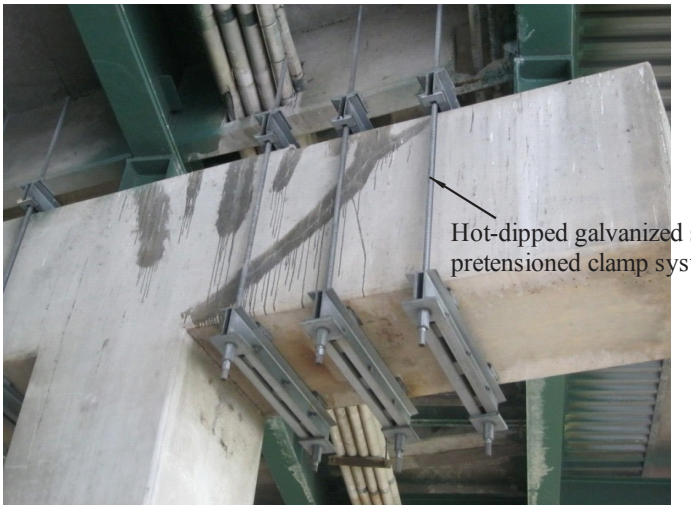

Figure 1.2. Pretensioned clamp system installed on a bridge pier cap

1.2 UNS S32101 stainless steel

The focus of this study is the UNS S32101 stainless steel. It is a duplex alloy, meaning its microstructure is composed of approximately equal parts of austenitic and ferritic grains (Johansson and Liljas 2002), and its nominal chemical composition is given in Table 1.1. This grade offers several advantages, specifically: a high mechanical strength; a resistance to uniform and pitting corrosion that is comparable to that found in the austenitic grades UNS S30400 and UNS S31600; and a resistance to stress corrosion cracking that is comparable to that characteristic of austenitic grade UNS S30400 (Johansson and Liljas 2002, Sieurin et al. 2006, Johansson and Prošek 2007). Furthermore, its lower nickel content reduces its price volatility—quantified through the alloy adjustment factor (AAF)—in comparison with austenitic alloys (Gedge 2008).

Table 1.1. Nominal chemical composition of UNS S32101 stainless steel (Sieurin et al. 2006)

Element	Composition (% weight)
Chromium, Cr	21.5
Nickel, Ni	1.60
Molybdenum, Mo	0.29
Manganese, Mn	4.92
Nitrogen, N	0.23
Carbon, C	0.032
Silicon, Si	0.66
Potassium, P	0.025
Copper, Cu	0.28
Sulfur, S	0.001
Iron, Fe	balance

1.3 Organization of the dissertation

This dissertation is organized as follows. Chapter 2 reviews the existing literature relating to the low homologous temperature stress relaxation behavior of metals. Mathematical and mechanical models to describe long-term behavior from short-term experiments are

introduced and compared. Previous studies carried out to understand the fundamental mechanics of externally-strengthened reinforced concrete pier caps are also elucidated.

Chapter 3 examines fundamental mechanical properties of the UNS S32101 stainless steel that may be necessary to design pretensioned clamp systems. The uniaxial tensile behavior of the material is characterized through a series of experiments, and a Ramberg-Osgood constitutive model is developed for the material. Experiments are also conducted to determine the state of damage (as a function of plastic strain) in the material. The microstructure of the material is also studied using a ferritescope and metallography. The feasibility of using continuum damage mechanics-based stress relaxation models is also explored in this chapter.

Chapter 4 characterizes the low homologous temperature (LHT) stress relaxation behavior of the UNS S32101 stainless steel through a combined experimental and analytical approach. Full-scale experiments are conducted to understand the long-term behavior of the material under ambient temperature conditions. A novel small-scale experiment is then developed and conducted to determine the activation energy associated with stress relaxation. The experimentally-determined activation energy is used to predict the time- and temperature-dependent behavior of the material. A uniaxial viscoplastic constitutive model is developed and one of its parameters is validated by independent experiments.

Chapter 5 illustrates an approach—based on the strut-and-tie analysis—that is capable of calculating the shear capacity of existing and strengthened reinforced concrete pier caps in a consistent and conservative manner. Strengths calculated using the new model are compared to the results of previous experimental studies. Furthermore,

recommendations are made for estimating the pretension force that can be applied to the pier cap structure. A summary of the findings of this study and recommendations for further study are provided in Chapter 6.

Chapter 2

Critical appraisal of previous work

This chapter reviews the present body of literature to gain a deeper understanding of the mechanical behavior and long-term performance of pretensioned strengthening systems that use duplex stainless steel bars. The chapter is divided into four major units. The first part deals with the theoretical mechanisms that drive low homologous temperature (LHT) creep and stress relaxation. Second, mathematical and mechanics-based models—consistent with these theoretical mechanisms—are explored and previous experimental investigations studying stress relaxation in steels and stainless steels are discussed. Third, a case for further experimental investigation into the stress relaxation behavior of the UNS S32101 austenitic-ferritic stainless steel is presented. And finally, previous experimental and analytical studies conducted to understand the mechanical behavior of externally-strengthened reinforced concrete pier caps are elucidated.

2.1 Overview of stress relaxation

Stress relaxation is a complex viscoelastic phenomenon that leads to a gradual decrease in the load of specimen held under a constant deformation (i.e., constant strain) condition. The total strain in a viscoelastic material can be divided into two components—the elastic strain, ε^{e}, and the creep strain, ε^{cr}—and is mathematically given by (Oding et al. 1965):

$$\varepsilon^{tot} = \varepsilon^{e} + \varepsilon^{cr} = \text{constant} \tag{2.1}$$

Stress relaxation manifests in a material when the initial (elastic) strain is gradually replaced by a time-dependent (creep) strain of an equal magnitude (Oding et al. 1965,

Garofalo 1965, Marschall and Maringer 1977), while maintaining a constant total strain (Fig. 2.1). Hence,

$$\frac{d\sigma}{dt} = E\frac{d\varepsilon^e}{dt} \tag{2.2}$$

By solving for ε^e in Eq. (2.1), differentiating the resultant, and substituting it into Eq. (2.2), one finds

$$\varepsilon^{cr} - \varepsilon_0^{cr} = \frac{\sigma_0 - \sigma}{E} \tag{2.3}$$

where ε_0^{cr} is the initial plastic strain. Thus, as σ decreases, ε^{cr} increases proportionally, validating that creep occurs during stress relaxation.

Furthermore, the second law of thermodynamics ensures that the stress relaxation curve always has a negative slope (Bažant and Cedolin 2010). In other words, the slope of the stress relaxation curve cannot increase with time.

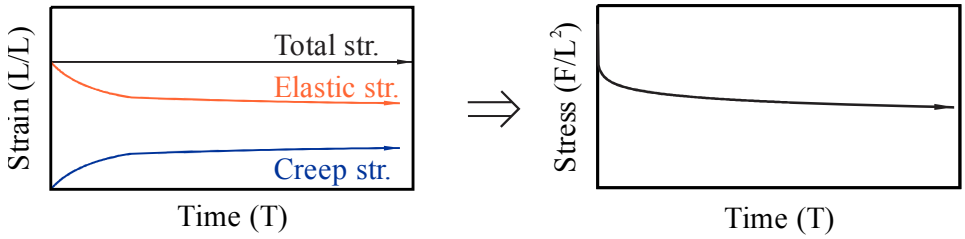

Figure 2.1. Time-dependent stress-strain behavior under constant temperature in a stress relaxation environment

Like all viscoelastic processes, stress relaxation is influenced by such factors as temperature, environmental conditions, and material microstructure (Garofalo 1965). Stress relaxation in metals characteristically begins with a rapid decline in the slope [Region I] followed by a gradual, asymptotic descent [Region II] (Fig. 2.2). The entire relaxation process over an extended time must be modeled using mechanics-based or mathematical models developed from shorter-term experiments.

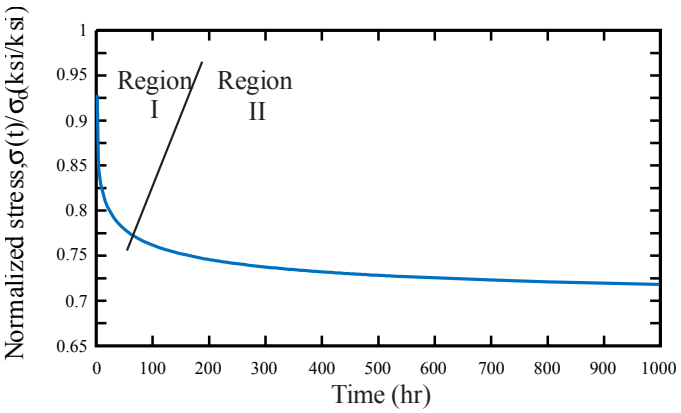

Figure 2.2. Typical stress relaxation curve for a metal

2.2 Mechanics of low homologous temperature stress relaxation

In metals, stress relaxation is a function of temperature (Garofalo 1965, Magura et al. 1962, Neu and Sehitoglu 1992, and Bažant and Yu 2013). In particular, it is dependent on the homologous temperature[1]—defined as the ratio of a material's service temperature to its melting temperature, both on an absolute scale; mathematically, $T_H = T / T_m$. The mechanisms driving creep and stress relaxation can be divided into two regimes: the low homologous temperature regime, or LHT ($T_H < 0.30$) and the high-temperature regime. The focus of the present investigation is stress relaxation that occurs in the LHT regime; the experiments conducted in this study range from 70 °F ($T_H = 0.1773$) to 150 °F ($T_H = 0.204$).

Although creep is more apparent in the high-temperature regime, previous research has shown that, for materials like certain steels and stainless steels, creep occurs at temperatures much lower than the melting temperature [see, for instance, Weihrauch and Hordon (1964), Marschall and Maringer (1977), Yamada and Li (1973), Krempl (1979),

[1] Based on the relationship between creep and stress relaxation established in Eq. (2.1), the terms "low homologous temperature creep" (prevalent in the literature) and "low homologous temperature stress relaxation" (the focus of this study) are used interchangeably.

Neu and Sehitoglu (1992), Krapf (2010), Moser (2011)]. Marschall and Maringer (1977) use the term *microcreep* to describe creep occurring at these low temperatures.

While creep at high temperatures is governed by diffusion mechanisms, LHT creep is controlled by non-diffusion mechanisms (Garofalo 1965). Theories suggest that LHT creep is driven by thermal activation of so-called soft spots and can be modeled using an Arrhenius-type equation (Wyatt 1963, Conrad 1964, Neu and Sehitoglu 1992). In this low-temperature regime, creep strain often is hypothesized to be proportional to the logarithm of time, giving rise to the notion of log creep (Marschall and Marringer 1977, Nabarro 2001). Conversely, in the high-temperature regime, creep strain is proportional to the one-third power of time (Wyatt 1963, Marschall and Marringer 1977). Additional information pertaining to the theoretical mechanisms that govern LHT creep is given in such references as Garofalo (1965), Conrad (1965), and Neu and Sehitoglu (1992).

The main goal of this investigation is to develop design-oriented stress relaxation relationships for an austenitic-ferritic (duplex) stainless steel used for structural strengthening. Hence, the mechanistic and mathematical models considered in this study describe the stress relaxation process in a mostly phenomenological, global manner (as opposed to models that explain the microstructural behavior of the metal).

2.3 Previous experimental studies to characterize stress relaxation in stainless steel

This section summarizes the work conducted by previous researchers who attempted to gain a better understanding of the stress relaxation phenomenon in stainless steel alloys used in various structural engineering applications. First, the experimental methodologies of those studies are described and their findings are succinctly summarized. Then, a brief discussion shows how the proposed research departs from the previous studies and

enhances the current literature on the time-dependent behavior of the UNS S32101 duplex stainless steel.

2.3.1 Review of pertinent experimental studies

Krapf (2010) conducted a series of stress relaxation experiments using the UNS S30400 stainless steel in which the tensile strain in the specimens was kept constant—with the use of a servo-hydraulic testing machine—for a short duration of time. UNS S30400 stainless steel has an austenitic microstructure. The rods were tested in their as-rolled, prismatic shapes (i.e., the rods were not machined or threaded) and had diameters of 0.365 in. The initial strain levels for each test varied from 0.0367 in./in. to 0.1160 in./in., strain values corresponding to stresses developed at 95 and 96 percent of the ultimate tensile stress values, respectively. These tests were preliminary in nature and designed so that stress relaxation would become apparent quickly; such high initial stress levels would not be feasible for practical field installations. The total duration of each test varied between 2 and 4 hours and the tests were conducted at room temperature (approximately 68 °F).

Duplex stainless steels are relatively new materials and, owing to this fact, their stress relaxation behavior has not been widely studied. Only one study (Moser 2011) could be found in the existing literature where the stress relaxation of *duplex* stainless steels was studied. Moser carried out a series of experiments to study the relaxation behavior of two austenitic grades (UNS S30400 and UNS S31600), three duplex grades (UNS S32101, UNS S32205, and UNS S32304), as well as one precipitation-hardened grade (UNS S17700) having a martensitic microstructure. The specimens were tested at a constant temperature of 68 °F using testing frames to maintain constant strain. The strands were tested at only one initial stress—70 percent of the ultimate tensile stress of

each grade—and the duration of each test was 200 hours. A wider range of initial stresses is required for other structural engineering applications (e.g., the design of bridge pier cap strengthening systems). Since the primary focus of Moser's investigation was to study materials for use as prestressing strands in prestressed concrete, strands manufactured through a cold drawing process were used. As recognized by Moser (2011), a previous study by Atienza and Elices (2007) had found that the cold drawing process causes substantial residual stresses to develop across the cross-sectional profile of the material. Additionally, cold worked crystals are harder than annealed ones (Mott and Nabarro 1948); cold working also causes internal strains that aid in the formation of dislocations while hindering their motion (Mott and Nabarro 1948). Hence, drawn specimens would have different creep and stress relaxation properties than rolled specimens (such as the rolled UNS S32101 specimens that are used in the proposed study).

Various other researchers [e.g., Yamada and Li (1973), Nir et al. (1977), Krempl (1979), Idermark and Johansson (1979), Kujawski et al. (1980)] have conducted ambient temperature uniaxial stress relaxation studies on *austenitic* and *martensitic* stainless steel grades. Yamada and Li (1973) studied the stress relaxation behavior of the austenitic UNS S30400 and UNS S31600 stainless steels at 75 °F; Nir et al. (1977) considered austenitic UNS S31600 stainless steel at 77 °F; Krempl (1979) investigated the short-term stress relaxation behavior of austenitic UNS S30400 stainless steel at ambient temperature; Idermark and Johansson (1979) studied the stress relaxation behavior of strip and wire springs composed of the austenitic UNS S30100 and the martensitic UNS S42000 stainless steel grades; and Kujawski et al. (1980) studied austenitic UNS S30400 stainless steel.

2.3.2 Critical appraisal of experimental studies

A review of the existing literature makes it apparent the paucity of experimental data for the stress relaxation behavior of *duplex* stainless steels, which have a dual-phase, austenitic-ferritic microstructure. Although Moser (2011) investigated the stress relaxation behavior of several duplex stainless steel grades, the material used in that study, as reported by Moser, underwent a cold drawing process. Cold-drawn specimens have different creep and stress relaxation properties than rolled specimens. All other studies noted above studied either austenitic or martensitic stainless steels. The durations of the experiments in the literature ranged from a few hours to 200 hours, and all existing stress relaxation experiments for duplex (or even austenitic and martensitic) stainless steels were conducted at temperatures of approximately 70 °F.

Additionally, all the previous stress relaxation studies surveyed in the literature considered a very limited range of initial stresses. For example, Krapf's (2010) tests had initial stress levels between 94 and 96 percent of the ultimate tensile stress of the material and Moser's (2011) strands were tested at only one initial stress, 70 percent of the ultimate tensile stress of each grade. None of the investigations reviewed offer usable models to guide the design and installation of bridge pier cap strengthening systems that use duplex stainless steel bars.

2.4 Mathematical and mechanistic modeling of stress relaxation

Stress relaxation in metals is a gradual process, taking long periods of time to achieve asymptotic behavior. Due to time constraints, models developed from shorter duration tests are used to extend the stress relaxation curves to time periods of interest. These models are mechanistic or mathematical in nature and describe the underlying,

phenomenological causes that drive stress relaxation. This section explores some models that are suitable for use with metals like the UNS S32101 stainless steel.

2.4.1 Viscoelastic constitutive models

Rheological models provide a powerful, yet simple, way of describing the time-dependent constitutive behavior of viscoelastic materials. These models describe the overall viscoelastic phenomenon rather than attempt to describe the micromechanical mechanisms that drive viscoelastic behavior (Bažant and Cedolin 2010). Composed of linear springs and viscous dashpots, these rheological models can be derived from the following fundamental stress-strain relationships (Findley et al. 1976):

- For a linear spring the relationship is $\sigma = E_1 \varepsilon$, where E_1 can be interpreted as the linear spring constant; and,
- The constitutive relationship for a linear viscous dashpot is $\sigma = \eta_1 \dot{\varepsilon}$, where η_1 is the coefficient of viscosity and $[\dot{x}] = dx/dt$.

Most types of viscoelastic behavior can be described using a model containing a combination of springs and dashpots (Roscoe 1950; Findley et al. 1976). Table 2.1 summarizes several basic rheological models as well as their associated analytical forms describing stress relaxation (derived based on the condition that $\varepsilon(t) = \varepsilon_0$). Unfortunately, analysis of data obtained from preliminary stress relaxation tests conducted in the present study showed that none of the basic rheological models described in Table 2.1 have sufficient degrees of freedom (dof) to adequately capture the long-term stress relaxation behavior of the UNS S32101 duplex stainless steel. While a generalization of the Maxwell model might describe the material's stress relaxation behavior, such a model would require multiple parallel chains and, hence, many variables (E_i and η_i) would need

to be determined. Thus, models with fewer variables that, nonetheless, are capable of adequately characterizing the long-term stress relaxation behavior of the UNS S32101 duplex stainless steel are explored further; such models would make better candidates for inclusion in guide specifications for the design and installation of pretensioned pier cap rehabilitation systems, where simplicity is warranted.

Table 2.1. Summary of rheological models for viscoelasticity [solutions derived in Findley et al. 1976 and Christensen 1971]

Model type	Analytical expression for stress relaxation
Maxwell 	$\sigma(t) = \sigma_0 \exp\left(\frac{-E_1 t}{\eta_1}\right)$
Kelvin–Voigt 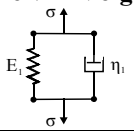	$\sigma(t) = \sigma_0 + \eta_1 \varepsilon_0 \delta(t)$ where $\delta(\cdot)$ is the Dirac delta function
Burgers (four-element) 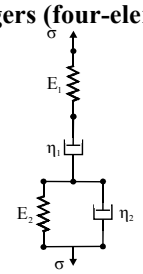	$\sigma(t) = \frac{\varepsilon_0}{A}\left[\left(q_1 - q_2 r_1\right)\exp\left(-r_1 t\right) - \left(q_1 - q_2 r_2\right)\exp\left(-r_2 t\right)\right]$ where $r_1 = (p_1 - A)/2p_2$ $r_2 = (p_1 + A)/2p_2$ $A = (p_1^2 - 4p_2)^{1/2}$ and $p_1 = \frac{\eta_1}{E_1} + \frac{\eta_1}{E_2} + \frac{\eta_2}{E_2}$ $p_2 = \frac{\eta_1 \eta_2}{E_1 E_2}$ $q_1 = \eta_1,\ q_2 = \frac{\eta_1 \eta_2}{E_2}$
Standard (Linear) Solid 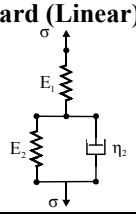	$\varphi(t) = \alpha + \beta \exp\left(-\mu t\right),$ and $\varphi(t) = \frac{\sigma(t)}{\sigma_{initial}}$
Generalized Maxwell (parallel-type) 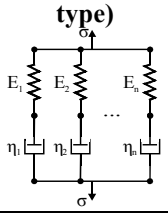	$\sigma(t) = \varepsilon_0 \sum_{i=1}^{n} E_i \exp\left(-\frac{E_i}{\eta_i} t\right)$
Modified Standard Solid (Chun and Hubbard 2009) 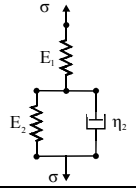	$\varphi(t) = \alpha + \beta \exp\left(-\mu t^q\right),$ and $\varphi(t) = \frac{\sigma(t)}{\sigma_{initial}}$

2.4.2 Temperature dependence of stress relaxation curves

Exposed stainless steel bars on bridge pier caps undergo daily and seasonal temperature changes. It has been found that for carbon prestressing strands the flow of metals (and, hence, stress relaxation) is accelerated by an increase in temperature (Bažant and Yu 2013). A study by Schwier (1958) found that an increase in temperature from 72 °F to 212 °F would amplify relaxation losses in carbon steel by a factor of eight. Although the metallurgy of carbon steel prestressing strands is different from austenitic-ferritic stainless steel bars, preliminary experimental results from this study lend credence to the hypothesis that an increase in temperature would have a marked effect on the stress relaxation behavior of the UNS S32101 stainless steel.

One limitation of all basic rheological models is that they are not capable of describing the influence of time-dependent changes in temperature on the overall asymptotic behavior of a stress relaxation curve. Simply put, the parameters developed using the basic rheological models are applicable only for the specific environmental parameters during the test and cannot adequately model changes in temperature during experiments. Hence, the literature was surveyed to identify models that are capable of characterizing the effects of varying temperature during a relaxation experiment.

2.4.3 Kinetic model for logarithmic stress relaxation

As noted previously, at low homologous temperatures (i.e., $T_H < 0.30$), thermally activated mechanisms control creep. In this temperature regime, creep strain can be characterized by a logarithmic relationship:

$$\sigma = \sigma_0 - \alpha_r \ln(1 + v_r t) \tag{2.4}$$

where σ_0 is the initial stress and α_r and v_r are constants independent of time. The parameter α_r is not sensitive to the initial stress; but the frequency factor, v_r, is sensitive to σ_0 as well as temperature. For creep, these parameters have been characterized by the following relationships (Neu and Sehitoglu 1992):

$$\alpha = \alpha_0 RT \frac{S}{\sigma_e} \tag{2.5}$$

$$v = v_o \exp\left(\frac{-(Q_c - h\sigma_e)}{RT}\right) \tag{2.6}$$

where S is the deviatoric stress; σ_e, the equivalent stress; Q_c the activation energy for LHT creep; and a_0, v_0, and h are creep constants specific to the material. These relationships can be modified for stress relaxation if $\alpha_r \approx E\alpha$ (Garofalo 1965). E is the modulus of elasticity. Hence,

$$\alpha_r = E\alpha_0 RT \frac{S}{\sigma_e} \tag{2.7}$$

$$v_r = v_{ro} \exp\left(\frac{-(Q_r - h\sigma_e)}{RT}\right) \tag{2.8}$$

As with creep, Q_r is the activation energy associated with LHT stress relaxation. Yet, because no existing studies have validated the assumption that $\alpha_r \approx E\alpha$ for duplex stainless steels this model is not used to characterize the stress relaxation behavior of the UNS S32101 stainless steel considered in this study.

2.4.4 Bažant and Yu (2013) viscoplastic constitutive model

The failure of the Koror-Babeldaob Bridge in Palau in 1977 highlighted the necessity of considering the influence of varying strain and temperature on carbon steel prestressing strands when designing large-span bridges (Bažant and Yu 2013). Existing methods used

to calculate stress relaxation in prestressing strands—e.g., the CEB-fib (1990) and the so-called American practice formulae (Magura et al. 1964)—are valid only for constant strain and temperature. Hence, Bažant and Yu (2013) developed an improved relaxation model based on viscoplasticity theory. While formulae are presented for both the varying strain and varying temperature cases, this study assumes a negligible variation in strain (Park and Paulay 1975, Razak 1986, Shams 2000). Mathematically, the new stress relaxation function is given as (Bažant and Yu 2013):

$$\sigma = \min(\gamma f_y^{'}, \sigma_0) + f_y^{'} \left\langle \frac{\sigma_0}{f_y^{'}} - \gamma \right\rangle \left[1 + \frac{\rho}{c} \left(\frac{t}{\lambda} \right)^k \right]^{-c} \tag{2.9}$$

where $\gamma f'_y$ is the stress level below which relaxation stops, σ_0 is the initial stress, and the remaining variables are parameters determined empirically from 1,000-hour experiments. Additionally, $\langle\ \rangle$ are the Macauley brackets, defined as $\langle x \rangle = \max(x, 0)$. The parameter γ is typically taken as 0.55 for prestressing strands (Magura et al. 1962). The dependence of temperature is characterized through the use of the Arrhenius equation and the activation energy of flow, replacing the real time, *t*, in Eq. (2.9) with an effective time,

$$t = \int_{\tau'=0}^{\tau} A_T(\tau') d\tau' \tag{2.10}$$

where τ is the real time and A_T, the Arrhenius factor, is defined as

$$A_T(t) = \exp\left[\frac{Q_{sr}}{k_B T_0} - \frac{Q_{sr}}{k_B T(t)} \right] \tag{2.11}$$

Here, Q_{sr} is the activation energy of flow; k_B the Boltzmann constant; and T_0 the reference temperature (294.2 K in the present study). An advantage of this model is that, because of its provenance, it is well suited for ready integration into existing guide

specifications and structural engineering design codes (Bažant and Yu 2013). However, this model has been developed and validated only for carbon steel prestressing strands. The present study will validate this model for austenitic-ferritic stainless steel bars.

2.4.5 Continuum damage mechanics-based model

Continuum damage mechanics (CDM) offers an alternative approach to describe stress relaxation under varying temperature conditions. Initially proposed by Kachanov (1958) and Rabotnov (1969) to model the creep rupture phenomenon—and later expanded through the works of Lemaitre (1984), Chaboche (1988), and other researchers to include a thermodynamic formulation to characterize damage—it introduces a new internal variable to relate material (microstructural) damage to easily measurable (global) mechanical quantities such as the modulus of elasticity (Kachanov 1986; Bhattacharya and Ellingwood 1999).

Though the damage variable is represented as a tensor, this study is only concerned with the case of uniaxial loading, where the damage variable is reduced to a scalar quantity, D. The constitutive equation for damaged materials is formulated using the strain equivalence principle, which states: "Any constitutive equation for a damaged material may be derived in the same way as for a virgin material except that the usual stress [σ] is replaced by the effective stress [$\tilde{\sigma}$]" defined as (Lemaitre 1996; Bhattacharya and Ellingwood 1999),

$$\tilde{\sigma} = \frac{\sigma}{1 - D} \tag{2.12}$$

Likewise, this principle can be applied to the effective elastic strain to determine an effective elastic modulus, $\tilde{E}$, for damaged materials (Bhattacharya and Ellingwood 1999):

$$\tilde{E} = E(1-D) \tag{2.13}$$

Using this definition of the effective elastic modulus, the state of damage can be found by determining the modulus of elasticity by a tension test (Fig. 2.3).

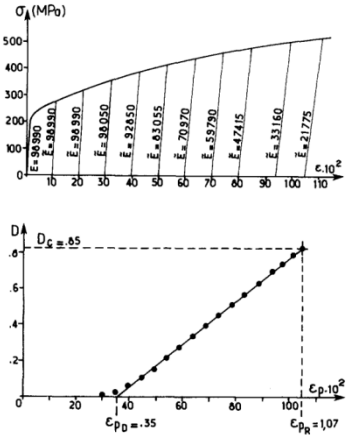

Figure 2.3. Evolution of ductile plastic damage of a copper alloy (Lemaitre 1984)

A constitutive law for stress relaxation can be formulated from the existing creep-damage equations proposed by Kachanov (1958) and later enhanced by Rabotnov (1969). Rabotnov (1969) found that the creep rate is dependent on the current state of stress as well as damage, and has the form:

$$\frac{d\varepsilon^{cr}}{dt} = \frac{d\varepsilon^{cr}(\sigma, D)}{dt} \tag{2.14}$$

Accounting for the damage process by the use of a differential equation that describes the evolution of damage, the creep strain rate and damage rate can be expressed (in the form given by Naumenko and Altenbach 2007) as:

$$\frac{d\varepsilon^{cr}}{dt} = \frac{K\sigma^n}{(1-D)^m} \tag{2.15}$$

$$\frac{dD}{dt} = \frac{A\sigma^p}{(1-D)^q} \tag{2.16}$$

Kachanov (1958) suggested that the influence of variable temperature on the creep and damage processes can be approximately accounted for by letting K and A be functions of temperature. Naumenko and Altenbach (2007) proposed the following Arrhenius-type equations for these functions:

$$K(T) = K_0 \exp\left[\frac{-Q_{cr}}{k_B T}\right] \tag{2.17}$$

$$A(T) = A_0 \exp\left[\frac{-Q_D}{k_B T}\right] \tag{2.18}$$

where Q_{cr} and Q_D are the activation energies associated with the creep and damage processes, respectively.

Guo et al. (2012) used the relationship between creep and stress relaxation established in Eq. (2.1) to derive relationships for stress rate and the stress relaxation-damage constitutive equation. The equation for stress rate can be written in the following manner, where E is the modulus of elasticity,

$$\frac{d\sigma}{dt} = -\left[A\frac{\sigma^{p+1}}{(1-D)^{q+1}} + EK\frac{\sigma^{n}}{(1-D)^{m-1}}\right] \tag{2.19}$$

Similarly, the stress relaxation-damage constitutive equation is given by,

$$\frac{d\sigma}{dD} = -\left[\frac{\sigma}{1-D} + \frac{EK}{A}\frac{\sigma^{n-p}}{(1-D)^{m-q-1}}\right] \tag{2.20}$$

in which $\sigma(t=0) = \sigma_0$.

The continuum damage mechanics approach is particularly attractive for the purposes of this study because it allows for direct experimental and analytical characterization of the relaxation damage in both the threaded and unthreaded regions of the bars. However, this approach characteristically requires the assumption that the

microstructural damage in the material due to creep is large enough to be detected by one of the macroscopic techniques discussed by Lemaitre (1996)—e.g., measurement of the variation in the elastic modulus by a direct tension test, change in density, etc. It should be noted that although Eqs. (2.19) and (2.20) do not include the Arrhenius-type temperature dependence, such dependence can be introduced into the model using a similar derivation. Additionally, to include the primary, as well as secondary and tertiary states of creep, the Othman and Hayhurst (1990) creep damage constitutive equations can be used to derive the relationships for the stress rate and the stress relaxation-damage constitutive equations:

$$\frac{d\varepsilon^{cr}}{dt} = G\left(\frac{\sigma}{1-D}\right)^{n} t^{m} \tag{2.21}$$

$$\frac{dD}{dt} = C\frac{\sigma^{\chi}}{(1-D)^{\varphi}} t^{m} \tag{2.22}$$

In Eqs. (2.21) and (2.22), G and C can be thought of as functions of temperature. An additional summary of various other creep-damage models is given in Kostenko et al. (2006).

2.4.6 Bažant and Yu (2013) approach for determining activation energy

The Bažant and Yu (2013) model is based on viscoplasticity theory and relies on an Arrhenius-type equation to describe temperature-dependent stress relaxation behavior. The authors rely on stress relaxation data from a Japanese strand manufacturer (SHINKO Wire Co. Ltd.) to determine the activation energy associated with stress relaxation for carbon prestressing strands. The SHINKO experiments involved loading several carbon prestressing wires to the same initial strain, but each at a different temperature [i.e., 20 °C (68 °F), 40 °C (104 °F), 60 °C (140 °F), and 80 °C (176 °F)].

To fit their model to the SHINKO experimental data, Bažant and Yu first plot the percent relaxation as a function of time, t (Fig. 2.4a). Next, the times to reach a particular amount of loss [e.g., 4% relaxation was used as the target loss by Bažant and Yu (2013)] for each temperature are extracted. The natural logs of the times corresponding to the target loss are then plotted against the reciprocal of temperature, $1/T$, and the slope of the linear regression line yields the quantity Q/k_B, where Q is the activation energy associated with stress relaxation process and k_B is the Boltzmann constant (Fig. 2.4b).

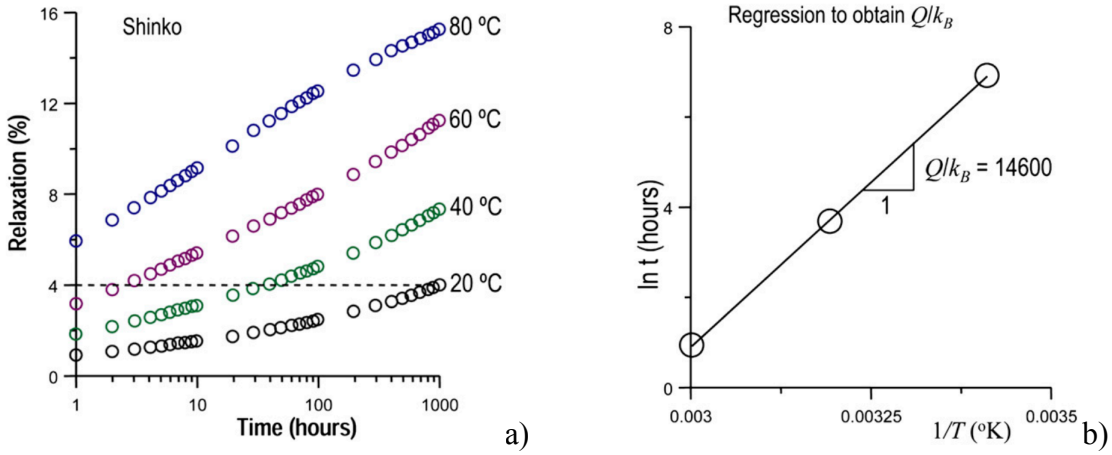

Figure 2.4. a) Relaxation at different temperatures, showing times required to reach 4% stress relaxation; and b) Regression plot giving Q/k_B [from Bažant and Yu (2013)]

Among the advantages of this approach is the simplicity associated with both the experiments and modeling aspects. Furthermore, the Bažant-Yu approach does not require differentiating stress (or strain) with respect to time; computing these derivatives from experimental data may be rather difficult. However, a potential drawback of this method is that it requires that several specimens be loaded to the *same* initial strain (at various constant temperatures) for long time durations (e.g, 1,000 hours). This would limit the repeatability of experiments when attempting to validate the activation energy at multiple temperatures as well as multiple initial strains.

2.4.7 Summary of mathematical and mechanistic models for stress relaxation

Four different approaches for modeling the low homologous temperature stress relaxation behavior of metals have been reviewed. Rheological models—the most basic models—are not capable of capturing time-dependent changes in temperature. Bažant and Yu's (2013) viscoplastic model is particularly attractive for use in design, as it is relatively simple in its formulation and has been successfully used in the past to describe stress relaxation in metals. Lastly, the Bažant and Yu (2013) approach for determining the activation energy for stress relaxation is summarized; some potential drawbacks associated with this approach are outlined and the need for an alternative method is established. This method will be introduced subsequently in Section 4.3.1.

2.5 Mechanics of reinforced concrete bridge pier caps

The primary goal of this research is to facilitate the development of a stainless steel-based system to enhance the shear strength of existing reinforced concrete bridge pier caps. This section briefly reviews some previous work conducted to understand the behavior of reinforced concrete pier caps.

2.5.1 Pier caps as deep beams

The behavior of reinforced concrete beams is dependent on their shear span-to-effective depth ratio, or a/d ratio (ASCE-ACI Committee 445 on Shear and Torsion 1998). In particular, beams with a/d ratios less than approximately 2.5—known as "deep beams"—fail in shear through the formation of an arch action, as opposed to a beam action (MacGregor and Wight 2005). The reinforced concrete pier caps analyzed in this investigation have $a/d < 2.5$ and, hence, behave structurally as deep beams.

The American Association of State Highway and Transportation Official's (AASHTO) *LRFD Bridge Design Specifications* (AASHTO 2010) permits the use of the following methods to evaluate the shear capacity of reinforced concrete beams:

- the simplified procedure for nonprestressed sections (§5.8.3.4.1);
- the general procedure (§5.8.3.4.2);
- the simplified procedure for prestressed and nonprestressed sections (§5.8.3.4.3); and
- the strut-and-tie model (§5.6.3).

A detailed review of each of these methods is provided in Bechtel (2011). The strut-and-tie approach is considered here, because previous studies have shown it to be a more appropriate method to assess the capacity of existing bridge substructures with short shear spans (O'Malley, 2011; Bechtel, 2011).

The strut-and-tie approach, originally developed by Schlaich et al. (1967), entails transforming a reinforced concrete member to an equivalent truss system consisting of compression struts, tension ties, and nodal zones where multiple elements intersect. Further details are provided in Bechtel (2011) and Kim (2014).

2.5.2 Experimental investigations to improve shear strength of bridge pier caps

The state of Georgia's system for improving the shear strength of bridge pier caps uses external pretensioned hot-dipped galvanized steel bars to transform the pier cap structural resistance from a single-strut mechanism to a double-strut mechanism (Fig. 2.5). O'Malley (2011) conducted a series of full-scale tests to understand the behavior of pier caps having such an external pretensioned bar clamp system that used carbon steel bars.

Intended to replicate a typical pier cap, the experiments involved reinforcement schemes similar to those found in Georgia bridges constructed in the middle part of the last century (O'Malley 2011). O'Malley's experiments showed that the presence of external shear reinforcement allowed a double-strut mechanism to form and permitted an increase in the shear capacity of strengthened pier caps. While linear-elastic carbon steel bars were used in that study, its findings and tools can used as a basis to form design guidelines for constitutively nonlinear stainless steel-based strengthening systems.

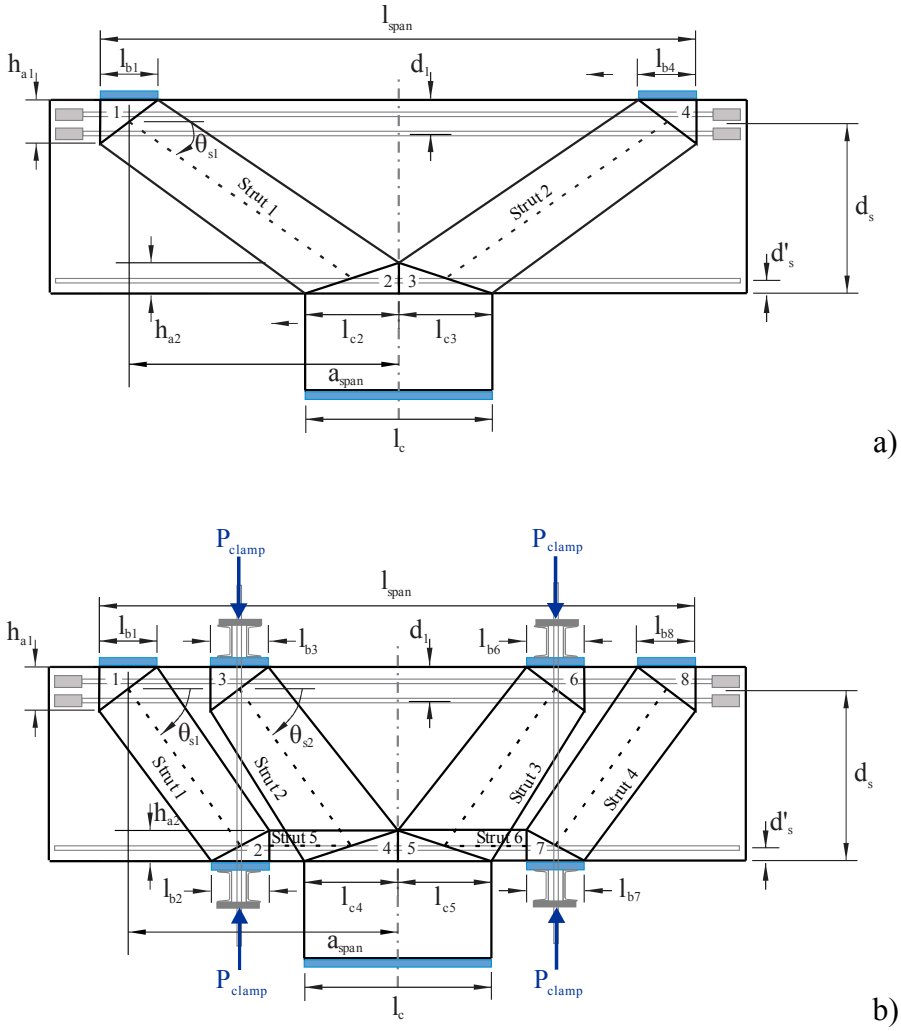

Figure 2.5. Strut-and-tie model of: a) original bridge pier cap; and b) strengthened bridge pier cap

2.6 Summary

In this chapter, the mechanics of low homologous temperature (LHT) stress relaxation were reviewed. Several models capable of describing the long-term stress relaxation behavior of the UNS S32101 stainless steel were also described. Finally, the mechanical behavior of reinforced concrete pier caps with external strengthening systems was explored. In the following chapters, we will examine the time-independent and time-dependent (stress relaxation) properties of the UNS S32101 stainless steel.

Chapter 3

Properties of UNS S32101 stainless steel as a structural material

The UNS S32101 stainless steel is a duplex alloy, meaning that its microstructure is nominally composed of equal parts of austenitic and ferritic grains. Owing to its relatively recent vintage, this grade has not been exhaustively tested to determine the mechanical properties that are useful for structural engineering applications, such as bridge pier cap rehabilitation and retrofitting. In this chapter, experiments are conducted to determine some fundamental material parameters of this particular alloy. These tests yield a set of material parameters that are necessary to design stainless steel-based structural rehabilitation systems. The experimental procedures followed and the results obtained from each test are discussed in the following sections.

3.1 Tensile testing of as-received material

A series of uniaxial tests were conducted at room temperature to determine the tensile properties of the UNS S32101 material. The material was received in two batches, the first containing round bars having diameters of 0.75 in. and the second containing round bars having diameters of 1.25 in. The bars from each batch underwent different annealing conditions. Three bars from the first batch (0.75 in. diameter bars) and four bars from the second batch (1.25 in diameter bars) were tested.

3.1.1 Experimental procedure

All seven bars were tested in a 200-kip Baldwin screw jack-type uniaxial test frame. An extensometer with a 1 in. gage length with a ±0.15 in. extension was used to measure low levels of strain. Additionally, a high-definition video camera was used to measure strains up to fracture using a video extensometer technique.

The tensile tests were conducted in accordance with ASTM Standard E8 (2009) to determine the full-range stress-strain relationship of the UNS S32101 bars. The bars were tested in an as-rolled, prismatic shape (as opposed to a milled, dogbone shape) in a screw jack test machine (Figs. 3.1 and 3.2). For the initial portion of the tests, the strain in the specimens was measured using an extensometer having a gauge length of 1 in. The extensometer used had a maximum travel distance of 0.15 in. (corresponding to a maximum strain of 0.15 in./in.), far lower than the rupture strains shown in Table 3.1. Hence, a novel video extensometer technique, like the one used by Zureick et al. (2014), was used to measure higher levels of strain.

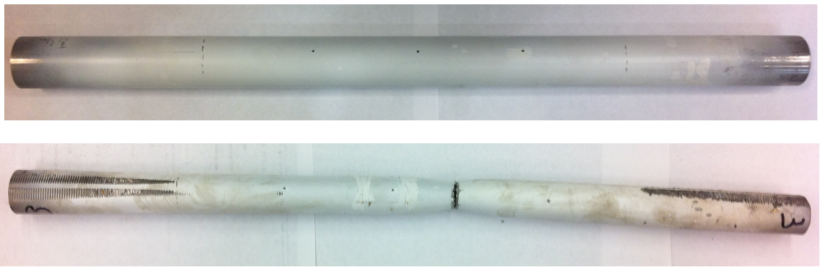

Figure 3.1. Specimen having a 1.25 in. diameter: a) prior to testing; b) after testing (failure)

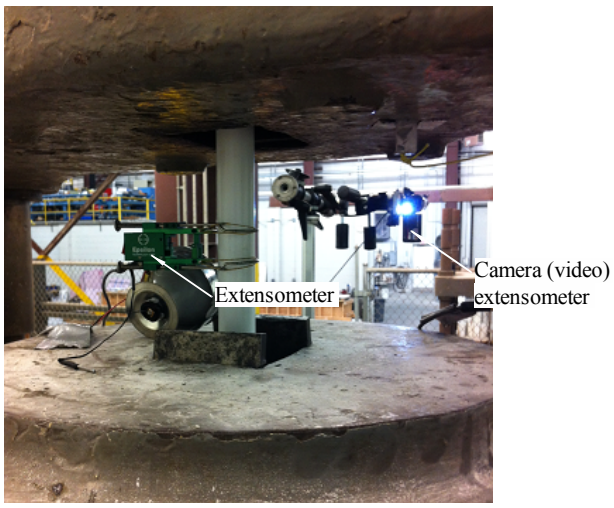

Figure 3.2. Experimental setup in screw-jack (Baldwin) test frame

3.1.2 Video extensometer

The first element of the video extensometer consists of a stationary (high-resolution) camera to record the deformation of a specimen (Fig. 3.3a). Part of the specimen—the gage section—is coated with a white paint; two black dots placed along the center of the specimen mark the gage length (Fig. 3.3b). Still images of the video are then generated at the same rate as data is acquired from the loading frame to allow for synchronicity between the two systems. For each still frame, the center of each dot is assigned a position on the Cartesian coordinate system. The spacing of the dots from the first frame of the video is used to calculate the initial gage length, L_0 (Fig. 3.3b):

As the specimen is loaded, the initial, circular dots elongate, becoming elliptical. The vertical center of the ellipse is assumed to lie on the same material point as the center of the initial circular dot. Using the coordinate locations of the displaced dots, the engineering strain value (in pixels/pixels) at that time point is calculated as (Fig. 3.3c):

$$\varepsilon = \frac{\Delta L}{L_0} = \frac{(y_a + \Delta y_a) - (y_b - \Delta y_b)}{L_0} \tag{3.1}$$

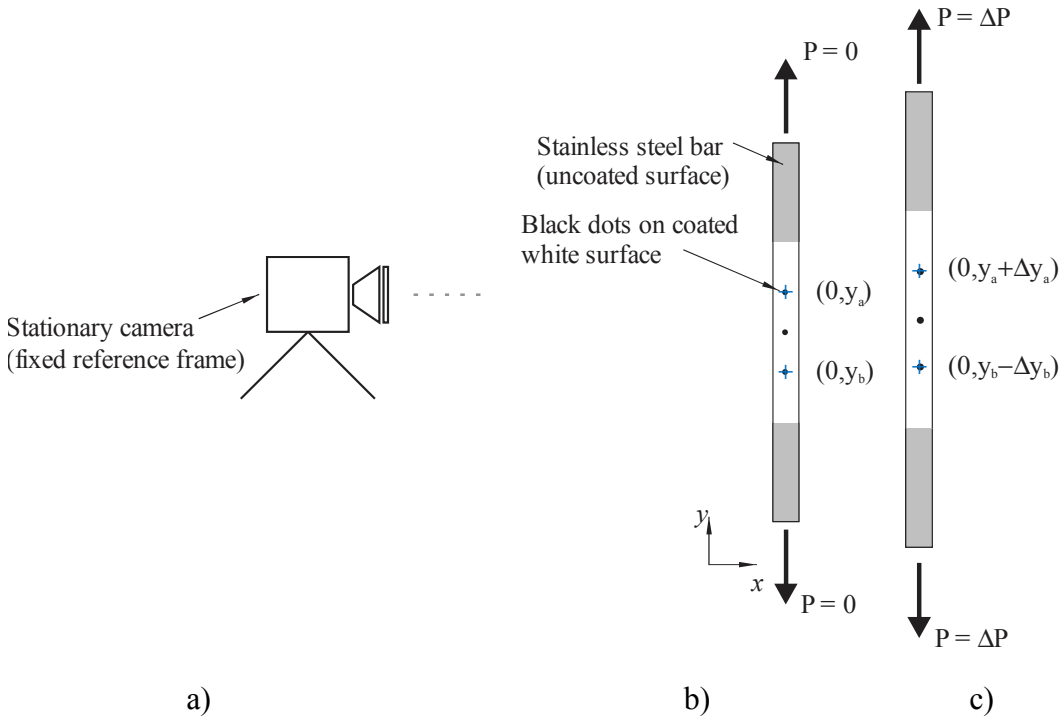

Figure 3.3. Components of the video extensometer system: a) a high-definition camera; b) an unloaded (undeformed) specimen with black dots to mark the gage length; and c) a loaded (deformed) specimen

3.1.3 Results

Stress-strain curves obtained from these tensile tests are presented in Fig. 3.4a for the bars having a 0.75 in. diameter and Fig. 3.4c for the bars having a 1.25 in. diameter. Additionally, a summary of the key results is provided in Table 5.1. The results show that the material has a high strain-hardening capability and a high strain at failure.

The initial modulus of elasticity, calculated in accordance with ASTM standard E111-04 (2010), is the slope of a linear regression curve generated between strain values of 0.0 in./in. and 0.0009 in./in. An upper limit of $\varepsilon = 0.0009$ in./in. is chosen, for the stress-strain curves begin exhibiting a degree of nonlinearity beyond that strain. Note that the tensile tests for the 0.75 in. and 1.25 in. diameter bars were subjected to different annealing conditions during manufacturing.

3.1.4 Mathematical constitutive relationship

Stainless steel has a nonlinear constitutive relationship. Mathematically, it can be modeled by a relationship like the Ramberg-Osgood equation (Ramberg and Osgood 1942). In particular, a form given in ASCE 8-02 (2002) is used:

$$\varepsilon = \frac{\sigma}{E_0} + 0.002\left(\frac{\sigma}{\sigma_{0.2}}\right)^n \tag{3.2}$$

where ε is strain; σ the stress; E_0 the initial modulus of elasticity; $\sigma_{0.2}$ the 0.2% offset proof stress; and n, a parameter to capture the sharpness of the knee, is calculated as follows:

$$n = \frac{\log\left(0.002/0.0001\right)}{\log\left(\sigma_{0.2}/\sigma_{0.01}\right)} \tag{3.3}$$

and $\sigma_{0.01}$ is the 0.01% offset proof stress.

Table 3.2 provides a summary of the average Ramberg-Osgood parameters developed from two bars having diameters of 0.75 in. and three bars having diameters of 1.25 in. Samples having Specimen IDs of 075-2101-19 and 125-2101-05 were not included in the analysis as a data acquisition error precluded the collection of data below strain levels of 0.0003 in./in. Hence, it was difficult to determine the initial modulus of elasticity for those specimens. Using an average value of the initial modulus of elasticity, 0.2% offset proof stress, and the knee parameter, the following constitutive equation is recommended for the 0.75 in. bars (Fig. 3.4b):

$$\varepsilon = \frac{\sigma}{27272\,\text{ksi}} + 0.002\left(\frac{\sigma}{85.7\,\text{ksi}}\right)^{5.92} \tag{3.4}$$

Similarly, the following constitutive relationship is recommended for the 1.25 in. bars (Fig. 3.4d):

$$\varepsilon = \frac{\sigma}{27554\,\text{ksi}} + 0.002\left(\frac{\sigma}{88.3\,\text{ksi}}\right)^{7.03} \tag{3.5}$$

Eqs. (3.4) and (3.5) are valid for stresses below the 0.2% offset yield stress (i.e., $\sigma \le \sigma_{0.2}$).

Table 3.1. Summary of UNS S32101 lean duplex stainless steel rod tensile tests

Specimen ID	Avg. diameter (in.)	0.5% tensile stress (ksi)	Ult. tensile stress (ksi)	Rupture strain (in./in.)
075-2101-00	0.752	85.3	105.3	0.383
075-2101-01	0.752	85.0	105.5	0.388
075-2101-19	0.752	87.2	106.0	0.391
125-2101-02	1.252	84.7	115.0	0.334
125-2101-03	1.251	88.4	116.4	0.366
125-2101-04	1.252	90.2	116.9	0.389
125.2101-05	1.252	89.2	115.0	0.378

Table 3.2. Summary of UNS S32101 Ramberg-Osgood parameters

Specimen ID	Modulus of elasticity (ksi)	0.2% proof stress (ksi)	0.01% proof stress (ksi)	n
075-2101-00	27,020	86.1	51.8	5.89
075-2101-01	27,525	85.3	51.6	5.96
125-2101-02	27,139	84.4	56.8	7.56
125-2101-03	27,532	89.2	56.7	6.61
125-2101-04	27,991	91.3	59.2	6.91

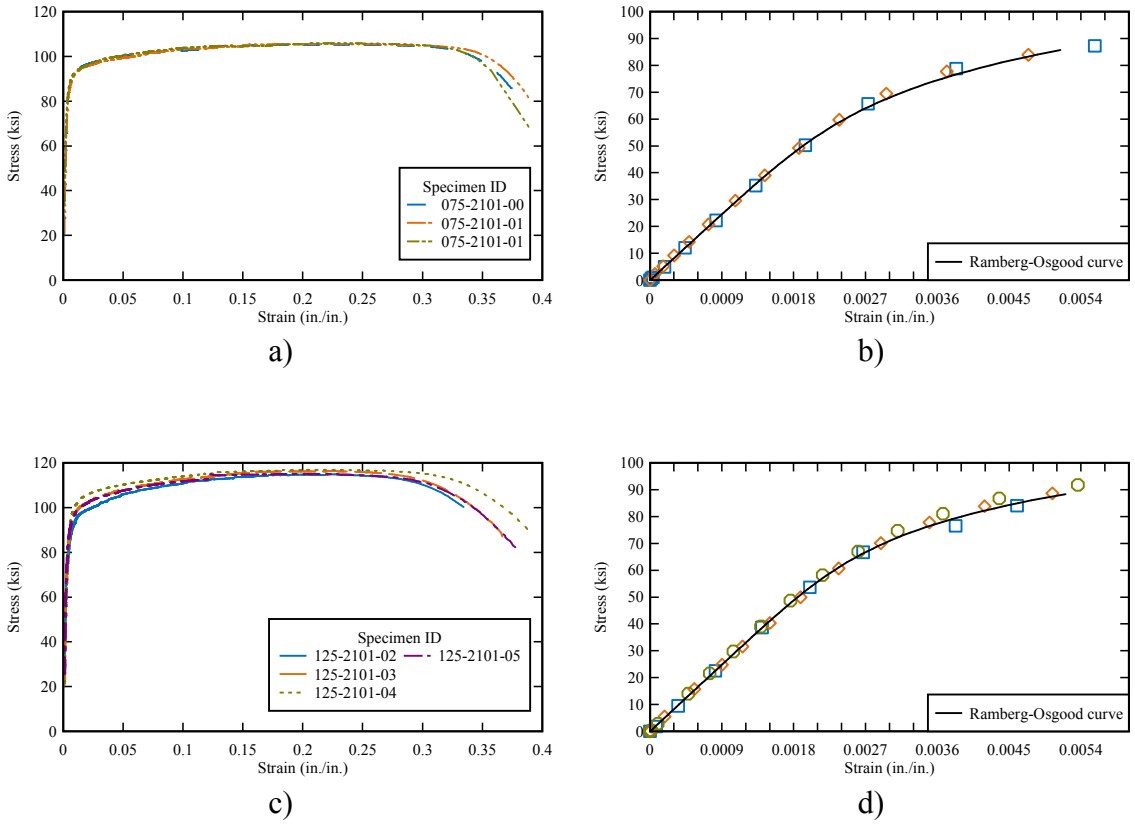

Figure 3.4. Tensile stress-strain relationships for UNS S32101 bars with diameters: a) 0.75 in. (full range); b) 0.75 in. ($\sigma \leq \sigma_{0.2}$); c) 1.25 in. (full range); d) 1.25 in. ($\sigma \leq \sigma_{0.2}$);

3.2 Uniaxial testing of material previously subjected to sustained loading

As described in Chapter 2, continuum damage mechanics (CDM) is based on the evolution of an internal variable for damage. Eq. (2.14), defining the effective elastic modulus, offers a way to determine the state of ductile damage by determining the modulus of elasticity by a tension test (Fig. 2.3). A similar approach is used to determine the state of damage in a material that has undergone stress relaxation.

Similar to the strain equivalence principle for ductile damaged materials, Bhattacharya (1997) proposed a strain equivalence principle for materials damaged due to creep: "A damaged volume of material under the applied stress [σ] shows the same

creep strain rate at a given time and temperature as a comparable undamaged volume under the effective stress [$\tilde{\sigma}$] at the same time and temperature." Hence, since creep and stress relaxation are different manifestations of the same phenomenon, an attempt is made to validate the feasibility of determining the state of damage in a material that has undergone stress relaxation through a direct tension test. Specifically, the slope of the unloading curve of a specimen that has undergone stress relaxation for a particular amount of time (e.g., 5 hours) is measured. According to the strain equivalence principle (Bhattacharya 1997), a reduced initial elastic modulus should be apparent in the material damaged by stress relaxation. Creep—and, correspondingly, stress relaxation—is a damage-driven process (Oding et al. 1965).

It should be noted that the damage variable (D) calculated from the results of this test would include the combined effects of time-independent plastic damage (D_p^{ti}) and creep damage (D_p^{cr}),

$$D = D_p^{ti} + D_p^{cr} \tag{3.6}$$

Thus, to isolate the damage due to permanent creep, the state of damage due to time-independent plastic damage must be subtracted from the total damage:

$$D_p^{cr} = D - D_p^{ti} \tag{3.7}$$

No study could be found in the literature where such an approach has been used to determine verification points for the evolution of creep damage. This research undertakes the task to establish the feasibility of modeling the low homologous temperature stress relaxation of the UNS S32101 alloy using CDM.

3.2.1 Time-independent plastic damage of UNS S32101 material

A material subjected to creep loading undergoes both time-independent plastic damage—damage caused by loading it to its initial stress—and time-dependent creep damage. As shown by Eq. (3.7), computing damage caused by the effects of creep alone requires knowledge of the time-independent plastic damage, D_p^{ti}. So to characterize the evolution of the time-independent damage component of the UNS S32101 stainless steel, a CDM-type tensile test was conducted. In this test (Fig. 3.5), the material is repeatedly loaded to increasing stress levels and unloaded to a condition where stress vanishes. The damage, then, is characterized by the change in the elastic modulus of the unloading portion of the curve the material (Lemaitre 1996; Bhattacharya and Ellingwood 1999) using the following relationship:

$$D = 1 - \frac{\tilde{E}}{E} \tag{3.8}$$

where $\tilde{E}$ is the effective elastic modulus defined in Eq. (2.13).

The test was conducted using an MTS universal testing frame; load was measured using a 55 kip load cell; and strain was measured using an extensometer having a 1 in. gage length. Additionally, the specimen was loaded to 16 strain levels using a strain-controlled feedback loop at a rate of 0.015 in./in./min [ASTM E8 (2009)] and unloaded using a load-controlled feedback loop at a rate of 83 lb/min [ASTM E8 (2009)]. All modulus values were calculated in accordance with ASTM standard E111-04 (2010).

The evolution of time-independent plastic damage in the material past the 0.00567 in./in. level is shown in Fig. 3.6. (It should be noted that the highest initial strain level for the stress relaxation experiments conducted in this investigation is 0.004 in./in.) The results indicate that no appreciable time-independent plastic damage occurred below

plastic strain levels of 0.00567 in./in. (i.e., the value of the modulus does not change from the original). Alternatively, any damage measured from a stress relaxation experiment must be wholly due to creep damage,

$$D_p^{cr} = D \tag{3.9}$$

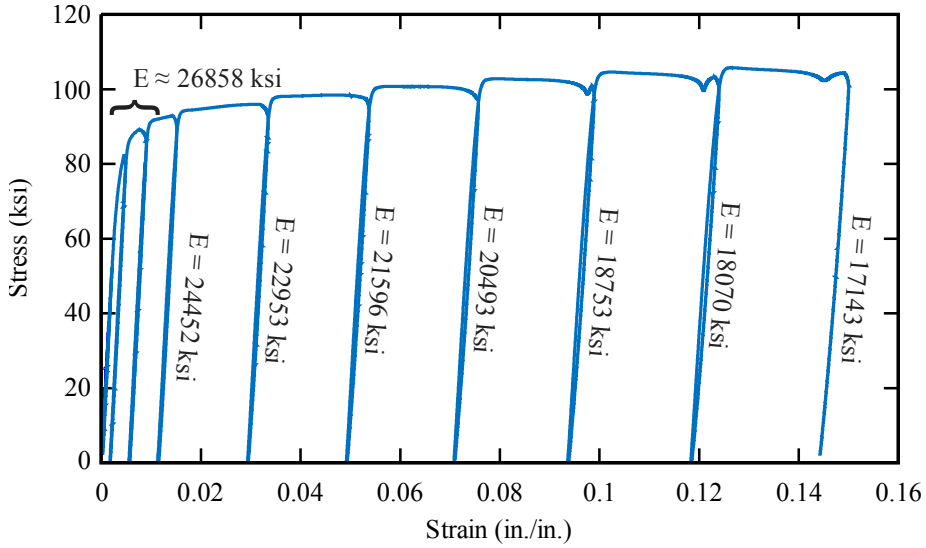

Figure 3.5. Evolution of elastic modulus with increasing strain

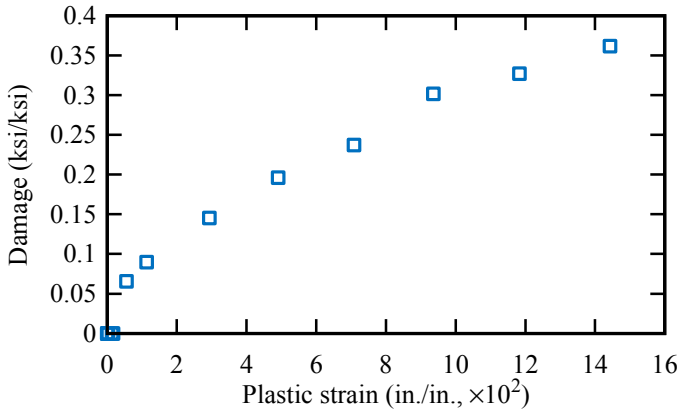

Figure 3.6. Evolution of time-independent plastic damage in the UNS S32101 stainless steel

3.2.2 Time-dependent plastic damage of UNS S32101 material

CDM-based models can combine damage occurring due to a variety of phenomena—e.g., creep, fatigue, plastic, etc. In this section, the feasibility of using CDM to model low

homologous temperature (LHT) stress relaxation in stainless steel is tested through an experimental approach. In particular, the experiments examine the feasibility of detecting macroscopic damage in a material that has undergone stress relaxation.

Two stress relaxation experiments using milled, dogbone specimens were conducted. One specimen was tested at a constant temperature of 70 °F, while the other was tested at a constant temperature of 100 °F. An MTS universal test machine was used to load the specimens and an extensometer having a 1 in. gage length was used to measure strain. Each specimen was loaded to an initial strain level of 0.0035 in./in. using a strain-controlled feedback loop at a rate of 0.015 in./in./min [ASTM E8 (2009)]. After being held under a constant deformation condition for 5 hours (i.e., the specimen was allowed relax for five hours), the specimen was unloaded using a load-controlled feedback loop at a rate of 83 lb/min [ASTM E8 (2009)]. The initial and final elastic modulus values were calculated in accordance with ASTM standard E111-04 (2010) and are shown in Fig. 3.7. No appreciable change in the modulus values (for either the 70 °F or 100 °F cases) is observed in either specimen after it underwent stress relaxation for a period of five hours. Hence, it may not be possible to use a macroscopic material property (e.g., the modulus of elasticity) to quantify the state of damage due to LHT stress relaxation in a specimen that has undergone stress relaxation for a short duration (e.g., 5 hours or less).

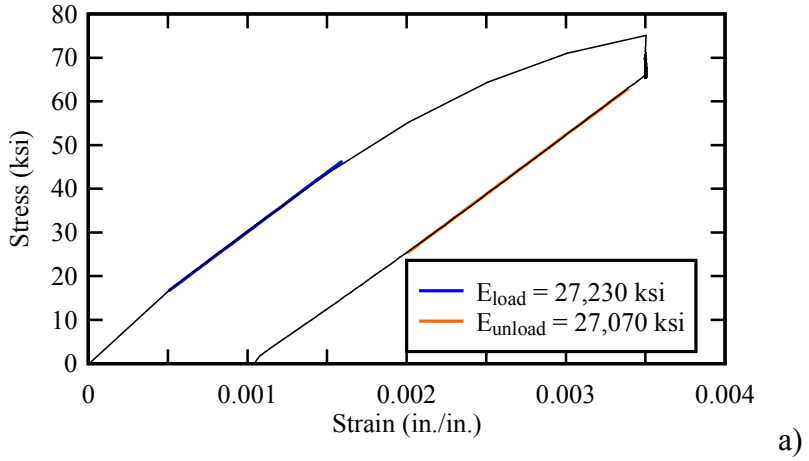

a)

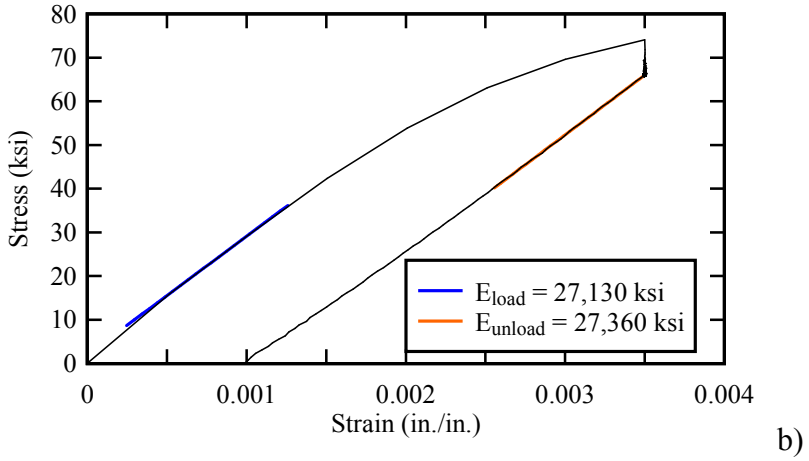

b)

Figure 3.7. Stress-strain relationships for stress relaxation experiments at: a) $\varepsilon_i = 0.0035$ in./in. at 70 °F; and b) $\varepsilon_i = 0.0035$ in./in. at 100 °F

3.2.3 Discussion

One of the goals of this research was to validate CDM-based stress relaxation models using direct experiments. However, the results of this section indicate that no appreciable macroscopic damage is observed in a specimen that has undergone low homologous temperature stress relaxation for a period of 5 hours or less. Hence, this study does not use CDM-based stress relaxation models to predict long-term stress relaxation in the UNS S32101 stainless steel.

Creep and stress relaxation in the LHT regime is exclusively limited to primary creep (Garofalo 1965). Since little or no macroscopic damage is observed in materials during primary creep (Lemaitre 1996), the damage evolution predicted by Eqns. (2.19) and (2.20) for the experiments conducted in this investigation cannot be verified independently.

The findings presented here do not imply that CDM is not a viable approach to characterize stress relaxation in the UNS S321010 stainless steel. The results merely demonstrate that at the temperature, strain levels and test durations studied here, no macroscopic damage is visible in the material; at higher temperatures, where macroscopically confirmable damage may become apparent, CDM-based models may prove to be useful.

3.3 Characterization of the microstructure

The microstructure of a material can have a marked effect its macroscopic behavior. For example, for duplex stainless steels the residual stress (microstress) is a function of the balance between the austenite and ferrite grains (Yang 2011). As has been mentioned before, the two sets of bars tested in this study (the first having diameters of 0.75 in. and the second having diameters of 1.25 in.) underwent different annealing conditions during manufacturing. These two sets of bars also have different Ramberg-Osgood parameters (Table 5.2) and their ultimate tensile stresses differ by about 9 percent (Table 5.1). Experiments to determine the volume fraction of the austenitic and ferritic grains in the two sets of bars are presented. Two techniques—one using a ferritescope and the other using metallography—are used.

3.3.1 Characterization of volume fractions using a ferritescope

A ferritescope—specifically, a Ferritescope model MP30 manufactured by Fischer—is a handheld device measures the ferrite content in duplex stainless steels. It works based on the principle of magnetic inductance (Beese and Mohr 2009). Specifically, the ferritic grains—which are magnetic—interact with a magnetic field generated by the ferritescope by inducing a voltage proportional to the ferritic content of the specimen. The ferritescope test is nondestructive and can be conducted rapidly. Two bars with 50 in. lengths (one 0.75 in. diameter bar and one 1.25 in. diameter bar) were tested. Measurements were made along the length in approximately 0.5 in. increments and four quadrants of each bar were tested.

The ferritescope outputs a ferrite number (FN), which can be related to the ferrite content using established relationships (Fig. 3.8). Additionally, corrections were made for the curvature of the bar (Fig. 3.9) using three-dimensional interpolation and calculated as:

$$Fe^{corr} = \alpha_{corr}^{convex\,curvature} \times Fe^{uncorr} \tag{3.10}$$

The ferrite content for each bar is presented in Figs. 3.10 and 3.11 for the 0.75 in. and 1.25 in. diameter bars, respectively. The 0.75 in. diameter bars have an average ferrite content of 59.9 %Fe; the 1.25 in. diameter bars have an average ferrite content of 55.7 %Fe.

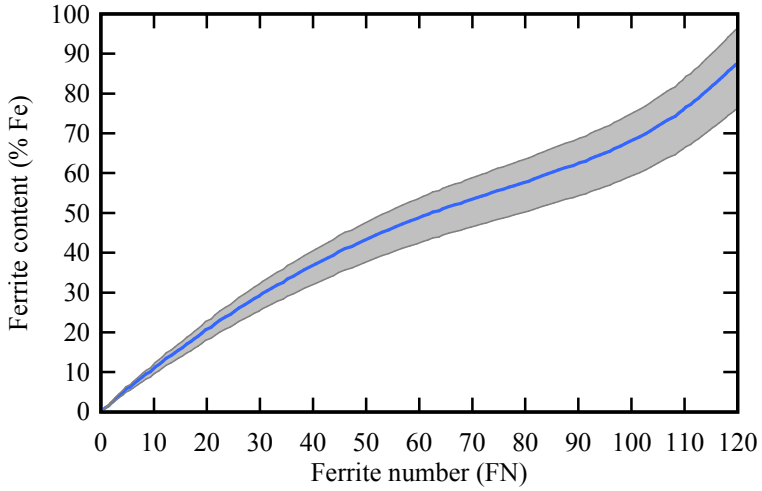

Figure 3.8. Conversion from ferrite number (FN) to ferrite content [after Fischer (2002)]

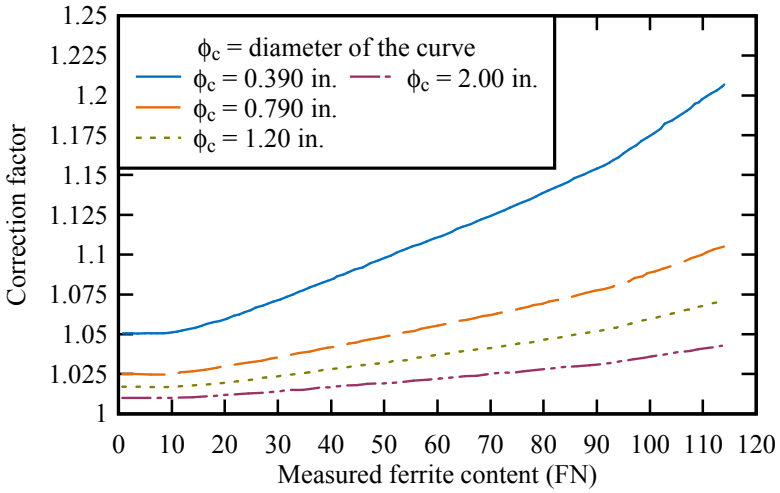

Figure 3.9. Correction factors for convexly curved specimens [after Fischer (2002)]

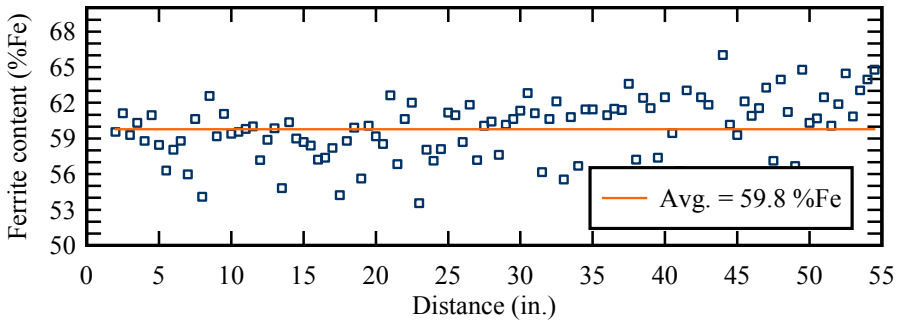

Q1)

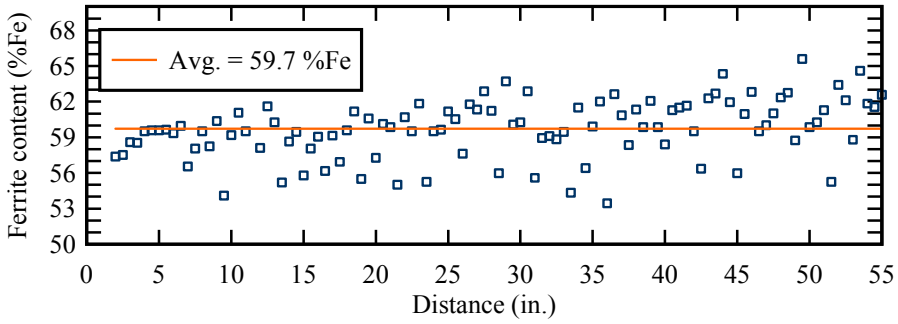

Q2)

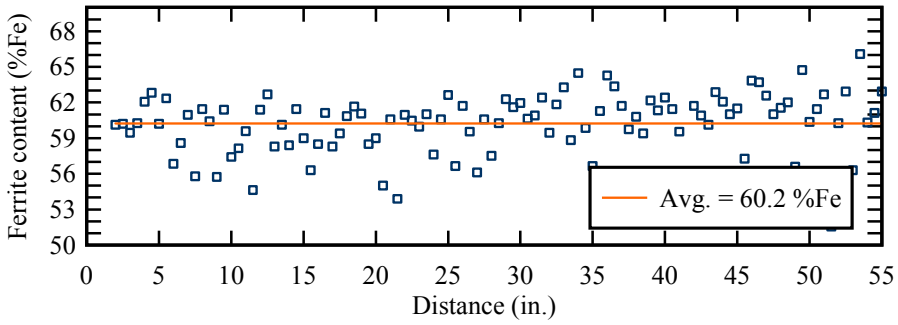

Q3)

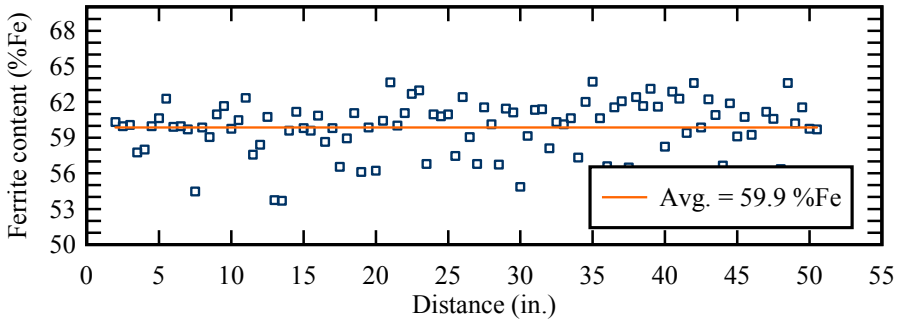

Q4)

Figure 3.10. Ferrite content for 0.75 in. diameter bar measured at the four quadrants

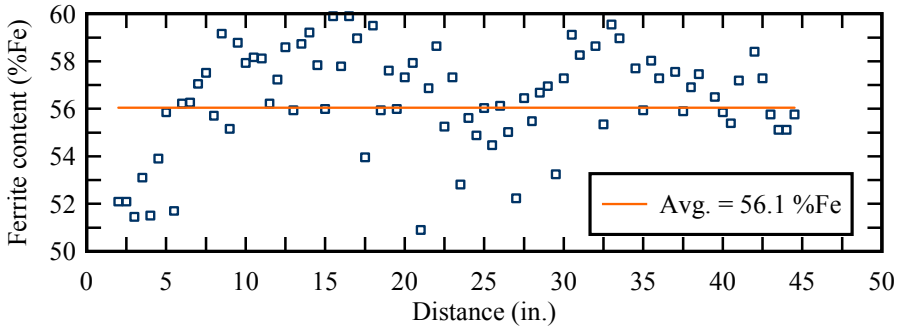

Q1)

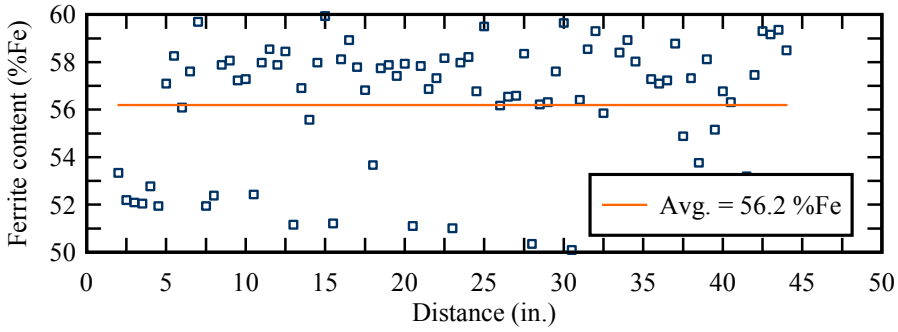

Q2)

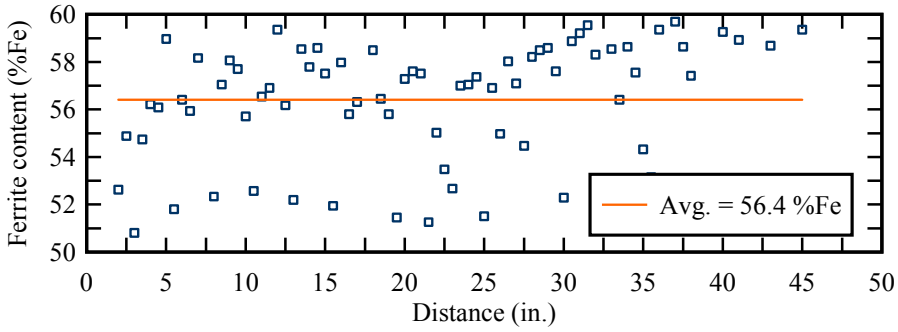

Q3)

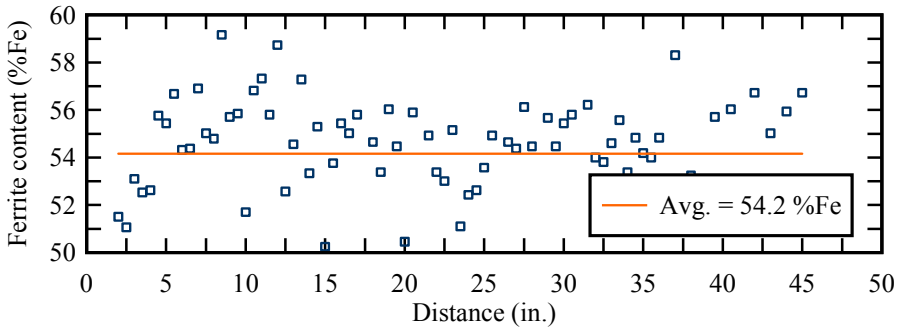

Q4)

Figure 3.11. Ferrite content for 1.25 in. diameter bar measured at the four quadrants

3.3.2 Characterization of volume fractions using metallography

Metallography deals with studying the constitution and underlying structure of metals (ASM 2004). The most common tool for metallography involves polishing and etching specimens and analyzing them using an optical microscope, with typical magnifications ranging from 50 to 1000×. The images generated using optical microscopy are evaluated using such techniques as image analysis and point counting (Underwood 1970). Here, the techniques used to prepare UNS S32101 specimens are discussed; the image analysis and point counting methods are also explained, and the results are presented. The metallography results are used to validate the data obtained using a ferritescope.

3.3.2.1 Sample preparation

Samples were cut from one randomly selected bar of each diameter set. From each diameter set, two samples—one corresponding to a longitudinal field of view and one corresponding to a transverse field of view—were cut (Fig. 3.12). The cut samples were then mounted in a phenolic power-based resin to afford easier handling.

Polishing a specimen for metallography involves sanding the surface with increasingly fine sandpaper. Specimens were polished on a wet sanding disk to maintain a low surface temperature; if the surface becomes hot during preparation, the material characteristics of the sample may change. Samples were first polished with 120 grit sandpaper, followed by 600, 1000, and 2000 grit sandpapers. The samples were then polished with a 6 μm sanding plate. Specimens were then polished using a 1 μm disk, and 0.25 μm disk. At the end of this process, the surface of the specimens has, to the naked eye, a mirror finish. After the specimens have been cleaned with acetone, they are etched.

A technique known as electrolytic etching was employed to reveal the austinic and ferritic phases of the material (Yang 2011). Specifically, specimens were etched with a 40% NaOH solution at 2.5 V for approximately 5 s. Austinic (γ) grains are light in color while ferritic (α) grains are dark (Fig. 3.13).

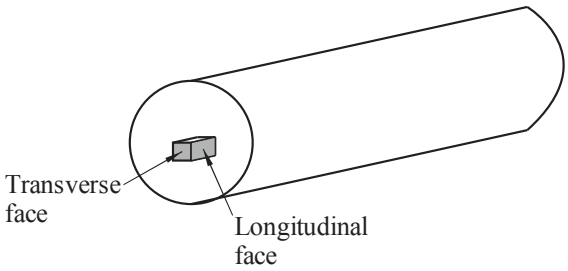

Figure 3.12. Longitudinal and transverse faces cut for metallography specimens

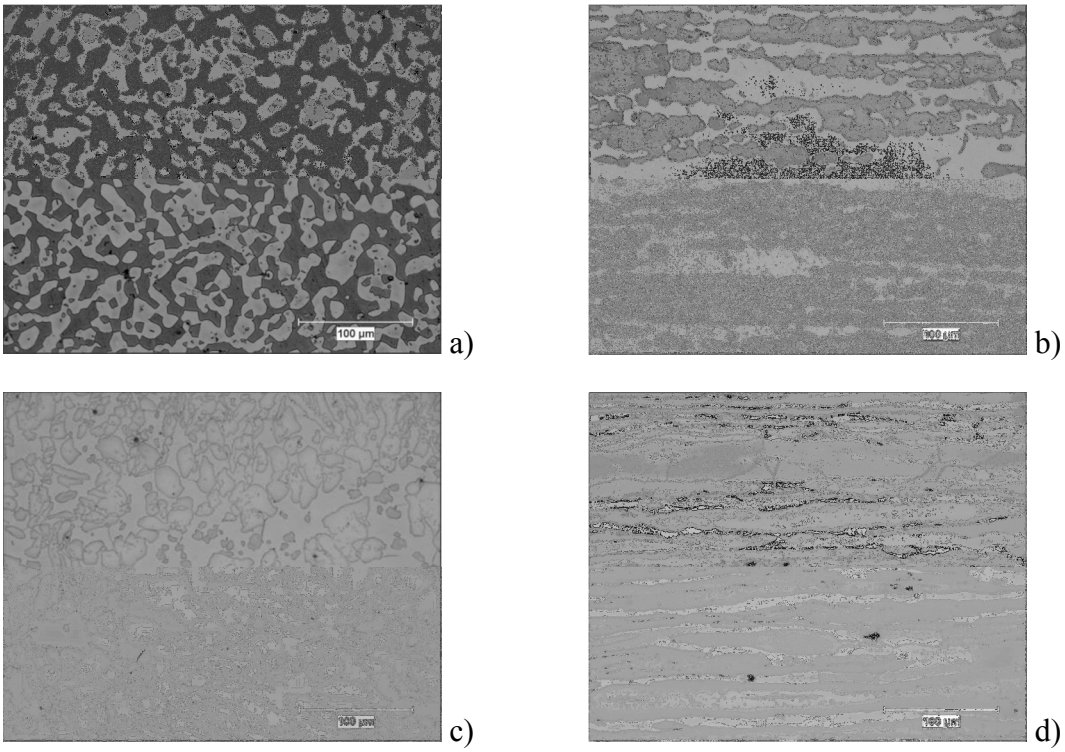

Figure 3.13. Micrographs of the UNS S32101 stainless steel. a) 0.75 in. bar, transverse face; b) 0.75 in. bar, longitudinal face; c) 1.25 in. bar, transverse face; d) 1.25 in. bar, longitudinal face

3.3.2.2 Image processing and quantitative stereology

A MATLAB algorithm was developed to quantify the results obtained from optical microscopy (Fig. 3.13). The algorithm converts the color image to a black-and-white (binary) image, where lighter (austenite) pixels are converted to white based on a threshold value. The darker (ferrite) pixels are converted to black. Since in binary images white pixels are assigned values of 1, the total number of pixels corresponding to the austenite phase can be obtained by summing all values of the image matrix:

$$A_{austenite} = \sum_{i=1}^{x_{\dim}} \sum_{j=1}^{y_{\dim}} IM_{i,j} \tag{3.11}$$

where [IM] is a matrix containing the pixel values for the image. Hence, the volume fraction of the austenite phase can be calculated as

$$V_{austenite} = \frac{A_{austenite}}{A_{total}} \tag{3.12}$$

And the volume fraction of the ferrite phase as, simply

$$V_{ferrite} = 1 - V_{austenite} \tag{3.13}$$

However, some micrographs were of poor quality and could not be analyzed using the image analysis algorithm. So a manual point-counting method proposed by Underwood (1970) was used for the images that could not be analyzed using the aforementioned algorithm. The point counting method (the simplest of the various quantitative stereology methods) involves charting a grid on the image and counting the intersecting points that lie over a light (or dark) phase (Fig. 3.14). If the lighter phase is used to count, the volume of austenite can be approximated as

$$V_{austenite} = \frac{\sum_i P_i^{austenite}}{P^{total}} \tag{3.14}$$

where $P_i^{austenite}$ is the total number of points intersecting over an austenitic grain in each grid (a total of five 5×5 grids were used for each micrograph); and P^{total} is the total number of points in the micrograph (i.e., 125 points). The volume of ferrite is computed using Eq. (3.13). The results of the metallography analysis are presented in Table 3.3.

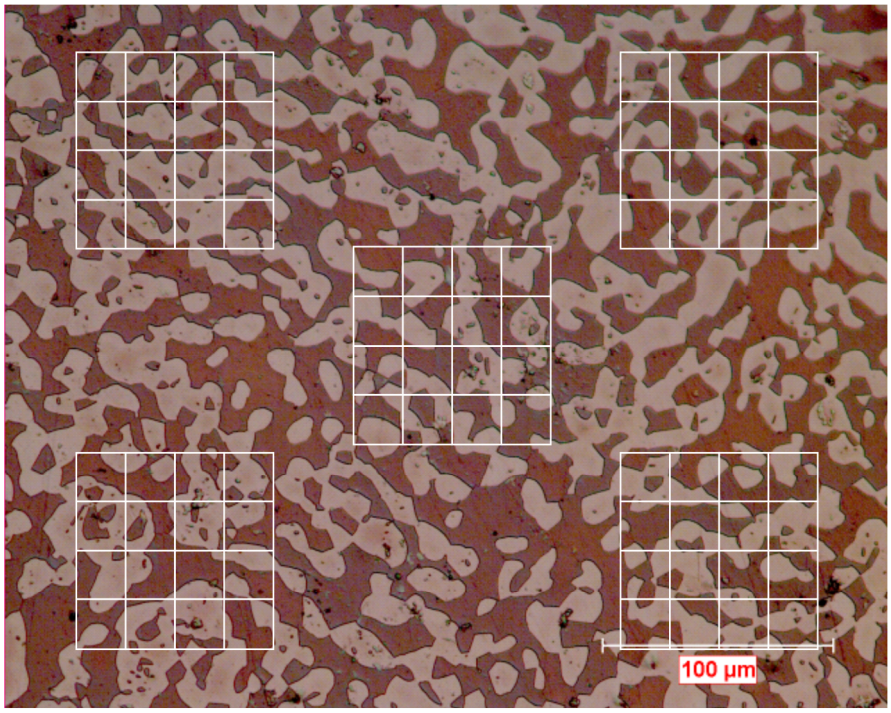

Figure 3.14. Grids over an optical microscope image of an etched UNS S32101 specimen

Table 3.3. Summary of metallography results

Diameter of rod (in.)	Direction	% Ferrite	% Austenite	Counting Method[a]
0.75	Transverse	52	48	I.A.
0.75	Longitudinal	54	46	P.C.
1.25	Transverse	50	50	P.C.
1.25	Longitudinal	53	47	P.C.

[a]I.A. denotes image analysis; P.C. denotes point counting

3.4 Summary

In this chapter, the basic material properties necessary to design stainless steel-based bridge pier cap strengthening systems were found through experimentation and analysis. Using results obtained from direct tension tests, a uniaxial constitutive relationship for the UNS S32101 stainless steel (in the Ramberg-Osgood form) was developed and recommended for use in design.

Experiments conducted to determine the evolution of damage in the material revealed that macroscopic damage is not apparent when the material is subjected to the temperature, initial strain conditions and test durations studied here. Hence, a CDM-based approach is not used in this investigation to characterize the long-term stress relaxation behavior of the UNS S32101 stainless steel. Still, a relationship established between plastic strain and damage due to time-independent plastic loading may prove useful for the design of future structural systems using the UNS S32101 alloy.

Finally, ferritescope analysis provided a glimpse into the microstructural composition of the material; especially, they provided information on how the bars belonging to the set with 0.75 in. bar diameters defer microstructurally from the bars belonging to the set with 1.25 in. diameters. Using a Ferritescope, we found that the 0.75 in. diameter bars have an average ferrite content of 59.9 %Fe; the 1.25 in. diameter bars have an average ferrite content of 55.7 %Fe. Conversely, metallography implies that both bars have approximately 50 %Fe. A potential explanation for this dichotomy between the two techniques is that the curve used to convert from the ferrite number to ferrite content (Fig. 3.8) has a potential error of approximately 10% from the mean in either direction.

Chapter 4

Stress relaxation of UNS S32101 stainless steel

This chapter examines the low homologous temperature (LHT) stress relaxation phenomenon of the UNS S32101 stainless steel. Particularly, short-term experiments (on the magnitude of hundreds of hours) are conducted and the data from those experiments are used to develop mechanics-based models to predict behavior to lifespans of interest. Small-scale experiments are also conducted to aid in the understanding of the temperature-dependent viscoelastic behavior of the duplex stainless steel material. These small-scale experiments are based on a modified temperature step-up experiment that is derived in this chapter.

4.1 Full-scale, ambient-temperature stress relaxation experiments

Owing to the UNS S32101 stainless steel's relatively recent vintage, a paucity of data exists concerning its long-term stress relaxation behavior. However—as has been demonstrated in previous chapters—the efficacy of the external strengthening system studied here is dependent on the minimum load in the pretensioned bars. Accordingly, a series of experiments are conducted to understand the stress relaxation behavior of the bars that will be used in conjunction with the strengthening system. These full-scale experiments use specifically designed and constructed test fixtures as well as new loading protocols to recreate the geometric, installation, and service conditions that are expected to exist on reinforced concrete bridge pier caps. An instrumentation plan consisting of load cells and strain gages is also described.

4.1.1 Description of apparatus and specimens

Four new experimental testing fixtures were designed and constructed to facilitate the measurement of stress relaxation in the UNS S32101 stainless steel at ambient temperature (AT) conditions. These specially-developed testing fixtures are composed of a steel channel apparatus bolted to hollow structural steel sections (Fig. 4.1a and 4.1b). The fixtures are intended to maintain a constant strain on stainless steel rods having approximate gauge lengths of 70 in. for extended periods of time while allowing for the placement of such instrumentation as strain gauges, extensometers, photographic strain measurements devices, and load cells. These testing frames consist of two channels at each end with hollow structural steel (HSS) sections that act as compression members between them. The channel apparatus involves two AISC C10×25 channels held together with the use of 1 in.-thick steel places welded to their top and bottom flanges. The HSS sections are 3 ft. long and represent the depth of a typical pier cap in the state of Georgia (Zureick et al. 2014). These channels are bolted together using the two 36 in.-long HSS5×5×5/16 steel members.

The specimens tested are intended to represent a typical stainless steel bar used with an external pretensioned structural strengthening system. The system involves using threaded bars coupled with nuts to maintain a constant strain condition. The bars used for the full-scale experiments have 100-in. lengths with 35 in. threading on one end and 3 in. of threading on the other (Fig. 4.2). A longer thread length on one side allows for the placement of a hydraulic jack and loading chair (Fig. 4.1c). The threads—16 threads/in. for the bars having 0.75 in. diameters and 12 threads/in. for the bars having 1.25 in. diameters—were machined in a fluid-cooled environment.

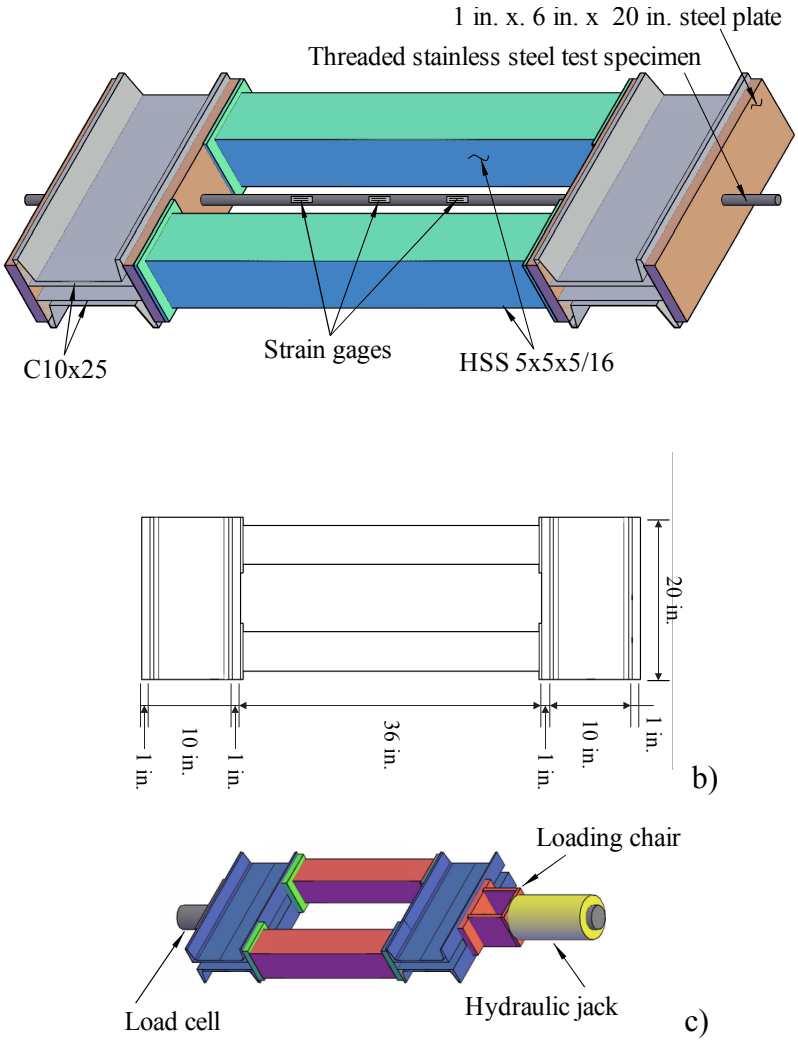

Figure 4.1. Schematic of experimental fixture: a) three-dimensional conceptual view; b) right-side view; c) reduced view showing hydraulic jack and load cell placement

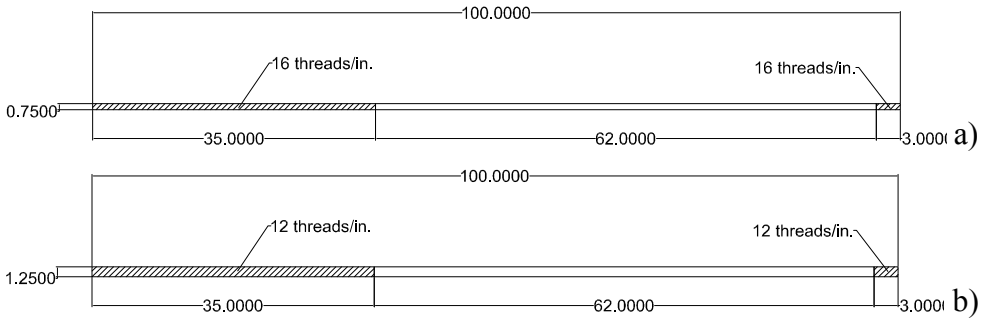

Figure 4.2. Threading details for: a) rod with diameter 0.75 in; b) rod with diameter 1.25 in.

4.1.2 Instrumentation plan

Preliminary tests demonstrated that the nut tightening process may cause vibrations in the rod. These vibrations, though not severe, may cause extensometers to become loose (and, hence, become unreliable sources for initial strain data). Instead, three epoxy-mounted strain gauges were used to monitor the strain in the rods during the initial loading phase. The load was monitored with the aid of a load cell. These sensors (Fig. 4.1c) allow for the accurate measurement of stresses and strains for the entire duration of each test.

4.1.2.1 Installation of strain gages

Strain gages having resistances of 350 Ω and gage lengths of 0.25 in. were used throughout the investigation. The strain gages are manufactured by Vishay Micro-Measurements and have model number CEA-06-250UW-350. The gages were bonded to the stainless steel test specimen using the Vishay M-bond AE-10 epoxy and post-cured at a temperature of 120 °F for a period of four hours.

4.1.2.2 Fabrication and calibration of load cells

Four load cells were developed for use in this study. The load cells are composed of round aluminum (alloy 6061) tubes with outer diameters of 3.5 in. and inner diameters of 2.5 in. The 6 in.-tall aluminum tubes were faced using a lathe to ensure the flatness of the top and bottom surfaces. Four strain gages were mounted at mid-height (Fig. 4.3a), bonded to each aluminum tube using the Vishay M-bond 600 epoxy, and post-cured at a temperature of 450 °F for a period of six hours. A full Wheatstone bridge circuit was completed by connecting the strain gages (Fig. 4.3b).

The four load cells were calibrated using a factory-manufactured Interface 200 kips load cell as well as a SATEC compression test frame. During calibration, the load cells

were loaded at a rate of approximately 0.1 kips/s and reached maximum loads of 120 kips (Fig. 4.4).

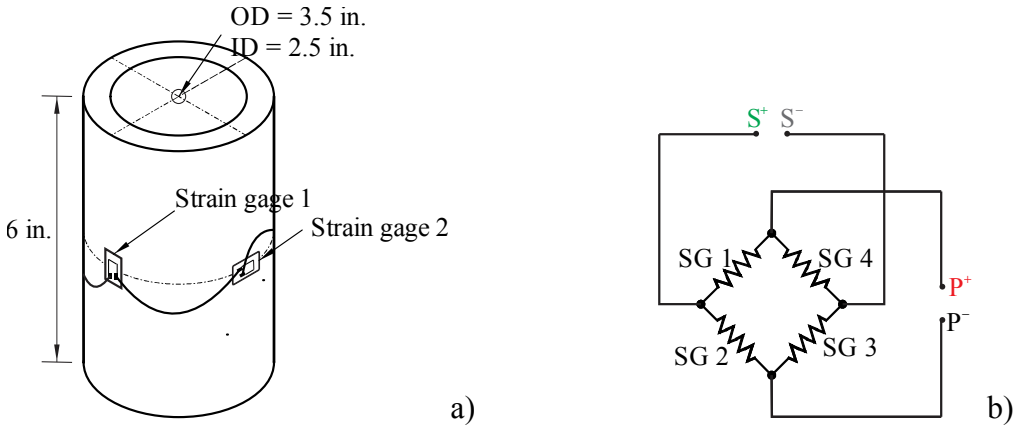

Figure 4.3. Schematic showing: a) a completed load cell; b) Wheatstone full bridge circuit for load cells

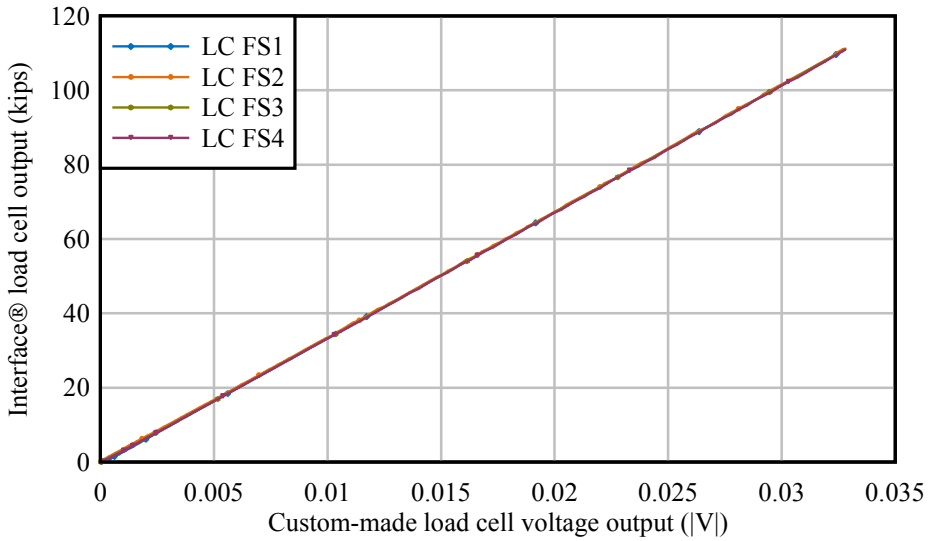

Figure 4.4. Calibration of custom-manufactured load cells with a factory-manufactured load cell

4.1.2.3 Measurement of data using computer data acquisition system

Data were recorded using a National Instruments computer data acquisition system (DAQ). During the first 48 hours of the test—the period where the stress relaxation rate, defined as the first derivative of stress with respect to time, is expected to be the

greatest—the load was sampled every 30 minutes; for the remainder of the test, data was recorded every hour. These sampling frequencies ensure that the load (and, hence, stress) is measured at a resolution appropriate for each stage of the test.

4.1.3 Environmental conditions

Twenty round UNS S32101 stainless steel specimens were tested at ambient conditions. Eleven specimens had cross-sectional diameters of 0.75 in. whereas the remaining nine had cross-sectional diameters equaling 1.25 in. The initial strain in the samples was induced using hydraulic jacks. Once the sample was tensioned to a predetermined initial stress, a nut placed at the edge of the gage length was tightened to maintain the initial strain. This is consistent with ASTM Standard E328-02 (2008), which permits the use of threading to hold strain constant for circular rods. With a constant strain, stress relaxation can be characterized by simply assessing the stress in the specimen over an extended period of time.

Throughout the duration of an experiment, temperature was maintained with the use of an environmental chamber at the Structural Engineering and Materials Research Laboratory of the Georgia Institute of Technology (or, GT Structures Lab). During the duration of testing, a constant ambient temperature condition—defined throughout this work as 70 °F ± 1 °F—was maintained.

4.1.4 Initial loading conditions

Stress relaxation experiments are deformation controlled. Indeed, initial strain in the unthreaded gauge section was used as the chief control variable for the experiments in this study. Nevertheless, safety concerns posed by higher stresses in the threaded area, where the cross-section is reduced, governed the design of the experiments. The 0.75 in. and 1.25 in. diameter rods have thread pitches of 16 threads/in. and 12 threads/in.,

respectively. At their narrowest points, these thread pitches reduce the cross-sectional area of the rods by, approximately, 20 and 16 percent for the 0.75 in. and 1.25 in. diameter rods, respectively. An additional safety margin is included by reducing the maximum permissible stress in the threaded region by 5 percent.

Hence, maximum strain levels corresponding to 76 percent of the ultimate tensile stress with respect to the nominal bar area for the 0.75 in. diameter rods and 70 percent of the ultimate stress for the 1.25 in. diameter rods (Fig. 4.5 and Table 4.1) are selected. Furthermore, a wide range of initial loading conditions were considered in this study. Multiple experiments at each initial stress level were conducted to validate the repeatability of results.

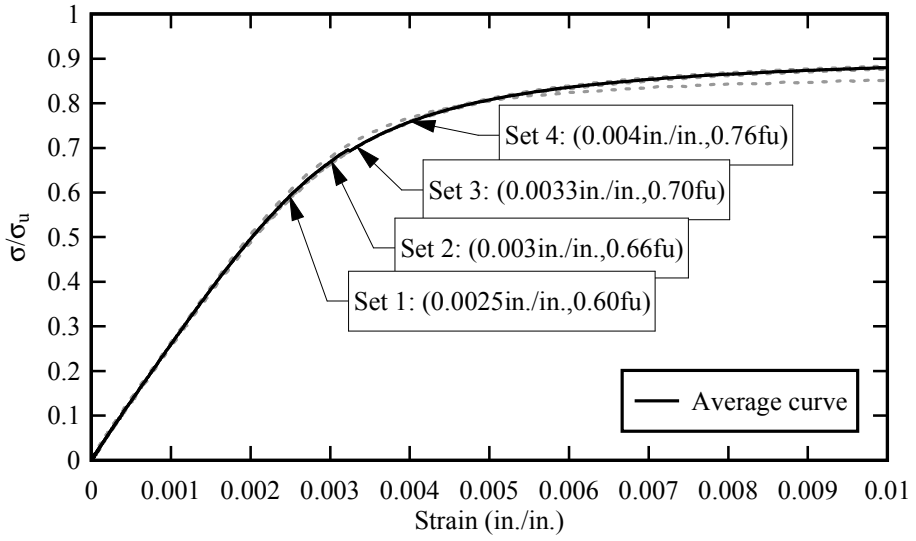

a)

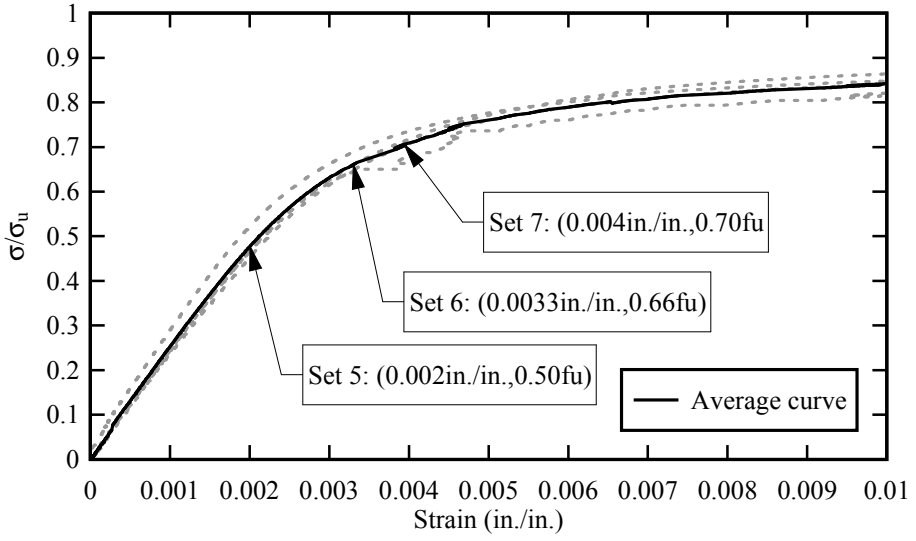

b)

Figure 4.5. Stress-strain curve showing experimental text matrix for: a) 0.75 in. diameter bars; b) 1.25 in. diameter bars

Table 4.1. Summary of experimental matrix

Test set	Cross-section diameter (in.)	Initial stress	No. specimens at AT	Test length (hours)
1	0.75	$0.60\sigma_u$	4	1,000
2	0.75	$0.66\sigma_u$	3	1,000
3	0.75	$0.70\sigma_u$	2	1,000
4	0.75	$0.76\sigma_u$	2	1,000
5	1.25	$0.50\sigma_u$	2	1,000
6	1.25	$0.66\sigma_u$	2	1,000
7	1.25	$0.70\sigma_u$	1	1,000
8	1.25	$0.50\sigma_u$	2/1	260
9	1.25	$0.66\sigma_u$	1	260
10	1.25	$0.70\sigma_u$	2	260

4.1.5 Ambient temperature experimental results

Data showing stress as a function of time are presented in Figs. 4.6 and 4.7 for the twenty experiments studied in this portion of the study. Stress relaxation is defined as a decrease in the load under constant strain conditions; accordingly, points corresponding to the initial loading portion of the curve are not shown. Stress is calculated using the nominal area of the bars. The specimens exhibit the two-region stress relaxation behavior associated with metals, where an initially rapid decrease in the stress (Region I) is followed by a gradual, asymptotic decline (Region II). Specimen IDs, nominal bar diameters, initial stresses (normalized by the ultimate tensile stress of the material), and percent relaxation at the end of the test are given in Table 4.2.

The data show that stress relaxation continues to occur past the 1,000 hour or 260 hour experimental durations, since the slope of the stress relaxation curve, $|\dot{\sigma}|$, is greater than zero at the termination of the experiments. Thus, an asymptotic limit cannot be ascertained simply from experimental data alone; a mechanics-based model is needed to extend the short-term experimental data to long-term service lifespans of interest.

Additionally, as shown in Fig. 4.8, stress relaxation for the UNS S32101 stainless steel at the ambient temperature condition (i.e., 70 °F or $T_H = 0.1773$) appears to be governed by logarithmic creep. Such behavior has been hypothesized for metals at low homologous temperatures by various previous studies (e.g., Marschall and Marringer 1976; Cotrell 1997; Nabarro 2001).

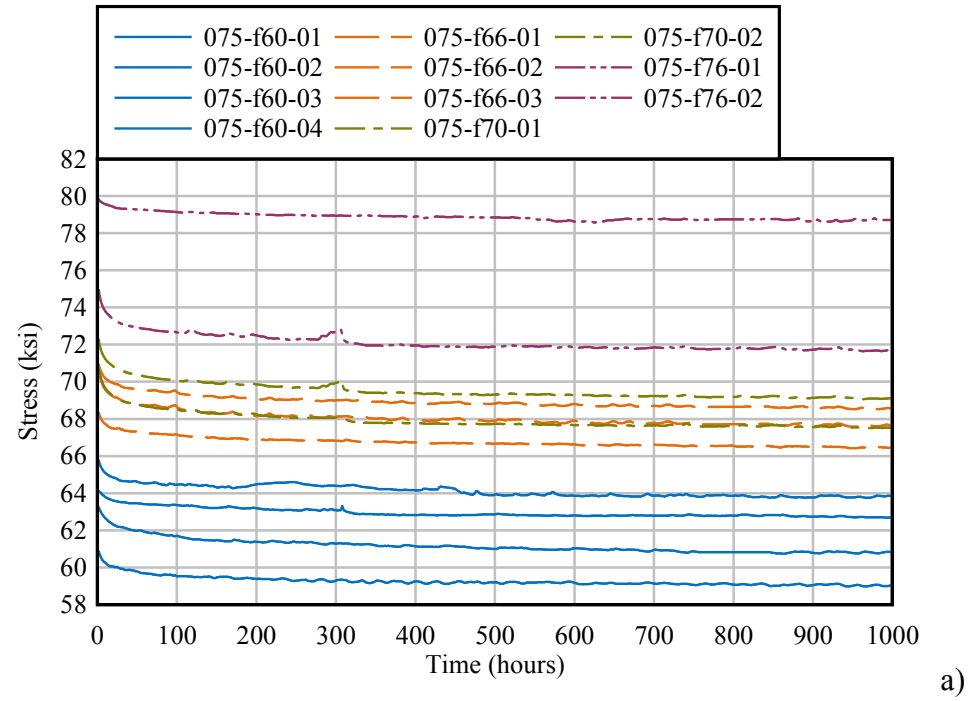

a)

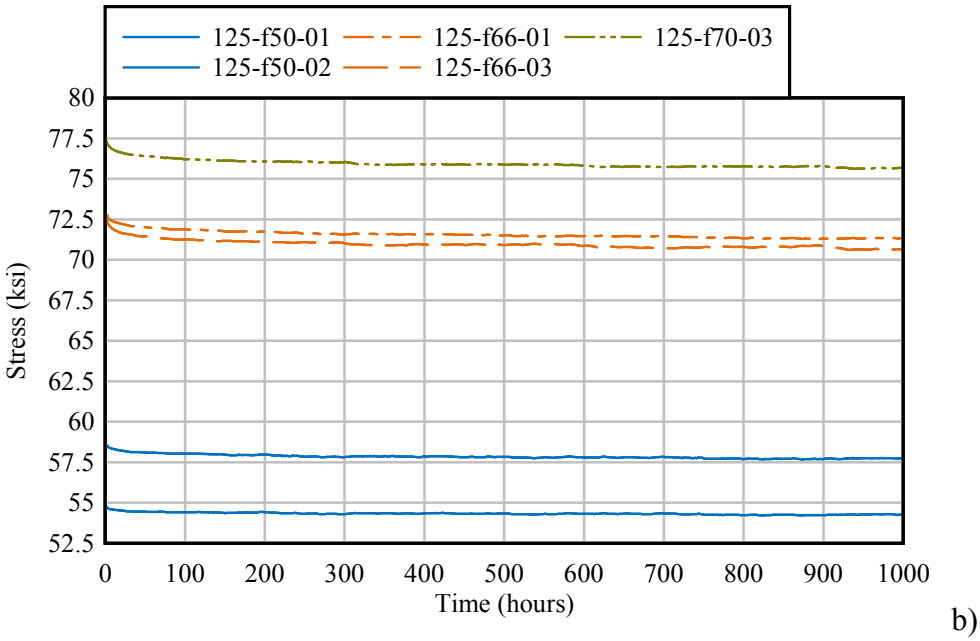

b)

Figure 4.6. Stress relaxation in the UNS S32101 stainless steel, 1,000 hr experiments: a) 0.75 in. diameter bars; b) 1.25 in. diameter bars

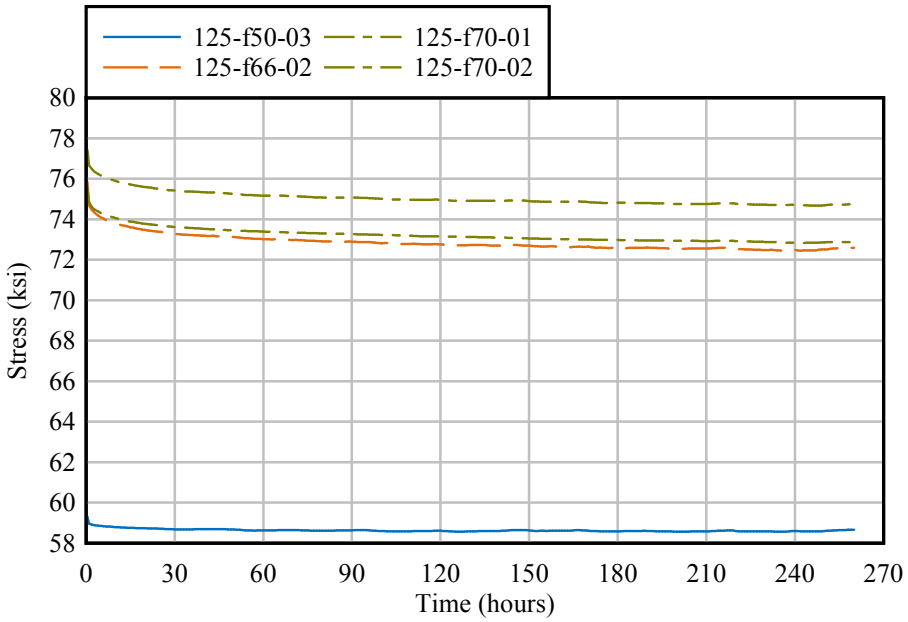

Figure 4.7. Stress relaxation in the UNS S32101 stainless steel, 260 hr experiments, 1.25 in. diameter bars

Table 4.2. Summary of experimental results

Specimen ID	Bar diameter (in.)	Test duration (hrs)	Normalized initial stress, σ/σ_u (ksi/ksi)	Percent relaxation at end of test (%)
075-f60-01	0.75	1,000	0.587	4.66
075-f60-02	0.75	1,000	0.610	5.62
075-f60-03	0.75	1,000	0.638	5.27
075-f60-04	0.75	1,000	0.612	2.92
075-f66-01	0.75	1,000	0.660	4.65
075-f66-02	0.75	1,000	0.688	6.89
075-f66-03	0.75	1,000	0.688	5.56
075-f70-01	0.75	1,000	0.698	8.34
075-f70-02	0.75	1,000	0.710	7.77
075-f76-01	0.75	1,000	0.760	2.00
075-f76-02	0.75	1,000	0.741	8.36
125-f50-01	1.25	1,000	0.478	1.93
125-f50-02	1.25	1,000	0.513	2.85
125-f50-03	1.25	260	0.515	1.70
125-f66-01	1.25	1,000	0.641	3.95
125-f66-02	1.25	260	0.665	5.79
125-f66-03	1.25	1,000	0.634	4.04
125-f70-01	1.25	260	0.681	4.48
125-f70-02	1.25	260	0.680	4.45

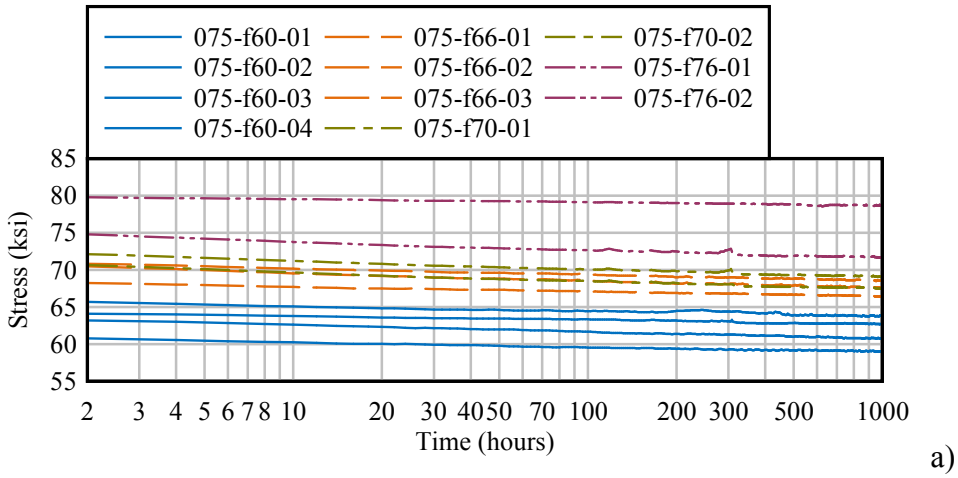

a)

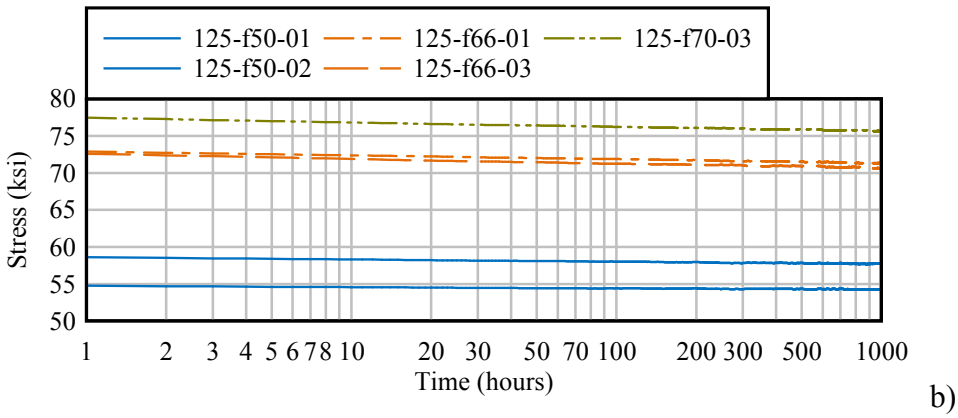

b)

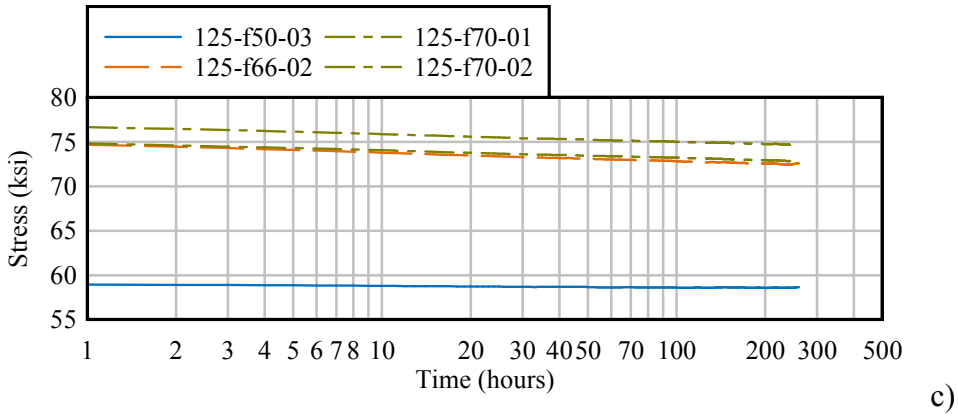

c)

Figure 4.8. Stress relaxation in the UNS S32101 stainless steel: a) 0.75 in. diam. bars; b) 1.25 in. diam. bars, duration 1,000 hrs.; b) 1.25 in. diam. bars, duration 250 hrs.

4.1.6 Development of suitable model to predict long-term behavior

4.1.6.1 Selection of model

Viscoelastic processes in metals can continue to occur over years and decades before reaching an asymptote. Yet, it is not feasible to conduct repeatable experiments—such as those conducted in the previous section—over such lengthy timescales. To overcome this limitation, models are typically developed from the (short-term) experimental data to allow for the prediction of the stress relaxation behavior to lifespans of interest. Justifiable extension of short-term experimental data to long timespans necessitates that the model describing the underlying phenomenological behavior be based on fundamental principles of mechanics. Furthermore, because this investigation's goal is to develop guidelines for the design of stainless steel-based structural strengthening systems, the model must be easily implementable into existing structural engineering design methodologies and philosophies.

The model proposed by Bažant and Yu (2013) is, thus, selected to predict the stress relaxation in UNS S32101 stainless steel. The Bažant-Yu model is based on viscoplasticity theory, has been proven to describe the time- and temperature-dependent behavior of carbon prestressing steel strands, and maintains a form that is similar to the equations currently in use by existing structural engineering design codes [e.g., American Concrete Institute, ACI, code 318-05 (2005) and Fédération Internationale de Béton, fib, code (2010)]. Adapted for the UNS S32101 stainless steel, the model for a uniaxially-loaded specimen under constant strain and ambient, isothermal temperature conditions has the following form:

$$\sigma = \min(\gamma\sigma_y, \sigma_0) + \sigma_y \left\langle \frac{\sigma_0}{\sigma_y} - \gamma \right\rangle \left[1 + \frac{\rho}{c} \left(\frac{t}{\lambda_{ss}} \right)^k \right]^{-c} \tag{4.1}$$

Here, σ_y is the 0.5% extension under load (EUL) stress; σ_0 the initial stress; γ, ρ, c, and k are temperature-dependent material constants; and λ_{ss} is taken to be 1,000 hrs for this study.

Temperature-dependence of a material is characterized through the use of the Arrhenius equation and the activation energy of flow, replacing the real time, t, in Eq. (2.9) with an effective time,

$$t = \int_{\tau'=0}^{\tau} A_T(\tau') d\tau' \tag{4.2}$$

where τ is the real time and A_T, the Arrhenius factor, is defined as

$$A_T(t) = \exp\left[\frac{Q}{k_B T_0} - \frac{Q}{k_B T(t)} \right] \tag{4.3}$$

Q is the activation energy of flow (in J/mol); k_B the Boltzmann constant (1.381×10^{-23} J/K); and T_0 the reference temperature (294.2 K in the present study).

4.1.6.2 Regression and statistical analysis of model

In this section, specimen-specific parameters are developed from the data presented in section 4.1.5 for the model selected in section 4.1.6.1. The least-squares approach is used to find the local-minimum of the sum of the squared-difference between the experimental results and the prediction obtained from the model at each time step. The parameters in the Bažant-Yu model—γ, ρ, c, k—are iteratively varied using a nonlinear generalized reduced gradient (GRG) algorithm in Microsoft Excel till a minimum of ℓ is achieved (Ladson et al. 1978). In other words,

$$\min \ell = \min \sum_{t=0}^{t=t_{duration}} \left[\sigma_t^{\exp} - \sigma_t^{\text{model}}(\gamma, \rho, c, k) \right]^2 \tag{4.4}$$

Yield stress values of 85.7 ksi for bars having 0.75 in. diameters and 88.3 ksi for bars having 1.25 in. diameters are used in Eq. (4.1). Parameter values resulting from the regression analysis for full-scale specimens tested at ambient temperature are presented in Table 4.3. Also presented in the same table are values of the coefficient of determination, R^2, between the experimental data and the corresponding Bažant-Yu model curve. Table 4.4 presents the prediction of percent stress relaxation at 1 year, 5 years, 10 years, 20 years, and 40 years.

Table 4.3. Summary of Bažant-Yu model regression analysis

Specimen ID	γ	ρ	c	k	R^2
075-f60-01	0.511	0.199	0.770	0.115	0.996
075-f60-02	0.502	0.225	0.577	0.168	0.982
075-f60-03	0.522	0.191	0.961	0.119	0.876
075-f60-04	0.574	0.171	0.442	0.216	0.980
075-f66-01	0.562	0.180	0.910	0.116	0.990
075-f66-02	0.524	0.237	0.683	0.118	0.972
075-f66-03	0.550	0.209	0.488	0.129	0.980
075-f70-01	0.475	0.342	0.237	0.131	0.964
075-f70-02	0.484	0.349	0.190	0.151	0.970
075-f76-01	0.545	0.060	0.145	0.185	0.955
075-f76-02	0.516	0.263	0.576	0.100	0.945
125-f50-01	0.528	0.268	0.104	0.122	0.887
125-f50-02	0.521	0.270	0.111	0.150	0.958
125-f50-03	0.555	0.243	0.091	0.104	0.916
125-f66-01	0.553	0.234	0.106	0.153	0.988
125-f66-02	0.486	0.311	0.144	0.162	0.992
125-f66-03	0.613	0.275	0.161	0.160	0.947
125-f70-01	0.511	0.388	0.076	0.240	0.996
125-f70-02	0.602	0.378	0.133	0.201	0.992

The results show that—with the exception of the 075-f76-01 specimen—a positive correlation exists between the initial stress and the long-term stress relaxation in the UNS S32101 material (Fig. 4.9). Unified models are developed for percent stress relaxation for simplified design recommendations for various timescales and for different initial stresses

that provide an upper-bound of the stress relaxation values while being compatible with existing structural design methodologies.

Table 4.4. Summary of Bažant-Yu model stress relaxation predictions

Specimen ID	Normalized initial stress, σ/σ_u (ksi/ksi)	Percent relaxation (%)				
		1 yr	5 yrs	10 yrs	20 yrs	40 yrs
075-f60-01	0.587	5.81	6.69	7.09	7.51	7.95
075-f60-02	0.610	7.53	9.05	9.75	10.5	11.2
075-f60-03	0.638	6.64	7.71	8.21	8.73	9.27
075-f60-04	0.612	4.58	5.80	6.37	6.96	7.58
075-f66-01	0.660	5.76	6.67	7.10	7.54	8.00
075-f66-02	0.688	8.54	9.78	10.4	10.9	11.5
075-f66-03	0.688	6.91	7.99	8.49	9.00	9.52
075-f70-01	0.698	10.0	11.2	11.7	12.2	12.7
075-f70-02	0.710	9.56	10.7	11.4	11.8	12.3
075-f76-01	0.760	2.82	3.52	3.85	4.20	4.57
075-f76-02	0.741	9.92	11.1	11.6	12.1	12.7
125-f50-01	0.478	2.24	2.45	2.55	2.64	2.74
125-f50-02	0.513	3.41	3.81	3.98	4.16	4.34
125-f50-03	0.515	2.23	2.42	2.50	2.58	2.66
125-f66-01	0.641	4.74	5.33	5.59	5.85	6.12
125-f66-02	0.665	8.10	9.14	9.60	10.1	10.5
125-f66-03	0.634	4.72	5.36	5.65	5.93	6.22
125-f70-01	0.681	6.76	7.71	8.12	8.53	8.94
125-f70-02	0.680	6.53	7.45	7.84	8.24	8.64

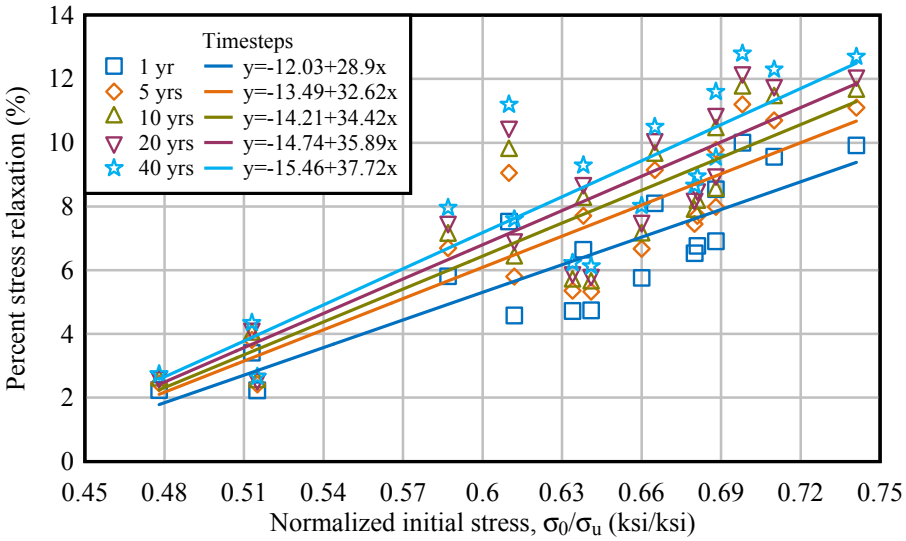

Figure 4.9. Percent stress relaxation for various initial stresses

Dispersion in the data is characterized by statistical analysis. Since there is a correlation between initial stress and percent relaxation at each time step, data are first

normalized to single initial stress values (i.e., $\sigma_0 / \sigma_u = 0.50, 0.60, 0.70, \text{and } 0.75$) by using the slope of the linear regression curve obtained show in Fig. 4.9. Mathematically, this normalization procedure is given by

$$p_{sr}^{norm} = m_{timestep}\left(\sigma_n^{norm} - \sigma_n^{init}\right) + p_{sr}^{init} \tag{4.5}$$

where $m_{timestep}$ is the slope of the regression curve given in Fig. 4.10 (13.0 for the 2 hours timestep; 15.5 for 10 hours; 18.3 for 50 hours; 19.6 for 100 hours; 22.7 for 500 hours; 24.2 for 1,000 hours; 27.7 for 5,000 hours; 28.9 for 1 year; 32.6 for 5 years; 34.4 for 10 years; 35.9 for 20 years; and 37.7 for 40 years); σ_n^{norm} is the initial stress normalized for $\sigma_i / \sigma_u = 0.50, 0.60, 0.70, \text{and } 0.75$; σ_n^{init} is the original value of the stress; and p_{sr}^{init} and p_{sr}^{norm} are original and normalized percent stress relaxation values, respectively. Fig. 4.10 shows the results of the normalization procedure, with the new normalized stresses on the abscissa and the associated percent stress relaxation values on the ordinate.

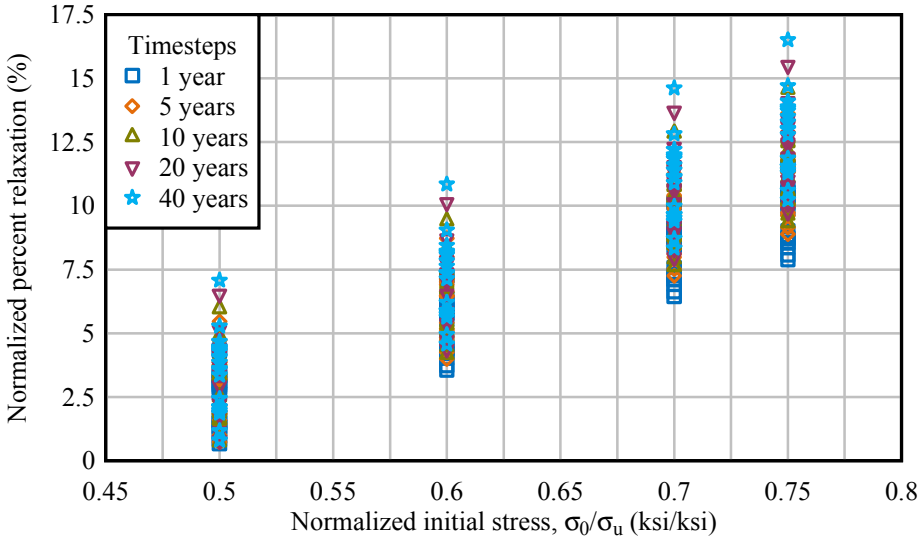

Figure 4.10. Normalized percent stress relaxation against normalized initial stress

Probability papers are then developed to select appropriate probabilistic distributions for the data presented in Fig. 4.10 at each initial stress level for the various time steps. The two-parameter Weibull distribution is selected. The Weibull distribution has been suggested as an appropriate probability distribution for various damage-driven processes like fatigue (Freudenthal 1960), and creep and creep-rupture (e.g., Christensen 2004 and Kim et al. 2010). The two-parameter Weibull distribution has been used in structural engineering applications to describe various material properties (Ellingwood 2003). For most material properties—like strength and stiffness—the 5th-percentile characteristic value is used (Zureick et al. 2006); for these properties are conservative when they have a lower-bound value. In contrast, higher stress relaxation values are conservative for design applications. Accordingly, the 95th-percentile characteristic, upper-bound values of the percent relaxation at the various different time steps in Fig. 4.10 are used.

Characteristic values can be used as nominal design values. A detailed procedure for calculating the 95th-percentile characteristic value is given in Zureick et al. (2006). But the first step in the process is calculating the Weibull shape parameter, β, and the Weibull scale parameter, α. These parameters are then used to compute the nominal value of the sample data for the pth fractile of the distribution. In other words, this is the value for which $P\left[X < x_p\right] = p$ and is computed by (Zureick et al. 2006)

$$x_p = \alpha\left[-\ln\left(1-p\right)\right]^{1/\beta} \tag{4.6}$$

Hence, the 95th-percentile characteristic value is given by

$$x_{0.95} = \alpha\left[3.00\right]^{1/\beta} \tag{4.7}$$

Table 4.5 and Fig. 4.11 show the 95th-percentile characteristic values of percent stress relaxation for $\sigma_0 / \sigma_u = 0.50, 0.60, 0.70, \text{and } 0.75$. These 95th-percentile characteristic values of percent stress relaxation at different times steps are subsequently used to develop Bažant-Yu model parameters for unified stress relaxation curves (Table 4.6, Fig. 4.12). Figs. 4.11 and 4.12 represent upper-bound stress-relaxation values that can be used to design stainless steel-based pretensioned strengthening systems.

Table 4.5. 95th-percentile characteristic values of percent stress relaxation

Normalized initial stress, σ/σ_u (ksi/ksi)	Percent relaxation (%)				
	1 yr	5 yrs	10 yrs	20 yrs	40 yrs
0.50	4.40	5.06	5.37	5.74	6.10
0.60	7.10	8.15	8.65	9.18	9.72
0.70	9.56	11.4	12.1	12.8	13.5
0.75	11.4	13.0	13.8	14.6	15.4

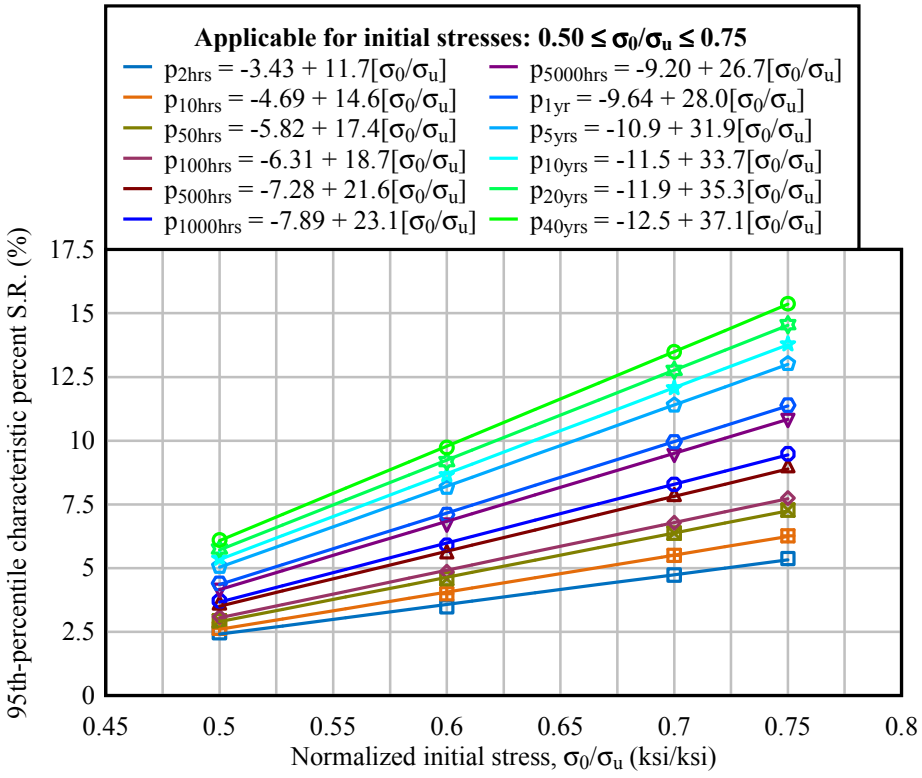

Figure 4.11. Normalized percent stress relaxation

Table 4.6. Summary of Bažant-Yu model regression analysis for 95th-percentile characteristic values

		Bažant-Yu model parameters				
	Normalized initial stress, σ/σ_u (ksi/ksi)	γ	ρ	c	k	σ_v (ksi)
Bar diam. = 0.75 in.	0.50	0.465	0.185	0.917	0.104	85.8
	0.60	0.465	0.185	0.917	0.104	85.8
	0.70	0.460	0.292	0.347	0.132	85.8
	0.75	0.461	0.292	0.348	0.132	85.8
Bar diam. = 1.25 in.	0.50	0.491	0.185	0.917	0.104	88.3
	0.60	0.491	0.185	0.918	0.104	88.3
	0.70	0.489	0.274	0.316	0.132	88.3
	0.75	0.489	0.287	0.356	0.131	88.3

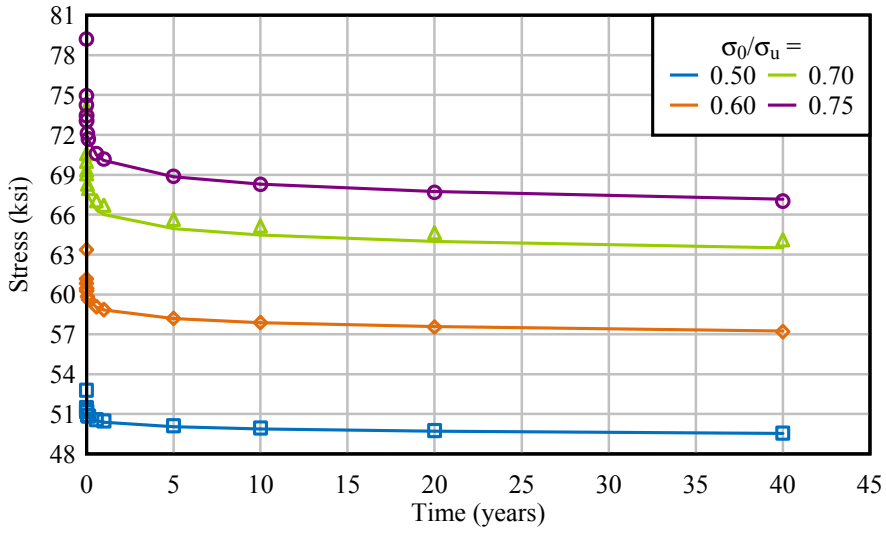

a)

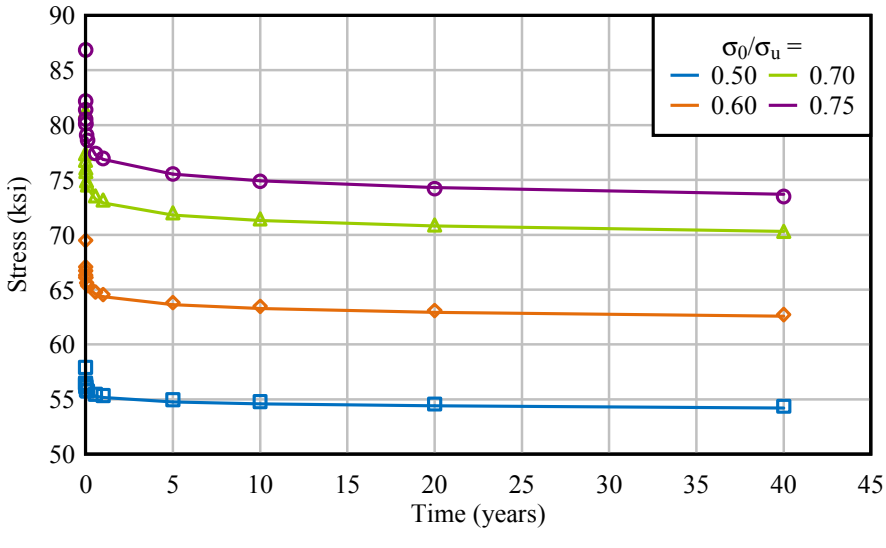

b)

Figure 4.12. 95th-percentile characteristic stress relaxation curves for bars with diameters: a) 0.75 in.; b) 1.25 in.

The equations and parameters presented in Figs. 4.11 and 4.12 and Tables 4.5 and 4.6 provide a conservative basis for calculating stress relaxation in the UNS S32101 stainless steel for individual initial stress levels. A unified viscoplasticity model that is applicable and conservative over the entire loading range would simplify the design process. The following two equations—corresponding to the $\sigma_0 / \sigma_u = 0.70$ loading level for the 0.75 in. diameter bars and $\sigma_0 / \sigma_u = 0.75$ for the 1.25 in. diameter bars—are valid for $\sigma_0 / \sigma_u \le 0.75$:

$$\sigma_{0.75} = \min(0.460\sigma_y, \sigma_0) + \sigma_y \left\langle \frac{\sigma_0}{\sigma_y} - 0.460 \right\rangle \left[1 + \frac{0.292}{0.347} \left(\frac{t}{1{,}000\,\text{hr}} \right)^{0.132} \right]^{-0.347} \tag{4.8}$$

$$\sigma_{1.25} = \min(0.489\sigma_y, \sigma_0) + \sigma_y \left\langle \frac{\sigma_0}{\sigma_y} - 0.489 \right\rangle \left[1 + \frac{0.287}{0.356} \left(\frac{t}{1{,}000\,\text{hr}} \right)^{0.131} \right]^{-0.356} \tag{4.9}$$

Though Eq. (4.8) may be overly conservative for bars having 1.25 in. diameters, it conservatively predicts the long-term stress relaxation for both of the two geometries of UNS S32101 duplex stainless steel bars tested in this investigation.

4.2 Experimental determination of the γ parameter in the viscoplastic constitutive model

Among the four parameters in the Bažant-Yu viscoplastic constitutive model—γ, ρ, c, k—the γ parameter has the greatest physical meaning. For $\gamma\sigma_y$ is a temperature-dependent material constant that has two implications: 1) it is the limit of the stress relaxation curve for $t \to \infty$ (i.e., $\sigma \to \gamma\sigma_y$ for $t \to \infty$); 2) it is the maximum initial stress below which no stress relaxation will occur (i.e., no stress relaxation will occur for $\sigma_0 < \gamma\sigma_y$). In this section, the second definition is exploited to develop an experiment

that directly, albeit qualitatively, validates the values of γ found in the preceding section via regression analysis.

For carbon prestressing steel strands, γ is approximately 55 percent of the yield stress. Similar values are obtained through regression analysis for the UNS S32101 stainless steel material investigated here (Table 4.3). Experimental confirmation of the value for γ obtained through regression analysis would serve to further validate the applicability of Bažant-Yu viscoplastic constitutive model for stainless steel. An experiment—based on the hypothesis that no stress relaxation will occur for specimens loaded to initial stresses lower than $\gamma\sigma_y$ —is developed.

In this experiment, specimens are initially loaded to low stresses. Nuts are used to maintain a constant strain condition in the specimens for a period of at least 30 hours and load is monitored throughout the duration using a load cell. If no appreciable decrease in the load is observed over 30 hours, the load is again increased (or stepped-up).

Three UNS S32101 specimens (two with 0.75-in. diameters and one with 1.25-in. diameter) were tested using the stress step-up experiment. Stress (normalized by yield stress) of a function of time is given in Fig. 4.13. The experimental results show, independently, that $0.50 \le \gamma \le 0.55$, in good agreement with the values of γ obtained through regression analysis. For comparison, the values for γ previously obtained from regression analysis range from 0.475 to 0.613, as summarized in Table 4.3.

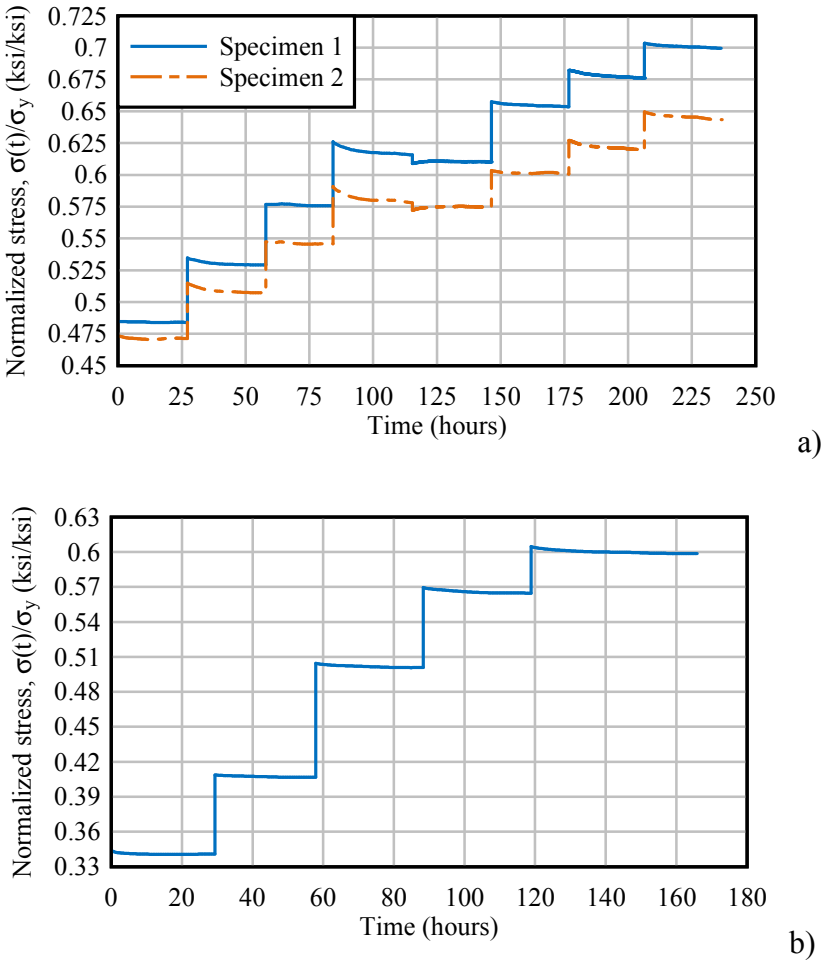

Figure 4.13. Experimental determination of γ parameter for bar diameter: a) 0.75 in.; b) 1.25 in.

4.3 Experiments to determine the activation energy for stress relaxation

Creep and stress relaxation at low temperatures are driven by a thermally activated process and can be modeled using an Arrhenius-type equation (Marschall and Maringer 1977; Conrad 1964; Neu and Sehitoglu 1992). For an Arrhenius-type model, the activation energy, Q, becomes an important parameter when one is concerned with describing the temperature-dependent behavior of stress relaxation (Cotrell 1964). As an example, Eq. (4.3) relies primarily on the activation energy for stress relaxation to characterize temperature dependence. In this section, two approaches to experimentally

determine the activation energy associated with stress relaxation at low homologous temperatures are explored.

The first approach—presented by Bažant and Yu 2013—involves comparing stress relaxation data from specimens loaded to the same initial strain, but tested at different constant temperatures. However, as stated in section 2.4.6, the Bažant and Yu approach has several drawbacks. Specifically, it requires longer-term experiments (e.g., 1,000 hours) that must be conducted at the same initial stresses for varying temperatures, limiting the repeatability of experiments if the availability of test specimens is a concern.

Thus, an alternate approach is explored, one based on the temperature step-up method proposed for creep by Conrad (1964) and Garofalo (1965). Such an approach has previously been employed to determine the activation energy for creep from a creep experiment. It involves loading a specimen to an initial stress at a constant temperature and then abruptly increasing the temperature. The resulting change in the slope of the time-stress curve offers a way to calculate the activation energy associated with stress relaxation. In this section, the approach is developed from a theoretical perspective and experiments are conducted to determine the activation energy for the UNS S32101 stainless steel.

4.3.1 Temperature step-up test for stress relaxation

4.3.1.1 Formulation for creep test

Various investigations [e.g., Neu and Sehitoglu (1992) and Conrad (1964)] have used temperature step-up tests to determine the apparent activation energy associated with creep. The basic premise involves loading the specimen to a constant load at a constant initial temperature and then increasing the temperature of the system at arbitrary time steps (Fig. 4.14). The apparent activation energy can then be determined from the change

in creep strain rate that occurs at the instant of the temperature change. Mathematically, the activation energy, Q, is computed using data from a temperature step-up test with the following equation (Conrad 1964):

$$Q = -R\left[\frac{\partial(\ln \dot{\varepsilon}^{cr})}{\partial(1/\mathrm{T})}\right] = \frac{R\ln(\dot{\varepsilon}_2^{cr} / \dot{\varepsilon}_1^{cr})}{[1/T_1] - [1/(T_1 + \Delta T)]} \tag{4.10}$$

where $\dot{\varepsilon}_1^{cr}$ and $\dot{\varepsilon}_2^{cr}$ are, respectively, the creep strain rates immediately prior to and following the abrupt temperature change; T_1 the temperature before the abrupt change; ΔT the temperature change (positive or negative); and R the gas constant, defined as the Boltzmann constant, k_B, multiplied by the Avogadro constant. Temperatures are in the units of Kelvin.

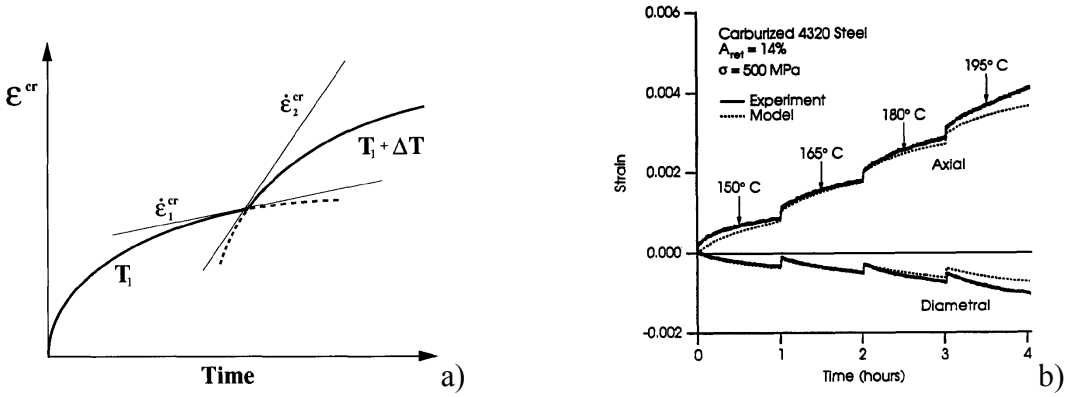

Figure 4.14. Differential temperature creep test: a) showing strain rates; b) empirical temperature step-up test [from Neu and Sehitoglu (1992)]

4.3.1.2 Formulation for stress relaxation test

While Conrad (1964), Garafalo (1965), and Neu and Sehitoglu (1992) have shown that it is possible to determine the apparent activation energy from creep tests with temperature steps (positive or negative), their approach requires experimental information about two variables: temperature and creep strain (or creep strain rate). It is not possible to directly measure the creep strain in a stress relaxation experiment; in a stress relaxation

experiment, it is easiest to measure the load (or, hence, stress) or the total strain. In this section, a new approach is derived—built on the previous work by Conrad (1964), Garafalo (1965), and Neu and Sehitoglu (1992)—that relates activation energy to the stress rate in a stress relaxation experiment.

As noted in Chapter 2, as the stress supported by a specimen relaxes, so, too, does the elastic strain. In other words (Garafalo 1965; Oding et al. 1965; Marschall and Maringer 1977):

$$\frac{d\sigma}{dt} = E\frac{d\varepsilon^e}{dt} \tag{4.11}$$

where E is the elastic modulus, ε^e the elastic strain, and σ the stress in the specimen. While Eq. (4.11) relates the stress to the elastic strain, Eq. (4.10) requires information about the creep strain. To relate the stress to the creep strain, we introduce the fundamental premise of the stress relaxation experiment, i.e., that the total strain, ε^t, in the specimen remains constant (Oding et al. 1965; Rabotnov 1969). Thus,

$$\varepsilon^t = \varepsilon^e + \varepsilon^{cr} = \text{constant} \tag{4.12}$$

Differentiating the equation with respect to time gives

$$\frac{d}{dt}\varepsilon^e + \frac{d}{dt}\varepsilon^{cr} = 0 \tag{4.13}$$

Hence, the elastic strain rate is related to the creep strain rate as simply

$$\frac{d}{dt}\varepsilon^e = -\frac{d}{dt}\varepsilon^{cr} \tag{4.14}$$

Now, using Eq. (4.11), we relate the creep strain rate to the stress in the specimen. Note that in the following equation, only one experimentally measured quantity (load as a function of time) is required as an input.

$$\frac{d\varepsilon^{cr}}{dt} = \dot{\varepsilon}^{cr} = -\frac{1}{E}\frac{d\sigma}{dt} = -\frac{1}{E}\dot{\sigma} \tag{4.15}$$

Substituting Eq. (4.15) into Eq. (4.10), we can relate the activation energy to the stress rate, $\dot{\sigma}$, immediately prior to and following an abrupt temperature change during a stress relaxation experiment (i.e., $\dot{\sigma}_1$ and $\dot{\sigma}_2$):

$$Q = \frac{R\ln(E_1\dot{\sigma}_2 / E_2\dot{\sigma}_1)}{[1/T_1] - [1/(T_1 + \Delta T)]} \tag{4.16}$$

Here, E_1 and E_2 are the elastic moduli at the initial and final temperatures corresponding to each temperature jump. Additionally, the temperatures are in the units of Kelvin.

Hence, experiments can be conducted where the specimen is loaded to a particular initial stress at a lower temperature (for instance, 70 °F) and the temperature is then abruptly changed (Fig. 4.15). Having knowledge only of the load and temperature as a function of time, one could determine the activation energy at several different temperatures with the same specimen. Because only one specimen is used to obtain information about the apparent activation energy at various temperatures, experiments could be easily repeated for several initial strains with a limited number of specimens. An additional benefit of this approach is that it allows for shorter-duration experiments.

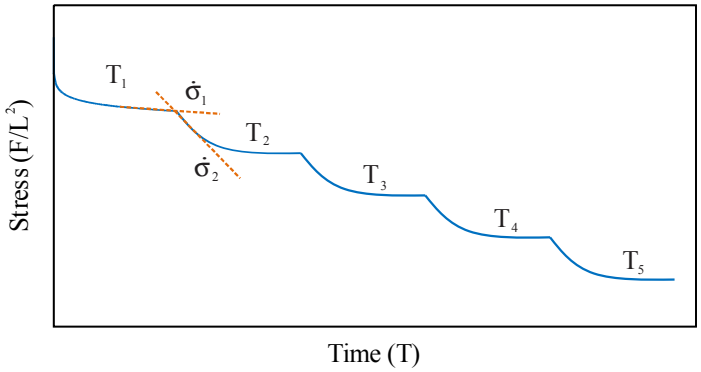

Figure 4.15. Hypothesized temperature step-up stress relaxation test

Still, there are several caveats associated with this approach. First, as recognized by Neu and Sehitoglu (1992), the arbitrary temperature steps should be small to ensure that no significant changes are made to the material microstructure. [For instance, Neu and Sehitoglu (1992) maintained temperature steps of 27 °F.] Second, in contrast to the activation energy-strain rate relationship, Eq. (4.10), the activation energy-stress rate relationship, Eq. (4.16), requires knowledge of the elastic modulus at the various temperature points. However, Schedin et al. (2012) found that the elastic modulus of the UNS S32101 stainless is expected to reduce by only approximately 2.7 percent in a temperature range of approximately 70–170 °F [20–80 °C] (Fig. 4.16). For the purposes of this study, such a small change is considered negligible and Eq. (4.16) is reduced to,

$$Q_{sr} = \frac{R \ln\left(\dot{\sigma}_1 / \dot{\sigma}_2\right)}{\left[1/T_1\right] - \left[1/\left(T_1 + \Delta T\right)\right]} \tag{4.17}$$

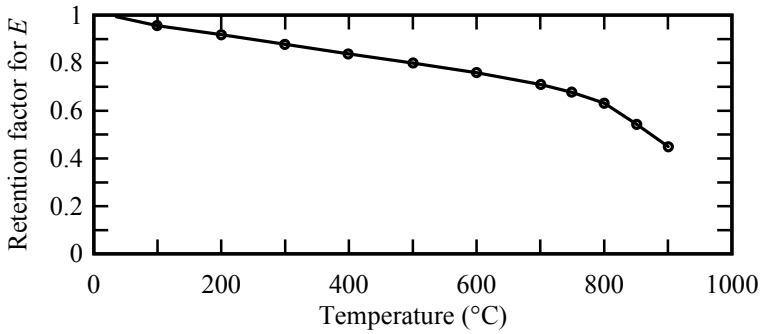

Figure 4.16. Temperature dependence of the elastic moduli of stainless steel [from Schedin et al. (2012)]

4.3.2 Temperature step-up experiments

4.3.2.1 Experimental procedure and test matrix

Similar to the ambient temperature experiments described previously, specimens for the temperature step-up experiments are loaded to an initial strain (at an initial temperature), the strain is held constant for a duration of time, and the relaxing load is measured as a

function of time. But unlike the ambient temperature experiments, dongbone specimens are used for the temperature step-up experiments (Fig. 4.17); an MTS servohydraulic test frame with a 55 kip load cell and a 1-in. gage length temperature-compensated extensometer is used to induce and maintain initial strain (Fig. 4.18); and an MTS environmental chamber is used to control the temperature (Fig. 4.19).

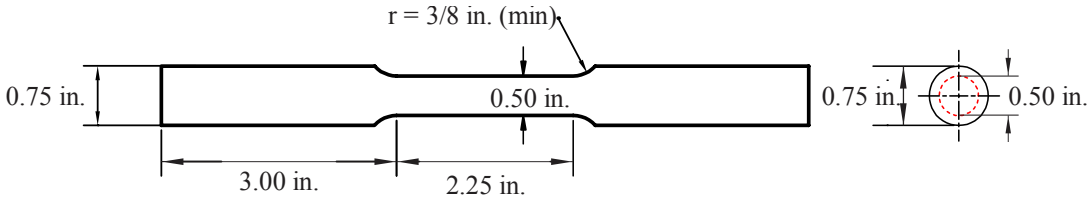

Figure 4.17. Schematic of round dogbone specimen

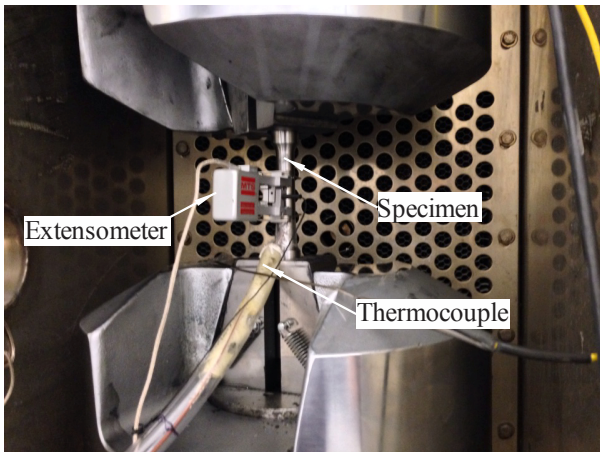

Figure 4.18. Instrumentation and specimen in MTS test frame

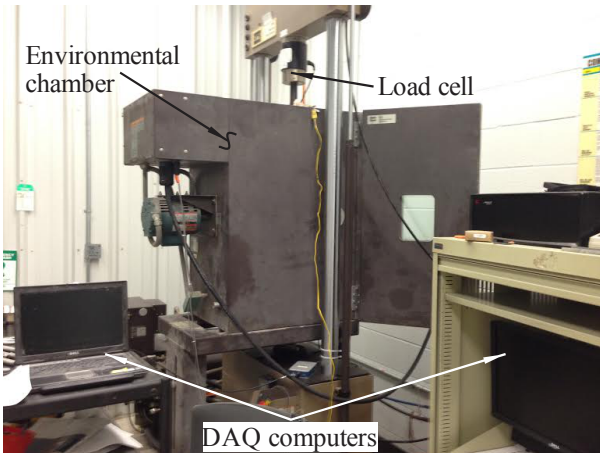

Figure 4.19. MTS test frame and environmental chamber

The dogbone specimens were machined from the as-received prismatic bars using a lathe with water cooling to a geometry specified in ASTM Standard E8 (2009). These specimens were machined to reduce adverse effects due to stress concentrations that form at the transition from the hydraulic wedge-grips and the specimen. Specimens were loaded to five different initial strains (Fig. 4.20) at a strain rate of 0.015 in./in./min, in accordance with ASTM E8 (2009). Four nominal temperature points were considered (70 °F, 100 °F, 125 °F, and 150 °F). The specimens were initially strained and clamped at an ambient temperature condition (nominally, 70 °F). The load was monitored at each temperature step for 1.5 hours, after which the temperature was abruptly increased. However, due to issues with the environmental chamber controller the actual temperature points were (70 ± 6 °F, 100 °F ± 6 °F, 125 F ± 6 °F, and 150 F ± 6 °F).

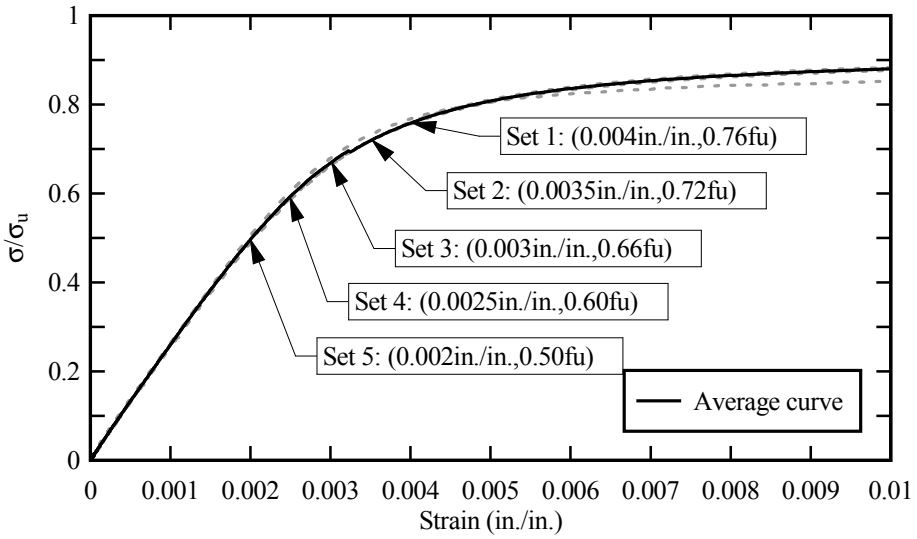

Figure 4.20. Initial loading points for temperature step-up experiments

4.3.2.1 Activation energy experimental results

A total of five temperature step-up experiments—one at each initial strain level presented in Fig. 4.20—were conducted. Load was monitored using a load cell and the strain was

measured using a 1 in.-gage length extensometer with temperature compensation. While Eq. (4.16) requires the instantaneous first derivative of time-stress curve. Finding such a derivative is difficult due to the inherent noise in the data. Hence, the Bažant-Yu viscoplastic constitutive model was fit to each segment of the curve (Fig. 4.21). Time-derivatives of the smooth curves were calculated at the instant of the temperature step-up to obtain the $\dot{\sigma}_1$ and $\dot{\sigma}_2$. Each 25 °F temperature step occurred over a period of approximately 5–10 minutes. The influence of thermal strains was not considered in the analysis used to calculate the slopes of the stress relaxation curves.

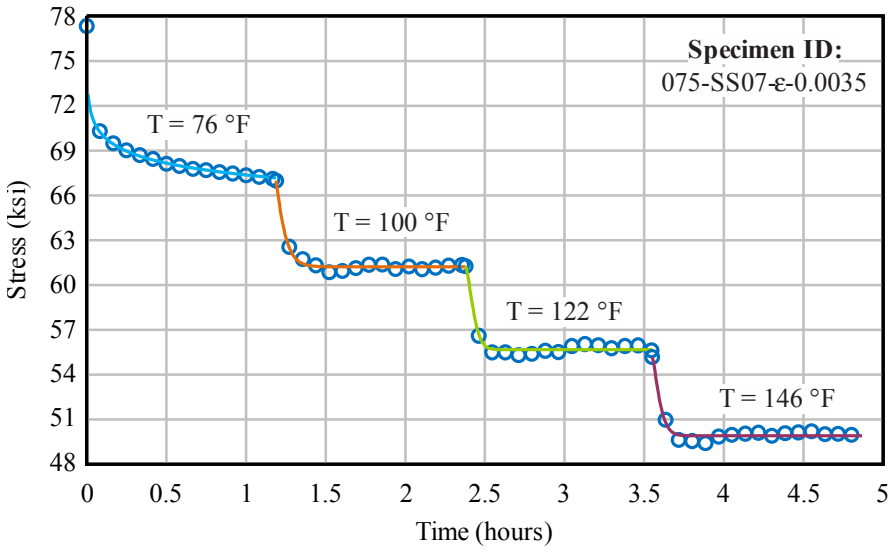

Figure 4.21. Stress relaxation behavior with temperature step-ups

Apparent activation energies associated with stress relaxation for the UNS S32101 stainless steel are presented in Table 4.7 and Fig. 4.22 (with the nominal temperature on the abscissa and activation energy on the ordinate). Table 4.8 gives the temperature at each step-up. No studies could be located in the literature that attempt to quantify the activation energies associated with low temperature creep or stress relaxation for the UNS S32101 stainless steel or any other stainless steel, so direct comparisons to the

results of other step-up experiments cannot be made. However, previous researchers have investigated such behavior for carbon steel. For a carburized steel under creep loading conditions, Neu and Sehitoglu (1992) found the activation energy, Q_c, to be 145,000 J/mole. Similarly, Bažant and Yu (2013) found the activation energy of prestressing strands under stress relaxation conditions, Q_{sr}, to be 121,388 J/mole. Thornton and Hirsch (1958) found the activation energy for creep to be 147,000 J/mole ± 59,000 J/mole for nickel.

Fig. 4.22 shows that the mean-valued activation energy for the UNS S32101 stainless steel is 302,000 J/mole ± 110,000 J/mole (72,000 cal/mole ± 26,000 cal/mole)—approximately twice that of carbon steel. Because this activation energy value cannot be directly compared to those from other studies reported in the literature, future independent studies are necessary to validate the results found here. Full-scale, long-term experiments that rely on the Bažant-Yu activation energy approach, for instance, on specimens loaded to the same initial stress (but several different constant temperatures) would provide valuable information.

Table 4.7. Summary of activation energies for stress relaxation

	Activation energy (J/mole)		
Specimen ID	295 K	312 K	327 K
075-SS-06-ε-0.0040	289,950	233,828	231,275
075-SS-07-ε-0.0035	252,907	374,613	328,518
075-SS-08-ε-0.0030	257,568	317,913	267,407
075-SS-09-ε-0.0025	290,127	331,322	342,200
075-SS-10-ε-0.0020	218,611	381,018	411,728

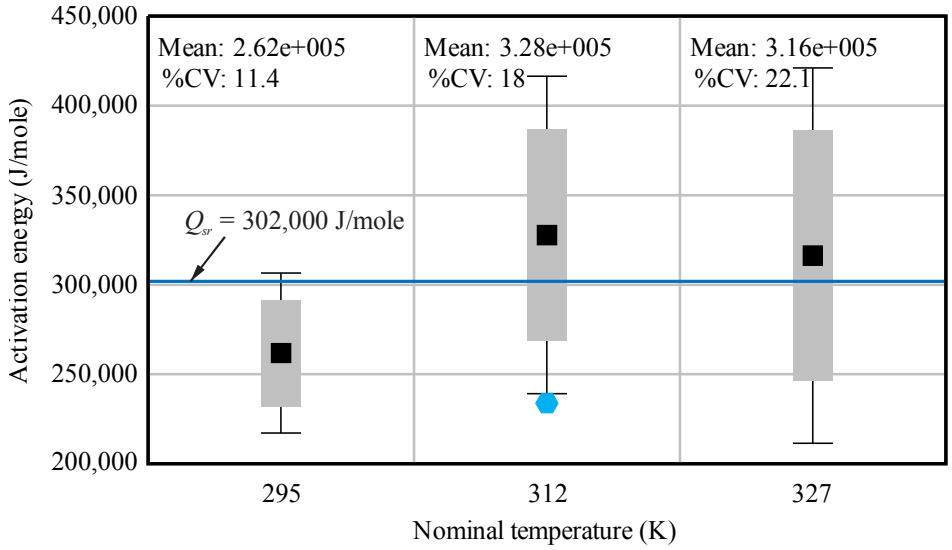

Figure 4.22. Determination of activation energy for stress relaxation

Table 4.8. Temperatures at each step-up point

	Step 1		Step 2		Step 3	
Specimen ID	T_1 (K)	T_2 (K)	T_1 (K)	T_2 (K)	T_1 (K)	T_2 (K)
075-SS-06-ε-0.0040	295	309	312	323	327	336
075-SS-07-ε-0.0035	299	311	312	323	325	337
075-SS-08-ε-0.0030	295	310	311	323	327	338
075-SS-09-ε-0.0025	296	311	312	323	327	339
075-SS-10-ε-0.0020	295	309	312	323	327	337

4.4 Temperature-dependent behavior of the UNS S32101 stainless steel

An increase in temperature will increase the stress relaxation in the UNS S32101 duplex stainless steel, because increasing temperatures increase the flow in metals. In the preceding sections, models have been developed to characterize the long-term, ambient temperature stress relaxation behavior of the duplex stainless steel [Eqs. (4.8) and (4.9)]. Coupling these ambient-temperature models with the activation energy determined in Fig. 4.22 and Eq. (4.2) allows for the characterization of the long-term, temperature-dependent stress relaxation behavior of the UNS S32101 stainless steel.

Eq. (4.2) for $T(t) = 90\ °\text{F}, 110\ °\text{F}, 130\ °\text{F}, 150\ °\text{F}$ and the resulting temperature-adjusted times are substituted into Eqs. (4.8) and (4.9), which were developed from 95th-

percentile characteristic values for stress relaxation at 70 °F. The results show that over a 40-year duration, approximately twice as much stress relaxation occurs at a constant 150 °F when compared to a constant 70 °F (Table 4.9). However, this temperature-induced acceleration is reduced in reality (when compared to constantly elevated temperature case) because the environmental temperature fluctuates daily between 150 °F and 70 °F (Table 4.10) and is not constantly elevated. The values given in Table 4.10 represent factors that amplify the predictions from Eqs. (4.8) and (4.9) to take into account temperature-induced increases in stress relaxation. To summarize, the long-term, temperature-dependent percent stress relaxation, $p_{sr}(t,T)$, of the UNS S32101 stainless steel is given by

$$p_{sr}(t,T) = \alpha_{vt}(T)\, p_{sr}^{70^\circ F} \tag{4.18}$$

where the values of α_{vt} for given maximum temperatures are given in Table 4.10 and α_{vt} = 1.00 for 70 °F and $p_{sr}^{70^\circ F}$ is percent stress relaxation calculated using Eq. (4.8). The above equation represents a conservative estimate—developed from a multitude of experiments conducted on UNS S32101 stainless steel bars in this investigation—for use in designing stainless steel-based pretensioned structural strengthening systems. In addition, based on Eq. (4.8), no stress relaxation will occur if the bars are loaded to $\sigma_0 \le \gamma\sigma_y$, where γ is, conservatively, 0.460, and σ_y is the 0.5% extension under load (EUL) yield stress. Thus, $\sigma_0 \le 0.460\sigma_y$ can be considered the maximum initial stress below which one need not be concerned about the influence of stress relaxation.

Table 4.9. Amplification factors for temperature-induced increases in stress relaxation for constantly elevated temperatures

		Stress relaxation amplification factor, $\alpha_{ct} = p(T)/p_{70°F}$				
	Temperature (°F)	1 year	5 years	10 years	20 years	40 years
Bar diam. = 0.75 in.	90	1.37	1.34	1.33	1.31	1.30
	110	1.76	1.68	1.65	1.62	1.59
	130	2.13	2.00	1.95	1.90	1.59
	150	2.43	2.26	2.19	2.12	2.06
Bar diam. = 1.25 in.	90	1.38	1.34	1.33	1.32	1.30
	110	1.76	1.68	1.65	1.62	1.59
	130	2.14	2.01	1.96	1.91	1.59
	150	2.45	2.27	2.20	2.13	2.07

Table 4.10. Amplification factors for temperature-induced increases in stress relaxation for daily-varying temperatures

		Stress relaxation amplification factor, $\alpha_{vt} = p(T)/p_{70°F}$				
	Temperature (°F)	1 year	5 years	10 years	20 years	40 years
Bar diam. = 0.75 in.	90	1.31	1.28	1.27	1.26	1.25
	110	1.69	1.62	1.59	1.56	1.54
	130	2.07	1.95	1.90	1.86	1.53
	150	2.38	2.21	2.14	2.08	2.02
Bar diam. = 1.25 in.	90	1.31	1.29	1.28	1.26	1.25
	110	1.70	1.62	1.60	1.57	1.54
	130	2.08	1.96	1.91	1.86	1.54
	150	2.39	2.22	2.15	2.09	2.03

4.5 Concluding remarks

In this chapter, the stress relaxation behavior of the UNS S32101 stainless steel was explored. A series of full-scale experiments were conducted to characterize the long-term behavior of the material at ambient temperature. A series of small-scale experiments were also conducted to determine the activation energy associated with stress relaxation. These activation energy experiments were based on a new technique formulated from the existing literature. The activation energy found was used to characterize the temperature-dependent behavior of the material. Finally, a phenomenological model—derived from fundamental mechanics—is proposed. This model (the Bažant-Yu viscoplastic constitutive model) predicts long-term time- and temperature-dependent viscoelastic behavior, is valid for stresses $\sigma_0 / \sigma_u \leq 0.75$ and temperatures $70\,°\text{F} \leq T \leq 150\,°\text{F}$, and can be readily incorporated into current methodologies for designing structural strengthening

systems. Furthermore, no stress relaxation will occur if a bar is loaded an initial stress value, $\sigma_0 \leq 0.460\sigma_y$, where σ_y is the 0.5% EUL yield stress.

Chapter 5

Structural behavior of strengthened pier caps

Reinforce concrete bridge pier caps strengthened with external pretensioned systems must be analyzed using the strut-and-tie method (Zureick et al. 2014). This chapter deals with the mechanical behavior of pier caps strengthened using a stainless steel-based pretensioned system.

5.1 Pretensioned clamp strengthening system

The state of Georgia currently employs a clamp-based system to strengthen existing bridge pier caps, as illustrated in Figure 1.1. The system involves placing channels at the top and bottom of a pier cap and uses pretensioned threaded bars (installed on both sides of the pier cap) to induce a compressive force in the pier cap. The elements typical installation procedure is illustrated in Fig. 5.1. The strain in the threaded stainless steel bars is held constant over time using nuts.

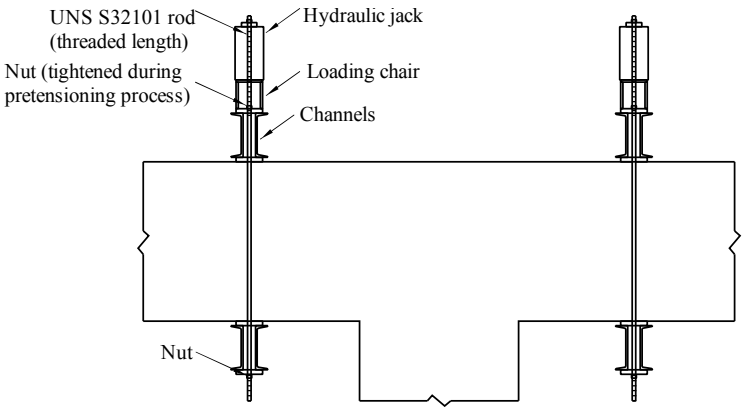

Figure 5.1. Components of the pretensioned clamp system installed on a bridge pier cap

5.2 Strut-and-tie model for strengthened pier caps

Strut-and-tie modeling is based on the lower-bound theorem of plasticity and involves transforming an RC deep beam to an equivalent truss system (Collins and Mitchell 1986; Schlaich et al. 1987). This truss model provides a visual of the flow of loads through the deep beam (Fig. 2.5). ACI (2011), AASHTO (2010), and CEB-FIP (1990), have presented the approach for the design of new members. An approach is presented here for the evaluation of existing bridge pier caps and the design of strengthening systems for those members.

The approach satisfies the requirements of §5.6.3 of AASHTO (2010)—the specification governing the design of bridges in the United States—in a simple and consistent way. Furthermore, the proposed approach's algorithmic nature allows for the development of computer programs. Models for use with fiber-reinforced polymer (FRP) and carbon steel strengthening systems have been developed by Bechtel (2011) and O'Malley (2011), respectively.

5.2.1 Strut-and-tie model for existing (unstrengthened) pier cap

In contrast to the analysis of new structures, the analysis of existing structures is constrained by the geometry of the actual structure. Fig. 2.5a shows a model of an existing (unstrengthened) bridge pier cap with an idealized truss model—with a single-strut mechanism—superimposed on it. The known variables in the model are the geometric properties of the structure: the width of the bearings (l_b), the width of the pier column (l_c), the location of the primary longitudinal reinforcement (d_s, d_s'), and the shear span (a_{span}). Using these known parameters, the geometry of the truss can be

computed: the height of the nodes (h_{a1}, h_{a2}), the angle of the diagonal strut (θ_{s1}), as well as the width of the diagonal strut (w_{s1}).

Determining the truss geometry is the initial step in establishing a strut-and-tie model. First, the heights of the nodes are established. (The widths of the nodes are assumed to be the same as the bearing lengths.) There are two types of nodes in a bridge pier cap: the nodes on the tensile face (nodes 1 and 4 in Fig. 2.5a) and the nodes on the compressive face (nodes 2 and 3 in Fig. 2.5a). The height of the nodes on the compressive face is determined using flexural analysis. Explicitly, the height of the compressive nodes (h_{a1}, h_{a2}) is taken as the depth of the Whitney compression block, *a* (Fig. 5.2):

$$h_{a2} = h_{a3} = a = \beta_1 c \tag{5.1}$$

where β_1, a factor that depends on the compressive strength of the concrete, ranges from 0.85 for concretes having strengths of 4 ksi or lower to 0.65 for concretes having strengths of 8 ksi of above (ACI 2008); and *c* is the depth of the axis of zero strain (or, simply, the neutral axis).

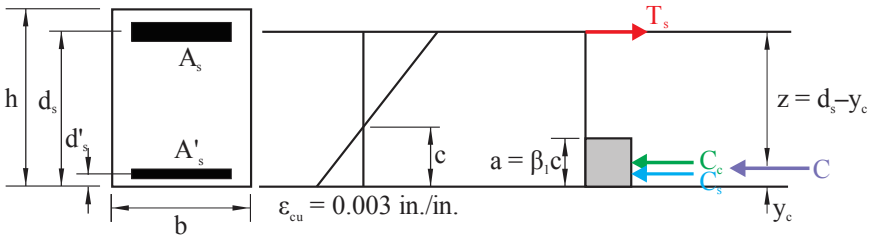

Figure 5.2. Calculating the depth of the Whitney compressive block

Conversely, the height of the nodal zones on the tensile face is calculated by equilibrating the forces in the horizontal direction (the force of the tie is resisted by bearing on the concrete). Fig. 5.3 shows the forces acting on node 1. The height is based

on the strain in the tension tie and the reduced concrete strength in the node [as proposed by Bechtel (2011)],

$$h_{a1} = h_{a4} = \frac{\varepsilon_{tie} A_s E_s}{\lambda f_c' b_{eff}} \tag{5.2}$$

where ε_{tie} is the assumed strain in the tension tie; A_s the area of tension steel; E_s the modulus of elasticity of steel; f_c' the compressive strength of concrete; b_{eff} the effective width (thickness) of the pier cap; and λ is a factor that reduces the compressive strength of the concrete in nodal zones that experience non-hydrostatic loading conditions in the following manner (AASHTO 2010):

$$\begin{aligned} &\lambda = 0.85 \text{ for CCC (hydrostatic) nodes} \\ &\lambda = 0.75 \text{ for CCT nodes} \\ &\lambda = 0.65 \text{ for CTT nodes} \end{aligned} \tag{5.3}$$

For example, a reduction factor of 0.75 is used for node 1 (Fig. 5.3) because it anchors a one-directional tension tie, making it a compression-compression-tension (CCT) node. Additionally, however, AASHTO (2010) requires that the height of a node anchored by bearing and reinforcement be limited by the distance from the tensile face to the tensile reinforcement layer closest to the neutral axis (d_1) and six times the diameter of the tensile reinforcement bars (d_b). In other words,

$$(h_{a1})_{\max} = d_1 + 6d_b \tag{5.4}$$

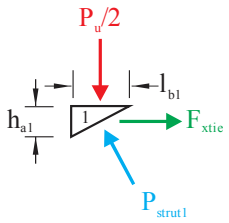

Figure 5.3. Free body diagram showing the forces acting on node 1

Once the heights of the nodes are determined and their centers are located, the truss geometry can be established as a function of the shear span (a_{span}) and the vertical distance between the nodes (Fig. 5.4),

$$\theta_{s1} = \arctan\left(\frac{d - \frac{h_{a1}}{2} - \frac{h_{a2}}{2}}{a_{span} - \frac{l_{c2}}{2}}\right) \tag{5.5}$$

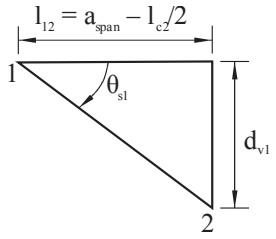

Figure 5.4. Geometry of the truss

After the width of the strut has been calculated using the following geometric relationship (the unstrengthened pier cap only has one strut)

$$w_s = l_b \sin(\theta_{s1}) + h_a \sin(\theta_{s1}) \tag{5.6}$$

the nominal stress in that strut can be computed by the dividing the force in that strut (obtained from static truss analysis) by the area of the strut

$$f_{s1} = \frac{F_{s1}}{w_{s1} b_v} \tag{5.7}$$

where b_v is the width of the pier cap. This nominal stress in that strut must be lower than the allowable stress for that strut, f_{cuS} , defined as (AASHTO 2010):

$$f_{cuS} = \min\left(\frac{f_c'}{0.8 + 170\varepsilon_l}, 0.85 f_c'\right) \tag{5.8}$$

Here, ε_l is computed as a function of the stain in the tension tie supporting that strut and the angle of the strut as follows

$$\varepsilon_l = \varepsilon_s + (\varepsilon_s + 0.002)\cot^2(\theta_{s1}) \tag{5.9}$$

Since the algorithm is based on the initial value of the strain in the tension tie, these equations can be iterated till the nominal stress in all compression struts is lower than the allowable stress for that strut (i.e., the initial strain in the tension tie should be lowered till no member fails). Additionally, checks must be performed to ensure that the capacities of the bearing locations are not exceeded.

5.2.2 Strut-and-tie model for strengthened pier cap

O'Malley (2011) showed that the pretensioned clamp system increases the strength of the pier cap by forming a second diagonal strut (Fig. 2.5b). A model is presented here to analyze the strength of pier caps strengthened with the stainless steel-based system introduced earlier. The model follows the same basic algorithm as the strut-and-tie model for the unstrengthened pier cap, but requires some modifications: 1) a pretension force is introduced; 2) a second diagonal strut is made apparent; 3) a horizontal strut is added.

As before, the known quantities are the geometry of the pier cap. While a method to calculate the required pretension force, P_{clamp}, is presented later, an arbitrary value may be used in the strut-and-tie procedure, since the pretension force is self-equilibrating. A procedure to calculate the geometry of each truss element, its nominal stress, and its limit stress is presented in Table 5.1. The variables used in that table are labeled in Fig. 5.5.

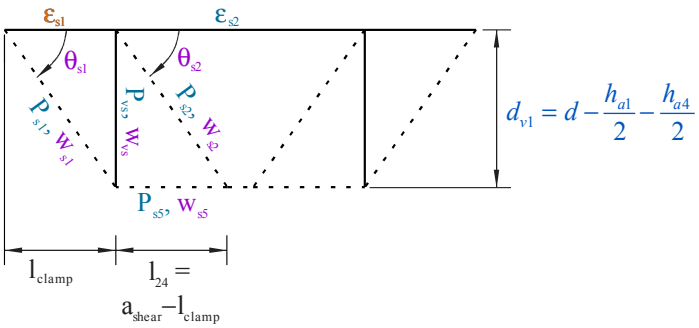

Figure 5.5. A truss analogy for a strengthened bridge pier cap

Table 5.1. Parameters for the strut-and-tie model of strengthen pier caps

Element type	Geometry	Nominal stress	Limit stress
Compression node (nodes 2, 4, 5, 7 in Fig. 2.5b)	1. Width: $l_{b,i}$ or $l_{c,i}$ 2. Height (from flexural analysis, Eq. 5.): $h_{a,i} = a$	$f_{n,j} = \frac{P_j}{A_j}$; where j is the direction of loading	$f_{cn} = \lambda f_c'$; λ given in Eq. 5.3
Tension node (nodes 1, 3, 6, 8 in Fig. 2.5b)	1. Width: $l_{b,i}$ 2. Height (from strain in tension tie anchoring node 1, Eq. 5.2): $h_{a,i} = h_{a1} = \frac{\varepsilon_{s1} A_s E_s}{\lambda_{n1} f_c' b_v}$	$f_{n,j} = \frac{P_j}{A_j}$; where j is the direction of loading	$f_{cn} = \lambda f_c'$; λ given in Eq. 5.3
Diagonal struts 1 and 4 (symmetric)	1. Strut angle: $\theta_{s1} = \arctan\left(\frac{d_{v1}}{l_{clamp}}\right)$ 2. Min. width of strut: $w_{s1} = l_b \sin(\theta_{s1}) + h_a \sin(\theta_{s1})$	$(f_{s1})_n = \frac{P_{s1}}{w_{s1} b_v}$; where b_v is the width of the pier cap	$(f_{s1})_{cu} = \min\left(\frac{f_c'}{0.8+170\varepsilon_l}, \cdots\right)$ $(\cdots, 0.85 f_c')$ where: $\varepsilon_l = \varepsilon_{s1} + (\varepsilon_{s1} + 0.002)\cot^2(\theta_{s1})$
Diagonal struts 2 and 3 (symmetric)	1. Strut angle: $\theta_{s2} = \arctan\left(\frac{d_{v1}}{l_{24}}\right)$ 2. Min. width of strut: $w_{s2} = l_b \sin(\theta_{s2}) + h_a \sin(\theta_{s2})$	$(f_{s2})_n = \frac{P_{s2}}{w_{s2} b_v}$; where b_v is the width of the pier cap	$(f_{s2})_{cu} = \min\left(\frac{f_c'}{0.8+170\varepsilon_l}, \cdots\right)$ $(\cdots, 0.85 f_c')$ where: $\varepsilon_l = \varepsilon_{s2} + (\varepsilon_{s2} + 0.002)\cot^2(\theta_{s2})$
Horizontal struts 5 and 6 (symmetric)	1. Strut angle: $\theta_{s5} = 0$ 2. Width of strut: $w_{s5} = h_a$	$(f_{s5})_n = \frac{P_{s5}}{w_{s5} b_v}$; where b_v is the width of the pier cap	$(f_{s2})_{cu} = 0.85 f_c'$
Tension ties	Strain (initial guess or calculated from truss analysis): ε_{s1}, ε_{s2}	$(f_{t,i})_n = \frac{E\varepsilon_{s,i}}{A_s}$	$(f_{t,i})_u = f_y$; where f_y is the yield stress of the steel

5.3 Calculation of maximum pretension force

The upper limit of the pretension clamp force is governed by the following limit states:

- bearing failure of concrete ($P_{bearing}$);
- crushing of the vertical strut formed by the pretension clamp force ($P_{crushing}$);

- splitting of the vertical strut by excessive transverse tensile stresses ($P_{splitting}$); and
- tensile load limit of the stainless steel bar (P_{ubar}).

Hence, the maximum pretension clamp force is given by

$$P_{clamp} \le \min(P_{bearing}, P_{crushing}, P_{splitting}, P_{ubar}) \tag{5.10}$$

5.3.1 Bearing failure of concrete

The bearing strength of the concrete supporting the pretension clamps is given by

$$P_{clamp} \le 0.75\varphi f_c' A_b \tag{5.11}$$

where φ is taken as 0.70 and A_b is the area of bearing. For pier caps, Eq. (5.11) simplifies to, approximately,

$$P_{bearing} \le \frac{0.5 f_c' l_b b_v}{n_{bars}} \tag{5.12}$$

where n_{bars} is the number of bars supported by the clamp.

5.3.2 Crushing of concrete in compression

The strength of the diagonal struts (Fig. 2.5b) is controlled the nominal compression stress exceeding its limit stress. The principle given in Eqns. (5.7) and (5.8) applies here as well, except the width of the strut is taken to be the bearing width of the pretension clamp system (Fig. 5.6)

$$w_s = l_{b2} \tag{5.13}$$

In addition, the limit stress in the strut is given by:

$$f_{cuS} = \frac{P_{clamp}}{w_s b_v} = \lambda f_c' \tag{5.14}$$

where λ is given by Eq. (5.3). However, λ can be conservatively taken as 0.65. Hence the maximum pretension clamp force for this limit state is, simply

$$P_{crushing} = \frac{0.65 f'_c w_s b_v}{n_{bars}} \tag{5.15}$$

where n_{bars} is the number of bars supported by the strut.

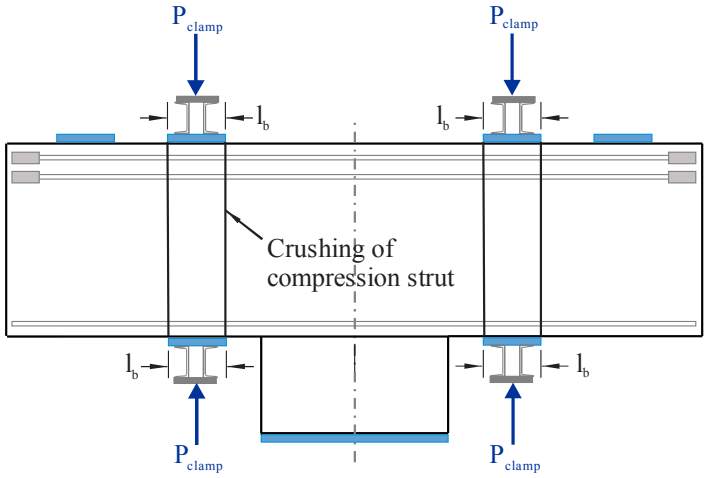

Figure 5.6. Crushing of vertical strut

5.3.3 Splitting of strut due to transverse tensile cracking

A highly localized and discontinuous stress state is present at the end zone of a concrete section under concentrated loading (Magnel 1949; Al-Saadoun 1980). At distances farther away from the point of load application, the stresses become uniformly distributed in the longitudinal direction. However, as the stresses progress from discontinuous to uniform, complex transverse tensile and shear stresses form in the member (Al-Saadoun 1980). These transverse tensile stresses can be significant and have been shown to cause cracking in pier caps with pretensioned clamp systems, as shown in Fig. 5.7 (O'Malley 2011).

These transverse tensile stresses have been analyzed using the theory of elasticity and have been used for the design of prestressed concrete members (Magnel 1949; Guyon 1953). Guyon (1953) developed isobars for the maximum transverse tensile stresses that form in terms of the mean compression, *f*, for a uniformly distributed load

(Fig. 5.8). As can be seen in Fig. 5.8, a maximum tensile stress that is equal to 34 percent of the mean compression stress forms in the cross-section. Setting this maximum tensile stress equal to the rupture stress of the concrete gives a relationship for the allowable pretension clamp force to prevent the tensile splitting of the concrete:

$$0.23\sqrt{f_c'} = 0.34f \tag{5.16}$$

where f_c' is the compressive strength of the concrete and f is the mean bearing stress caused by the pretension clamp is computed as a function of the pretension clamp force, P_{clamp}, the bearing width of the clamp, l_b, and the thickness of the pier cap, b_v

$$f = \frac{P_{splitting}}{l_b b_v} \tag{5.17}$$

Substituting Eq. (5.17) into Eq. (5.16) the maximum allowable pretension clamp force for the limit state where tensile splitting of the concrete section occurs is given as simply:

$$P_{splitting} = \frac{0.68\sqrt{f_c'} l_b b_v}{n_{bars}} \tag{5.18}$$

where n_{bars} is the number of bars supported by the clamp.

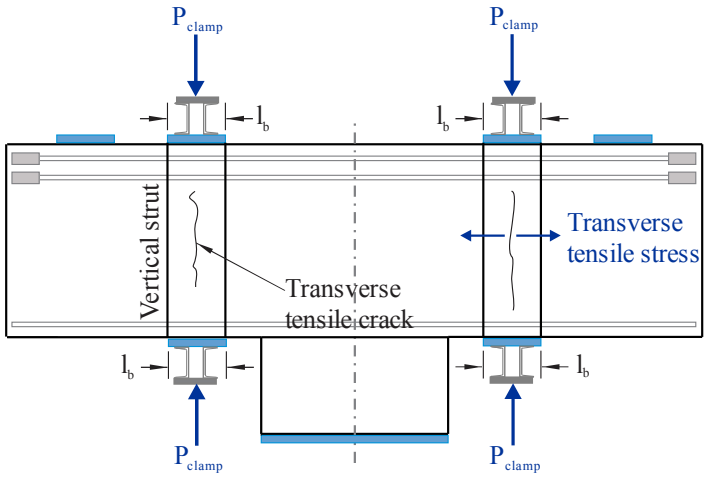

Figure 5.7. Formation of a transverse tensile crack

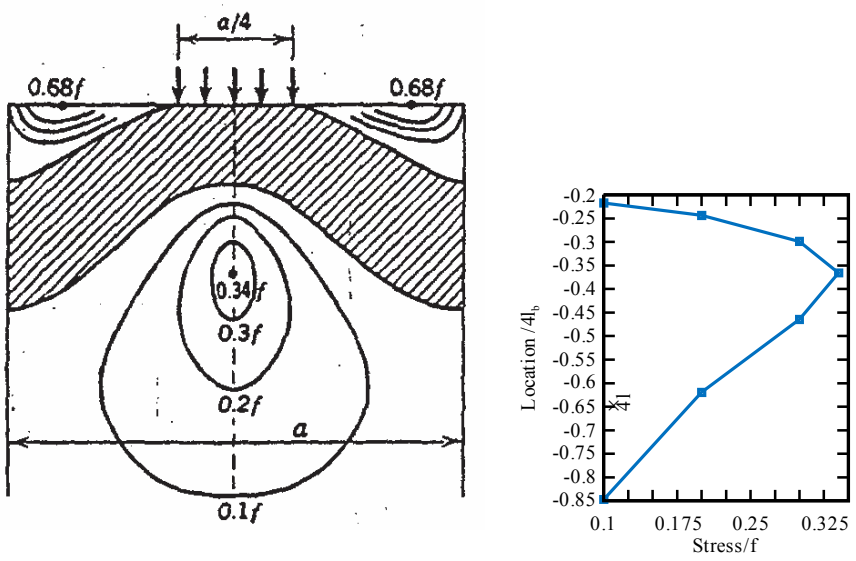

Figure 5.8. Transverse tensile stresses due to distributed load on a rectangular beam [from Guyon (1953) and Lin and Burns (1981)]

5.3.4 Tensile load limit of the stainless steel bar

The Bažant and Yu viscoplastic model [Eq. (4.8)] suggests that no stress relaxation will occur in the UNS S32101 stainless steel if the initial pretension force, σ_0, is lower than $0.460\sigma_y$. Thus, to simply remove concerns of the adverse influence of stress relaxation on the long-term performance of the pretension strengthening system,

$$P_{ubar} \le 0.460\sigma_y A_{bar} \tag{5.19}$$

where σ_y is 0.5% extension under load and A_{bar} is cross-sectional the area of the bar. It should be noted here that Eq. (5.19) assumes a unixal state of loading. Hence, care should be taken to ensure that eccentric loads (i.e., those loads causing flexure) are not induced in the bars.

5.4 Validation of strut-and-tie model for strengthened pier cap

O'Malley (2011) studied the behavior of a carbon steel-based pretensioned clamp system to strengthen RC bridge pier caps by testing full-scale specimens. The experimental data from that investigation provides benchmark values to validate the strut-and-tie models developed in the previous section. Three pier cap specimens from the O'Malley (2011) study are selected and analyzed.

To ensure a wide range of pier cap geometry, two specimens (3-S-PT and 5-S-CR-PT2) include the minimum amount of transverse reinforcement required by AASHTO (2010) and one does not (4-NS-CR-PT). Furthermore, the stainless steel-based pretensioned clamp systems may be installed on pier caps with existing cracks. Hence, to validate that the strut-and-tie approach can model both uncracked and cracked pier caps, two of the selected pier caps (4-NS-CR- PT and 5-S-CR-PT) were loaded to induce cracking before the pretensioned clamp was installed.

All three pier caps tested by O'Malley (2011) and analyzed here had depths of 36 in. (a typical pier cap depth in the state of Georgia) and shear spans, a_{shear}, of 50 in (Fig. 5.9 shows the two specimens with the minimum transverse reinforcement and Fig. 5.10 shows the one without). Table 5.2 summarizes the pretension force applied in each pier cap specimen as well as the compression strength of the concrete and yield strength of the reinforcement. Table 5.3 provides a synopsis of the key results of the analysis. The

results show that the proposed strut-and-tie model predicts conservative strength for RC bridge pier caps strengthened with pretensioned clamp-based systems (Fig. 5.11).

Table 5.2. Summary of key input parameters for O'Malley (2011) specimens

Specimen ID	Pretension force (kips)		Concrete compressive strength (ksi)	Steel yield stress (ksi)
	Span 1	Span 2		
3-S-PT	265	256	3.55	73.0
4-NS-CR-PT	210	213	3.08	73.0
5-NS-CR-PT2	223	212	3.64	73.0

Table 5.3. Summary of test results for O'Malley (2011) specimens

Specimen ID	Experimentally determined capacity (kips)	Strut-and-tie capacity (kips)	V_{exp} / V_{calc}	Predicted failure mode
3-S-PT	287	207	1.39	Tension tie yielding
4-NS-CR-PT	299	204	1.46	Tension tie yielding
5-NS-CR-PT2	307	208	1.48	Tension tie yielding

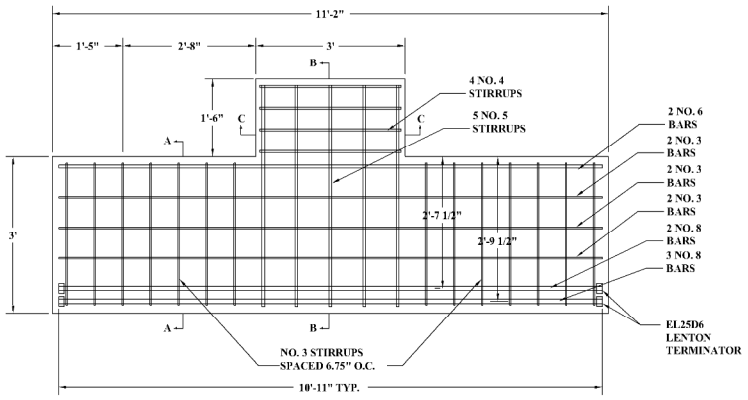

a)

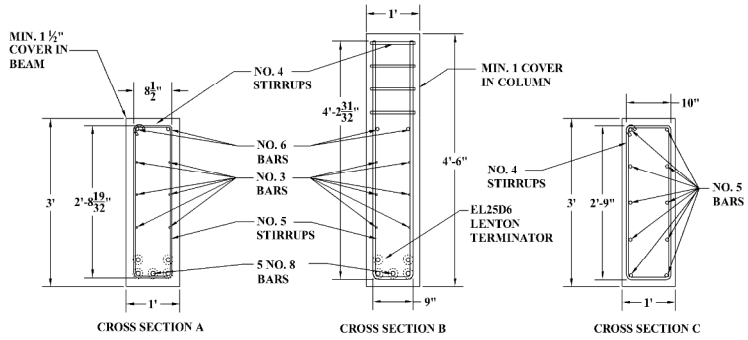

b)

Figure 5.9. Schematic of specimen ID 3-S-PT and 5-S-CR-PT2: a) elevation view; b) cross-sectional views [O'Malley (2011)]

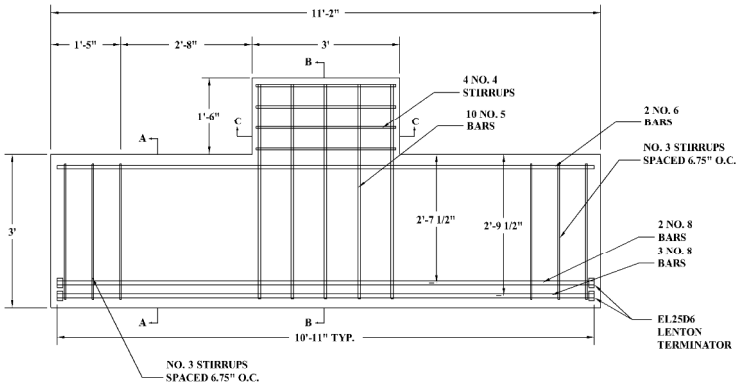

a)

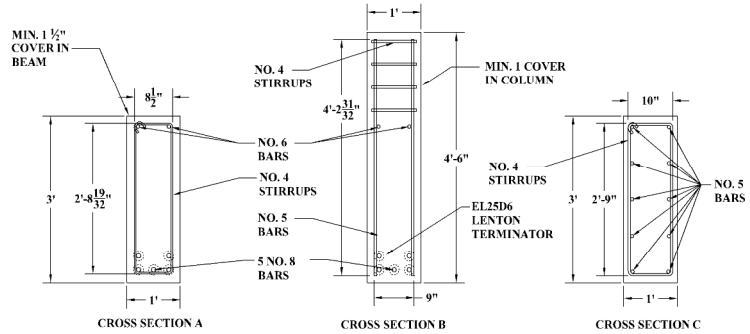

b)

Figure 5.10. Schematic of specimen IDs 4-NS-CR-PT: a) elevation view; b) cross-sectional views [O'Malley (2011)]

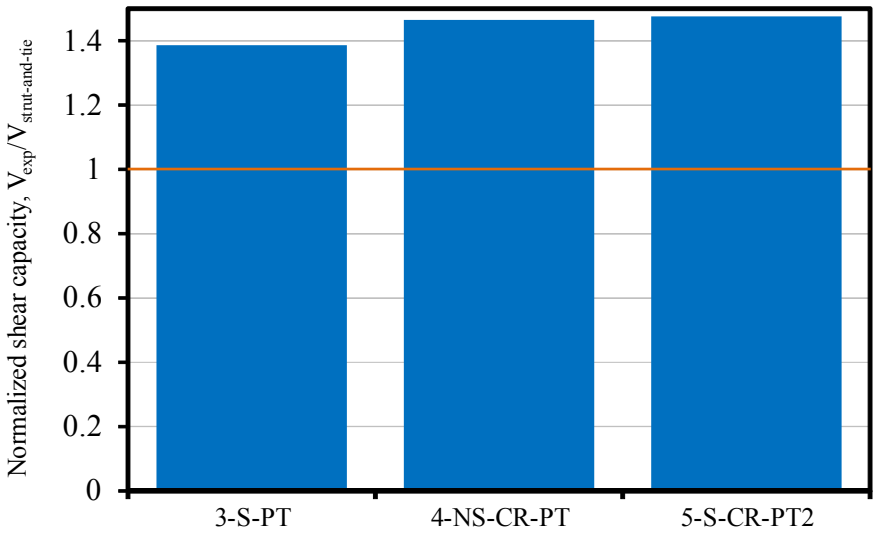

Figure 5.11. Comparison of experimental capacity with proposed strut-and-tie model

5.5 Conclusion

In this chapter, a strut-and-tie-based methodology for the design of pretensioned clamp systems to strengthen reinforced concrete bridge pier caps was presented. This model was validated against results of full-scale experiments conducted by O'Malley (2011). Guidelines are provided to calculate the maximum (upper-bound) pretension force.

Chapter 6
Conclusions and recommendations

6.1 Summary

The present investigation addressed a problem related to the strengthening of reinforced concrete bridge pier caps by means of an external pretension system that uses stainless steel bars. Previous studies have suggested that a minimum pretension force may be required for the effective performance of such strengthening systems. However, stress relaxation can lead to a decrease in the pretension force over time. This investigation characterized the stress relaxation behavior of the UNS S32101 stainless steel through a combined experimental and analytical approach. Twenty short-term stress relaxation experiments (with durations ranging between 260–1000 hours) were conducted at ambient temperature conditions. Additionally, five experiments were conducted at temperatures ranging from 70 °F to 150 °F to determine the activation energy for stress relaxation.

Data from these experiments were used to develop a viscoplastic constitutive model to describe the time- and temperature-dependent behavior of the stainless steel bars. Using a two-parameter Weibull distribution, 95th-percentile characteristic upper-bound values of percent stress relaxation at various time steps were found. These upper-bound values may be used for the design of stainless steel-based strengthening systems.

Recommendations were also made regarding the pretension force in the strengthening system. These recommendations account for the stress relaxation behavior of the UNS S32101 stainless steel.

6.2 Recommendations for further research

Due to the limitations of the present study, it is recommended that the following topics be considered for further research:

1. The stress relaxation behavior of various duplex stainless steel alloys.
2. Effect of threading on the stress relaxation behavior of pretensioned stainless steel bars.
3. Influence of thermal strain and thermal cycling on the performance of the strengthening system.
4. Dependence of stress relaxation on the material's microstructure (e.g., austenite-ferrite balance or grain orientation).
5. Creep and stress relaxation in duplex stainless steels under flexural loading conditions.
6. Examination of the microstructural mechanisms that govern stress relaxation in the UNS S32101 stainless steel and other duplex alloys. Studies may consider the mechanisms that control the time-dependent aspects of low-temperature plasticity (i.e., thermal obstacles such as the Peierls-Nabarro stress, forest dislocations, climb of edge dislocations, etc.).

References

AASHTO. (2010). *LRFD bridge design specifications with 2010 interim revisions*, 5th Ed., Washington, D.C.

ACI. (2011). *Building code requirements for structural concrete (ACI 318-11)*, Farmington Hills, Mich.

Al-Saadoun, S. S. (1980). "A three-dimensional photoelastic investigation of the stress distribution in the anchorage zone of post-tensioned beams." Masters' thesis, Dept. of Civil Engineering, King Fahd University of Petroleum and Minerals, Dhahran, Saudi Arabia.

ASCE. (2002). *Specifications for the design of cold-formed stainless steel structural members (SEI/ASCE 8-02)*, Reston, Va.

ASCE-ACI Committee 445 on Shear and Torsion. (1998). "Recent approaches to shear design of structural concrete." *Journal of Structural Engineering*, 124(12), 1375–1471.

ASM. (2009). *ASM handbook volume 9: Metallography and microstructures*, G. F. Vander Voort, ed., ASM International, Materials Park, Ohio

ASTM. (2009). Standard test methods for tension testing of metallic materials, ASTM E8, Conshohocken, Pa.

ASTM. (2010). Standard test method for Young's modulus, tangent modulus, and chord modulus, ASTM E111-04, Conshohocken, Pa.

ASTM. (2008). Standard test methods for stress relaxation for materials and structures, ASTM E328-02, Conshohocken, Pa.

Atienza, J. M., and Elices, M. (2007). "Role of residual stresses in stress relaxation of prestressed concrete wires." *Journal of Materials in Civil Engineering*, 19(8), 703–708.

Bažant, Z. P., and Cedolin, L. (2010). *Stability of structures: Elastic, inelastic, fracture and damage theories*, World Scientific, Hackensack, N.J.

Bažant, Z. P., and Yu, Q. (2013). "Relaxation of prestressing steel at varying strain and temperature: Viscoplastic constitutive relation." *Journal of Engineering Mechanics*, 139(7), 814–823.

Bechtel, A. J. (2011). "External strengthening of reinforced concrete pier caps." Ph.D. thesis, Sch. of Civil and Environmental Engineering, Georgia Institute of Technology, Atlanta, Ga.

Beese, A. M., and Mohr, D. (2009). "Experimental quantification of phase transformation in austenitic stainless steel." *Proceedings, SEM Annual Conference*, Society for Experimental Mechanics, Albuquerque, N.M.

Bhattacharya, B. (1997). "A damage mechanics-based approach to structural deterioration and reliability." Ph.D. thesis, Dept. of Civil Engineering, Johns Hopkins University, Baltimore, Md.

Bhattacharya, B., and Ellingwood, B. R. (1999). "A new CDM-based approach to structural deterioration." *International Journal and Solids and Structures*, 36, 1767–1779.

Comité Euro-International du Béton (CEB-fip). (1990). *CEB-fip model code 1990: Model code for concrete structures*, Thomas Telford Services Ltd., London, U.K.

Chaboche, J. L. (1988a). "Continuum damage mechanics: Part I." *Journal of Applied Mechanics*, 55, 59–64.

Chaboche, J. L. (1988b). "Continuum damage mechanics: Part II." *Journal of Applied Mechanics*, 55, 65–72.

Christensen, R. M. (1971). *Theory of viscoelasticity: An introduction*, Academic Press, New York.

Christensen, R. M. (2004). "A probabilistic treatment of creep rupture behavior for polymers and other materials." *Mechanics of Time-Dependent Materials*, 8, 1–15.

Chun, K. J., and Hubbard, R. P. (2007). "Development of a reduced relaxation function and comparison of stress relaxation for anatomically paired tendons." *Journal of Mechanical Science and Technology*, 23, 1893–1898.

Collins, M. P., and Mitchell, D. (1986). "Rational approach to shear design—the 1984 Canadian code provisions." *ACI Journal*, 83(6), 925–933.

Conrad, H. (1964). "Thermally activated deformation of metals." *Journal of Metals*, 16(7), 532–588.

Cotrell, A. H. (1964). *The mechanical properties of matter*, Wiley, New York.

Cotrell, A. H. (1997). "Logarithmic and Andrade creep." *Philosophical Magazine Letters*, 75(5), 301–307.

Ellingwood, B. R. (2003). "Toward load and resistance factor design for fiber-reinforced polymer composite structures." *Journal of Structural Engineering*, 129(4), 449–458.

Findley, W. N., Lai, J. S., and Onaran, K. (1969). *Creep and relaxation of nonlinear viscoelastic materials*, North-Holland Publishing, Toronto.

Fischer. (2002). *Operator manual FERITSCOPE® MP30*, Helmut Fischer GMBH, Sindelfingen, Germany.

Freudenthal, A. M. (1960). "Prediction of fatigue life." *Journal of Applied Physics*, 31(12), 2196–2198.

Garofalo, F. (1965). *Fundamentals of creep and creep-rupture in metals*, Macmillan, New York.

Gedge, G. (2008). "Structural uses of stainless steel—buildings and civil engineering." *Journal of Constructional Steel Research*, 64, 1194–1198.

Guo, J., Zhang, W., and Sun, X. (2012). "Stress relaxation continuum damage constitutive equations for relaxation performance prediction." *Advanced Materials Research*, 455/456, 1434–1437.

Guyon, Y. F. (1953). *Prestressed concrete*, Contractors Record, London.

Hildebrandt, T. H. (1938). "Definitions of Stieltjes integrals of the Riemann type." *The American Mathematical Monthly*, 45(5), 265–278.

Idermark, S. U. V., and Johansson, E. R. (1979). "Room temperature stress relaxation of high-strength strip wire and spring steels—procedures and data." *Stress Relaxation Testing*, Alfred Fox, ed., ASTM STP 676, 61–77.

Johansson, P., and Liljas, M. (2002). "A new lean duplex stainless steel for construction purposes," *4th European Stainless Steel Science and Market Congress*, Paris.

Johansson, P., and Prošek, T. (2007). "Stress corrosion cracking properties of UNS S32101." *Acom*, 2-2007, OutoKumpu.

Kachanov, L. M. (1986). *Introduction to continuum damage mechanics*, Martinus Nijhoff Publishers, Dordrecht, The Netherlands.

Kachanov, L. M. (1958). "Rupture time under creep conditions." *International Journal of Fracture*, 97, xi–xviii. Originally published in Russian in 1958, English translation published in 1999.

Kim, S.-H. (2014). "Experimental and analytical investigation of reinforced concrete bridge pier caps with an externally bonded stainless steel system." Ph.D. thesis, Sch. of Civil Engineering, Georgia Institute of Technology, Atlanta, Ga.

Kim, S.-J., Kim, W.-G., Jung, I.-H., Kim, Y.-W. (2010). "Statistical analysis of creep crack growth behavior in modified 9Cr-1Mo steel." *Materials Science Forum*, 645, 516–519.

Kostenko, Y., Lvov, G., Gorash, E., Altenbach, H., and Naumenko, K. (2006). "Power plant component design using creep-damage analysis." *Proceedings, 2006 ASME International Mechanical Engineering Congress and Exposition*, American Society of Mechanical Engineers, Chicago, Ill.

Krapf, C. N. (2010). "Stress relaxation of post-tensioned stainless steel rods for bridge pier cap strengthening." M.S. thesis, Sch. of Civil and Environmental Engineering, Georgia Institute of Technology, Atlanta, Ga.

Krempl, E. (1979). "An experimental study of room-temperature rate-sensitivity, creep, and relaxation of AISI Type 204 stainless steel." *Journal of Mechanics and Physics of Solids*, 27, 363–375.

Kujawski, D., Kallianpur, V., and Krempl, E. (1980). "An experimental study of uniaxial creep, cyclic creep, and relaxation of AISI Type 304 stainless steel and room temperature." *Journal of Mechanics and Physics of Solids*, 28, 129–148.

Ladson, L. S., Waren, A. D., Jain, A., Ratner, M. (1978). "Design and testing of a generalized reduced gradient code for nonlinear programming." *ACM Transactions on Mathematical Software*, 4(1), 34–50.

Lemaitre, J. (1984). "How to use damage mechanics." *Nuclear Engineering and Design*, 80, 233–245.

Lemaitre, J. (1996). *A course on damage mechanics*, Springer, New York.

Langhaar, H. L. (1962). *Energy methods in applied mechanics*, Wiley, New York.

Lin, T. Y., and Burns, N. H. (1981). *Design of prestressed concrete structures*, Wiley, New York.

MacGregor, J. G., and Wight, J. K. (2005). *Reinforced concrete: Mechanics and design*, 4th Ed., Prentice Hall, Upper Saddle River, N.J.

Magnel, G. (1949). "Design of the ends of prestressed concrete beams." *Concrete and Constructional Engineering*, 44(5), 141–148.

Magura, D. P., Sozen, M. A., and Siess, C. P. (1962). "A study of stress relaxation in prestressing reinforcement." *Eleventh Progress Report of the Investigation of Prestressed Reinforced Concrete for Highway Bridges*, University of Illinois, Urbana, Ill.

Marschall, C. W., and Maringer, R. E. (1977). *Dimensional instability: An introduction*, Pergamon Press, New York.

Moser, R. D. (2011). "High-strength stainless steels for corrosion mitigation in prestressed concrete: Development and evaluation." Ph.D. thesis, Sch. of Civil and Environmental Engineering, Georgia Institute of Technology, Atlanta, Ga.

Mott, N. F., and Nabarro, F. R. N. (1948). "Dislocation theory and transient creep." *Physical Society Bristol Conference Report*, 1–19.

Nabarro, F. R. N. (2001). "The time constant of logarithmic creep and relaxation." *Materials Science and Engineering A*, 309/310, 227–228.

Naumenko, K. and Altenbach, H. (2007). *Modeling of creep for structural analysis*, Springer, New York.

Neu, R. W., and Sehitoglu, H. (1992). "Low-temperature creep of a carburized steel." *Metallurgical Transactions A*, 23A, 2619–2624.

Nir, N., Huang, F. H., Hart, E. W., and Li, C.-Y. (1976). "Relationship between anelastic and nonlinear viscoplastic behavior of 316 stainless steel at low homologous temperature." *Metallurgical Transactions A*, 8A, 583–588.

Oding, I. A., Burdukskii, V. V., and Geminov, V. N., translated by Kennedy, A. J. (1965). *Creep and stress relaxation in metals*, Oliver & Boyd, London.

O'Malley, C. J. (2011). "Experimental testing, analysis, and strengthening of reinforced concrete pier caps by exterior post tensioning." Ph.D. thesis, Sch. of Civil and Environmental Engineering, Georgia Institute of Technology, Atlanta, Ga.

Othman, A. M., and Hayhurst, D. R. (1990). "Multi-axial creep rupture of a model structure using a two parameter material model." *International Journal of Mechanical Sciences*, 32(1), 35–48.

Park, R., and Paulay, T. (1975). *Reinforced concrete structures*, Wiley, New York.

Rabotnov, Y. N. (1969). *Creep problems in structural members*, North-Holland Publishing, Amsterdam, The Netherlands.

Ramberg, W., and Osgood, W. R. (1941). "Description of stress–strain curves by three parameters." *Technical Note No. 92*, National Advisory Committee for Aeronautics, Washington, D.C.

Razak, H. A. (1986). "Time dependent effects in reinforced concrete sections subjected to flexure." Ph.D. thesis, Department of Civil Engineering, University of Surrey, Guildford, U.K.

Roscoe, R. (1950). "Mechanical models for the representation of visco-elastic properties." *British Journal of Applied Physics*, 1, 171–173.

Schedin, E., Ivarsson, B., Andersson, M., and Lindström, R. (2012). "Duplex stainless steel in fire." *Acom*, 1-2012, OutoKumpu.

Schlaich, J., Schafer, K., Jennewein, M. (1987). "Toward a consistent design of structural concrete." *PCI Journal*, 3, 74–151.

Schwier, F. (1958). "Wires and bars for prestressed concrete." *RILEM Symposium on Special Reinforcement for Reinforced Concrete and on Prestressing Reinforcement*, Liege, Belgium.

Shams, M. K. (2000). "Time-dependent behavior of high-performance concrete." Ph.D. thesis, Sch. of Civil Engineering, Georgia Institute of Technology, Atlanta, Ga.

Sieurin, H., Sandström, R., and Westin, E. M. (2006). "Fracture toughness of the lean duplex stainless steel LDX 2101." *Metallurgical and Materials Transactions A*, 37A, 2975–2981.

Thornton, P. R., and Hirsch, P. B. (1958). "The effect of stacking fault energy on low temperature creep in pure metals." *Philosophical Magazine*, 3(31), 738–761.

Underwood, E. E. (1970). *Quantitative stereology*, Addison-Wesley, Boston.

Wang, N., O'Malley, C., Ellingwood, B. R., Zureick, A.-H. (2011). "Bridge rating using system reliability assessment. I: Assessment and verification by load testing." *Journal of Bridge Engineering*, 16(6), 854–862.

Weihrauch, P. F., and Hordon, M. J. (1964). "The dimensional stability of selected alloy systems." *Final Report Prepared for the Naval Applied Science Laboratory*, Alloyd General Corporation, Cambridge, Mass.

Wyatt, O. H. (1963). "Transient creep in pure metals." *Proceedings of the Physical Society*, 66, 459–480.

Yamada, H., and Li, C.-Y. (1973). "Mechanical models for the representation of visco-elastic properties." *Metallurgical Transactions*, 4, 2133–2136.

Yang, D. (2011). "Cyclic stress effect on stress corrosion cracking of duplex stainless steel in chloride and caustic solutions." Ph.D. thesis, Sch. of Mechanical Engineering, Georgia Institute of Technology, Atlanta, Ga.

Zureick, A.-H., Bennett, R. M., and Ellingwood, B. R. (2006). "Statistical characterization of fiber-reinforced polymer composite material properties for structural design." *Journal of Structural Engineering*, 132(8), 1320–1327.

Zureick, A.-H., Ellingwood, B. R., Kim, S. H., Bechtel, A., O'Malley, C. J., and Shah, F. (2014). "Bridge repair and strengthening study: Part I." *Final Report Prepared for the Georgia Department of Transportation*, Georgia Institute of Technology, Atlanta, Ga.